MECHANICAL CHARACTERIZATION AND NUMERICAL SIMULATION OF A LIGHT-WEIGHT ALUMINUM A359 METAL-MATRIX COMPOSITE

by

JAMES P. DEMARCO, JR.
B.A., Florida State University, 2002
M.S., Florida State University, 2004

A thesis submitted in partial fulfullment of the requirements
for the degree of Master of Science
in the Department of Mechanical, Materials, and Aerospace Engineering
in the College of Engineering and Computer Science
at the University of Central Florida
Orlando, Florida

Summer Term
2011

ABSTRACT

Aluminum metal-matrix composites (MMCs) are well positioned to replace steel in numerous manufactured structural components, due to their high strength-to-weight and stiffness ratios. For example, research is currently being conducted in the use of such materials in the construction of tank entry doors, which are currently made of steel and are dangerously heavy for military personnel to lift and close. However, the manufacture of aluminum MMCs is inefficient in many cases due to the loss of material through edge cracking during the hot rolling process which is applied to reduce thick billets of as-cast material to usable sheets.

In the current work, mechanical characterization and numerical modeling of as-cast aluminum A359-SiC_p-30% is employed to determine the properties of the composite and identify their dependence on strain rate and temperature conditions. These efforts will allow manufacturers of the material to identify optimum conditions to produce rolled sheets having the desired properties with minimal loss of material through edge cracking. Tensile and torsion tests were performed at a variety of strain rates and temperatures. Data obtained from tensile tests were used to calibrate the parameters of a material model for the composite. The material model was implemented in the ANSYS finite element software suite, and simulations were performed to test the ability of the model to capture the mechanical response of the composite under simulated tension and torsion tests. A temperature- and strain rate-dependent damage model extended the constitutive model to capture the dependence of material failure on testing or service conditions.

Several trends in the mechanical response were identified through analysis of the dependence of experimentally-obtained material properties on temperature and strain rate. The numerical

model was found to adequately capture strain rate and temperature dependence of the stress-strain curves in most cases. Ductility modeling allowed prediction of stress and strain conditions which would lead to rupture, as well as identification of areas of a solid model which are most likely to fail under a given set of environmental and load conditions.

to Aurora, who helped me stand again

ACKNOWLEDGMENTS

TABLE OF CONTENTS

LIST OF FIGURES x

LIST OF TABLES xii

CHAPTER 1: GENERAL INTRODUCTION 1

CHAPTER 2: MECHANICAL CHARACTERIZATION OF A LIGHT-WEIGHT, ALUMINUM A359 METAL-MATRIX COMPOSITE UNDER TENSILE LOADING 4

2.1 Abstract 4

2.2 Introduction 5

2.3 Experimental Approach 7

2.4 Experimental Results 9

2.5 Numerical Approach 14

2.6 Determination of Parameters 17

2.7 Numerical Results 21

2.8 Conclusions 23

2.9 Acknowledgments 24

2.10 References 24

2.11 Tables 29

2.12 Figures 35

CHAPTER 3: CHARACTERIZATION OF THE TORSIONAL RESPONSE OF AS-CAST A359-SiC_p-30% AT ELEVATED TEMPERATURES 52

3.1 Abstract 52

3.2 Introduction 53

3.3 Experimental Procedure 55

3.4 Computational Modeling 58

3.5 Results 62

3.6 Conclusions 67

3.7 References 68

3.8 Tables 74

3.9 Figures 78

CHAPTER 4: AN APPROACH FOR MODELING DUCTILITY OF AS-CAST A359-SiC_p-30% AT ELEVATED TEMPERATURES 94

4.1 Abstract 94

4.2 Introduction 94

4.3 Microscopy and Testing 96

4.4 Numerical Approach 99

4.5 Results 102

4.6 Conclusions 105

4.7 Acknowledgments 106

4.8 References 106

4.9 Tables 110

4.10 Figures 112

CHAPTER 5: GENERAL DISCUSSION 124

LIST OF FIGURES

Figure 2.1: Temperature dependence of various A359-SiC_p-XX%..... 35
Figure 2.2: Backscatter electron micrographs from the as-cast A359-SiC_p-30%..... 36
Figure 2.3: Tensile specimen dimensions..... 37
Figure 2.4: Profile of mechanical test assembly..... 38
Figure 2.5: Temperature dependence of tensile response of A359-SiC_p-30% under moderate strain rates..... 39
Figure 2.6: Strain rate dependence of tensile response of A359-SiC_p-30% at various temperatures..... 40
Figure 2.7: Rate dependence of tensile properties of A359-SiC_p-30%..... 41
Figure 2.8: Temperature dependence of tensile properties of A359-SiCp-30%..... 42
Figure 2.9: Secondary electron micrograph from the fracture surface of composite in the as-cast condition tested at 10^{-3} s^{-1} and 1000°F (538°C)..... 43
Figure 2.10: (a-c) Secondary and (d) backscatter electron micrographs illustrating the various characteristic of fracture in tensile tested A359-SiC_p-30%..... 44
Figure 2.11: Backscatter electron micrographs of evolving Si-eutectic morphology in A359-SiC_p-30%..... 45
Figure 2.12: Linear regression for determination of stress-hardening parameter b..... 46
Figure 2.13: Comparison of simulated and experimental tensile response of A359-SiC_p-30% at various temperatures at a strain rate of 10^{-3} s^{-1}..... 47
Figure 2.14: Comparison of simulated and experimental tensile response of A359-SiC_p-30% at various temperatures at a strain rate of 10^{-2} s^{-1}..... 48
Figure 2.15: Comparison of simulated and experimental tensile response of A359-SiC_p-30% at various strain rates at 1000°F (538°C)..... 49
Figure 2.16: Simulated rate and temperature dependence of the yield strength, σys, of..... 50
Figure 2.17: Simulated temperature and rate dependence of the saturated stress, σs, of..... 51
Figure 3.1: Microstructure of as-cast A359-SiC_p-30%..... 78
Figure 3.2: Torsion specimen dimensions..... 79
Figure 3.3: Profile of mechanical test specimen, heater, and extensometer..... 80
Figure 3.4: Temperature distributions along torsion specimen surface at specified target temperatures..... 81
Figure 3.5: Image of ANSYS model geometry for torsion specimen..... 82
Figure 3.6: Temperature distribution fit. (placeholder)..... 83
Figure 3.7: Torsion behavior of as-cast A359-SiC_p-30% at various temperatures at a strain rate of (a) 10^{-3} s^{-1}, (b) 10^{1} s^{-1}..... 84
Figure 3.8: Torsion behavior of as-cast A359-SiC_p-30% at various strain rates at temperatures of 20°C (68°F) and 538°C (1000°F)..... 85
Figure 3.9: Dependence of equivalent material properties on strain rate for tension and torsion; filled symbols represent tension, empty symbols torsion..... 86

Figure 3.10: Dependence of equivalent material properties on temperature for tension and torsion; filled symbols represent tension, empty symbols torsion 87
Figure 3.11: Comparison of shear stress-strain curves obtained with and without temperature distribution imposed on specimen. 88
Figure 3.12: Comparison of shear stress-strain curves obtained directly from gage surface and by reduction of pilot-node torque-twist data. 89
Figure 3.13: (a) von Mises, and (b) x-y shear stress contours at midplane of specimen, 1000°F, equivalent strain rate 10 s^{-1} 90
Figure 3.14: (a) von Mises, and (b) x-y shear stress contours at midplane of specimen, 1000°F, equivalent strain rate 10 s^{-1} 91
Figure 3.15: Comparison of simulated and experimental tensile response of A359-SiCp-30% at various temperatures at an equivalent strain rate of 10^{-3} s^{-1} 92
Figure 3.16: Comparison of simulated and experimental shear response of A359-SiC_p-30% at various strain rates at 538°C (1000°F) 93
Figure 4.1: Microstructure of A359-SiC_p-30% 112
Figure 4.2: Stress-strain profiles at 538°C (1000°F). Black curves represent tension; gray curves represent torsion. 113
Figure 4.3: Stress-strain profiles at an equivalent strain rate of 10^{-3} s^{-1}. Black curves represent tension; gray curves represent torsion. 114
Figure 4.4: Ultimate strengths and failure strains versus (a) temperature, (b) strain rate. 115
Figure 4.5: Toughness versus (a) strain rate, (b) temperature. 116
Figure 4.6: Polynomial fit to toughness versus temperature and strain rate data. 117
Figure 4.7: Mesh and boundary conditions for torsion simulation ..... **Error! Bookmark not defined.**
Figure 4.8: Damage contours for torsion specimen simulation. (a) Specimen surface. (b) Cross section at midplane. 119
Figure 4.9: Simulated damage histories. (a) Absolute damage. (b) Relative damage. 120
Figure 4.10: Rolling simulation geometry 121
Figure 4.11: Equivalent stress v. strain for torsion test performed at 538°C (1000°F) and equivalent strain rate of 10^{1} s^{-1} and bilinear approximation used for LS-DYNA simulation. 122
Figure 4.12: Rolling damage 123

LIST OF TABLES

Table 2.1: Chemical composition of A359 (vol%) [10] 29
Table 2.2: Tensile experiments on A359-SiC_p-30% 30
Table 2.3: Constitutive modeling constants 31
Table 2.4: Levenberg-Marquardt optimization inputs 32
Table 2.5: Comparison of initial and converged modeling parameters 33
Table 2.6: Optimized hardening constants 34
Table 3.1: Chemical composition of A359 74
Table 3.2: Constitutive modeling constants for Zhou-Clode inelasticity model, as identified via tensile testing 75
Table 3.3: Tensile experiments performed on A359-SiC_p-30% 76
Table 3.4: Equivalent material properties of A359-SiC_p-30% identified through torsion testing 77
Table 4.1: Chemical composition of A359 matrix 110
Table 4.2: Test conditions. A label of "C" indicates torsion, and "TE" indicates tension 111
Table 4.3: Experimental and predicted damage limits 111

CHAPTER 1: GENERAL INTRODUCTION

Aluminum metal-matrix composites (MMCs) are a class of materials in which an aluminum alloy is reinforced by some other material to form a composite material with the desired properties. Aluminum alloys are valued for having low densities and high ductilities, but they lack the strength and stiffness of heavier alloys such as steel. By reinforcing an aluminum alloy with particles of a stronger, stiffer material such as silicon carbide or boron carbide, it is possible to produce a composite that maintains the light weight of the aluminum alloy while obtaining greater strength and stiffness. Thus the resulting composite has a desirable specific stiffness and strength-to-weight ratio. Such a material may be useful when weight becomes a limiting factor in efficiency, as in the case of aerospace components or even ground transport in an age of rising fuel costs. An aluminum MMC may also be useful when the weight of a human-operated component becomes dangerously high, as in the case of hatches on tanks, which must be impact resistant and yet light enough for safe human usage.

While aluminum MMCs are often inexpensive to form through casting, the cost of processing is a limiting factor to wider utilization of these materials. A common method for processing aluminum MMCs is hot rolling, in which cast billets are passed through a roll mill at elevated temperatures to reduce the billets to thin sheets with enhanced material properties. However, it is common for cracks to form along the transverse edges of the rolled sheets. The cracked material must be trimmed from the rolled sheets before further processing, and the trimmed material is lost.

The mechanical response of materials subjected to hot rolling is influenced by such factors as roll temperature, ambient temperature, strain rate, and roll geometry. Manufacturers of aluminum MMCs and other rolled materials seek to establish rolling conditions that will lead to increased ductility with minimal edge cracking. One approach to identifying ideal rolling conditions is to roll a material under a variety of conditions and compare the resulting sheets. However, the drawback of this approach is the cost associated with wasted material and retooling. An alternative approach is to simulate the rolling process through finite element modeling. If an appropriate model can be constructed, a parametric study may be performed to identify ideal rolling conditions.

Simulation of the hot rolling process requires definition of a constitutive model that captures the mechanical response of the material under consideration under arbitrary loading conditions. This thesis concerns the definition, calibration, implementation and utilization of a constitutive model for A359-SiC_p-30%, an aluminum metal-matrix composite. Three articles are included as CHAPTERS TWO, THREE, and FOUR, which describe different aspects of the model and its use. In CHAPTER TWO, the mechanical characterization of A359-SiC_p-30% under tensile loading is described, and a strain rate- and temperature-dependent constitutive model for the material is introduced. The model is implemented as a user-programmable feature in the ANSYS finite element software suite, and the simulated material response under tension is compared with experimental results. In CHAPTER THREE, the mechanical response of A359-SiC_p-30% under torsion is investigated. Experimental data obtained through elevated-temperature torsion testing is analyzed, and results from a scale model simulation of the torsion

specimen are compared with experiments. In CHAPTER FOUR, the constitutive model is extended by the introduction of a strain rate- and temperature-dependent damage model. The model allows comparison of the workability of the material at varying strain rates and temperatures under arbitrary load configurations. The model is applied to simulations of torsion testing and hot rolling. A general discussion follows in CHAPTER FIVE.

CHAPTER 2: MECHANICAL CHARACTERIZATION OF A LIGHT-WEIGHT, ALUMINUM A359 METAL-MATRIX COMPOSITE UNDER TENSILE LOADING

Mechanical Characterization and Numerical Simulation of a Light-Weight, Aluminum A359 Metal-Matrix Composite under Tensile Loading. By James P. DeMarco, Jr., Catalina Uribe-Restrepo, Justin Karl, Yongho Sohn, and Ali P. Gordon

The contents of this chapter were submitted for publication in the ASME Journal of Applied Mechanics

2.1 Abstract

Lightweight, nano-structured aluminum metal-matrix composites (MMCs) have been identified as a next-generation armoring material due to their low density and high strength. While Al-MMCs with 5%, 10% and 20% SiC have been characterized, A359-SiC_p-30% has not received as much attention. In order to reduce material loss through edge cracking during the hot rolling process, it is critical to characterize the deformation and rupture behavior of aluminum metal-matrix composites at high temperatures and moderate strain rates. Multiaxial isotropic constitutive equations designed for modeling the thermomechanical processing response of a lightweight MMC are developed. The model incorporates both strain rate and temperature dependence of the inelastic response, while the elastic behavior is Hookean. To validate the functional forms established in construction of the model and to calibrate its parameters, tensile tests were performed on A359-SiC_p-30% samples at a variety of strain rates and temperatures. Prior to this study, the candidate material has yet to be mechanically characterized. By means of the finite element method, the constitutive model was applied to simulate the tensile response, and a strong correlation with the experimental data was achieved. Metallurgical analyses were

carried out on tensile-tested samples to determine the microstructural mechanisms leading to tensile rupture.

Keywords: metal-matrix composites, mechanical characterization, strain-dependent modeling, temperature-dependent modeling

2.2 Introduction

While aluminum alloys have the advantages of low density and high ductility, they generally lack the strength and elastic modulus of heavier alloys such as steel. Aluminum alloy metal-matrix composites (MMCs) formed through inclusion of hard reinforcement materials have increased strength and elastic modulus compared to the aluminum alloy, but the tradeoff is loss of ductility. Nanoparticle-reinforced composites have begun displacing conventional reinforced materials except in certain extremely high performance applications, due to the disadvantages of the latter which include extremely low ductilities, low transverse properties, high cost, and inability to be processed by standard techniques [1]. Rolled, particle-reinforced composites have transverse property values nearly as high as the longitudinal property values, and much lower processing costs by comparison [1].

Increased processing cost in particle-reinforced composites results from the scrapping of material due to the edge cracking imparted by hot rolling of cast billets of the composite into thin sheets. During the rolling process, cracks form along the edges of the sheet in the long transverse (L-T) direction, where plane stress dominates. This material must be then trimmed from the sheet before further rolling. Through careful control of thermomechanical processing parameters, improved ductility and reduced edge cracking may be achieved.

One approach to optimizing the strength and ductility of this class of materials is to physically hot roll a large collection of cast billets under varied processing conditions (e.g. temperature, roll speed, lubrication), and conduct mechanical experiments on samples incised from the collection of rolled slabs. As a low-cost alternative to even a fractional factorial of this approach, Al-MMC specimens from cast slabs may be subjected to a variety of tensile conditions in the range of the temperature and strain rate conditions associated with rolling. Test conditions which confer high strength and ductility may be identified numerically.

Based on research from literature [2] [3] [4], the particle volume fraction plays a significant role in determining the mechanical properties of the composite. For A359 composites and tensile conditions, the hard particles limit dislocation motion in the matrix material. Tensile strength generally increases with particle volume and decreases with temperature, while ductility generally decreases with particle volume and increases with temperature. These trends are shown in Fig. Figure 2.1. Room temperature (20°C) data is from [5], while A359 and A359-SiC_p-10% data at higher temperatures is from [6], and A359-SiC_p-20% data is from [7]. Strengths and elongations should be not be considered representative of all A359-SiC_p MMCs, since widespread scatter has been identified as a trend for these materials, as noted in [8], e.g.

To support with the thermomechanical process optimization, constitutive equations are developed to capture strain rate and temperature dependence of the stress-strain behavior exhibited by a candidate MMC. The uniaxial plasticity model proposed by Zhou and Clode [9] for torsion is extended to a multiaxial viscoplastic model with temperature-dependent linear

elasticity. The model is then utilized for a parametric study of mechanical response of a cast light-weight composite, A359-SiC_p-30%.

2.3 Experimental Approach

The candidate material for the current investigation is A359-SiC_p-30%. Chemical composition for the matrix alloy, A359, is provided in Table 2.1 [10]. Because of its attractive thermal management properties, the material has been selected for electronic package and brake rotor applications [11]. The composite material, or variations thereof, have been studied under fracture [12], torsion [2], and high strain rate conditions [13].

Four microstructural features are present in A359-SiC_p-30%: Al solid solution (fcc), α-SiC, eutectic regions of Al-solid solution and Si, and precipitates/dispersoids rich in Mg/Fe. Figure 2.2(a) shows the presence of randomly distributed α-SiC particle reinforcement. The average size of these particles, based on image analysis and materials specification, is 17±5 μm, which is in range of the low-cost SiC particle measurements of [11]. In the as-cast microstructure, however, some microstructural inhomogeneity includes clustering of SiC particles and voids due to solidification shrinkage and/or incomplete infiltration. Figure 2.2(b) shows the interdendiritic eutectic morphology of Al solid solution and Si.

Mechanical tests were performed in order to evaluate and characterize the behavior of the cast A359-SiC_p-30%. Monotonic tensile tests were conducted under a variety of temperatures and strain rates. A total of fourteen round, dogbone-type specimens of the as-cast and unrolled material were tested in a static lab air environment using an MTS 100-kN capacity model 810 servohydraulic load frame. Specimens with a 1.0in (25.4mm) gage section were machined from

the unprocessed slabs of material by an ISO-9001 compliant facility into the dimensions shown in Fig. Figure 2.3.

Frame alignment was verified prior to testing as per ASTM standard E1012 [14]. Tests were controlled and recorded by a TestStar IIs control/acquisition system connected to a PC running MTS Multi-Purpose Testware. This series of tensile tests was strain-controlled via a 632-series extensometer with high-temperature capable contact rods.

Tests were defined by applied strain rates of 10^{0}, 10^{-2}, 10^{-3} and 10^{-5} 1/s, as these rates are representative of the processing rates in manufacture. Room temperature (68°F, 20°C) tests followed ASTM E8 [15] guidelines. During elevated temperature testing, target temperature levels were maintained with use of an MTS 653 high temperature furnace utilizing integrated dual-temperature controllers. Furnace sections surround the specimen from the left and right, and extensometer contact rods are inserted from the front of the test station, as pictured in Fig. Figure 2.4. These elevated temperature tests were conducted at 600°F (315.5°C), 750°F (398.9°C) and 1000°F (537.8°C), which were selected as representative of deformation processing temperatures of this material. High temperature test procedures conformed to suggested heat soak times and other guidelines from ASTM standard E21 [16].

The microstructures of ruptured surfaces of the material were examined using a variety of techniques, including X-ray diffraction (XRD), white light optical microscopy (OM) and scanning electron microscopy (SEM). Specimens of interest were sectioned into cubes with approximate dimensions of 1.0cm by 1.0cm by 0.2cm. X-ray diffraction patterns were collected using the Rigaku D-Max B Diffractometer with Cu-Kα radiation, with an accelerating voltage of

40keV, and a scan rate of 0.58 degrees/minute from 2-theta range of 20 to 90. Specimens were mounted in room-temperature curing epoxy resin, ground using SiC grinding papers and polished down to 0.25 micron finish using diamond paste with oil lubricant. For clearer distinction of constituent microstructure, Keller's Reagent was used to etch the metallographically prepared samples. After general observation via OM, Zeiss Ultra-55 field-emission SEM, operating at 25 keV was employed with secondary electrons and backscatter electron contrasts. X-ray energy dispersive spectroscopy (XEDS), equipped on the SEM was also employed to determine compositions of relevant phases semi-quantitatively.

2.4 Experimental Results

Data from experiments were plotted, analyzed, and condensed into a set of material properties. Trends observed in the elastic modulus, flow stress, tensile strength, and ductility are discussed in this section. Some properties showed strong trends with both temperature and strain rate, while others seemed to vary mainly with temperature without a significant dependence on strain rate. Stress-strain curves at various temperatures and at a strain rate of 10^{-3} 1/s are shown in Fig. Figure 2.5. Stress-strain curves at various strain rates and at 600°F (316°C) and 1000°F (538°C) are shown in Figs. Figure 2.6a and Figure 2.6b, respectively. Tensile properties extracted from the stress-strain curves are summarized in Table 2.2 and shown in Figs. Figure 2.7 and Figure 2.8. As the volume fraction of SiC increases from 20% to 30% for A359 MMCs, standard deviation in the modulus, tensile strength, and yield strength increase [8]. Some scatter has been observed in the experimental data reported here, but this is consistent with variable segregation of particles within the microstructure.

Intuitively, the elastic modulus was found to be dependent on temperature (Fig. Figure 2.8). Increases in temperature resulted in a decrease in the Young's modulus over the range of temperatures tested, regardless of strain rate (Fig. Figure 2.5). A slight rise in elastic modulus with exponential increases in rate was noted, with the exception that at 1000°F (538°C), the fastest rate of 10^{-2} 1/s resulted in an elastic modulus much lower than expected (Fig. Figure 2.6). This may be attributed to early yielding as a consequence of the temperature approaching the melting point of the A359 matrix, which is in the range of 1045-1115°F (565-605°C) [17].

Flow stress was determined by a 0.02%-offset method to account for the brittle character of the composite at low temperatures (Table 2.2). As expected, yield strength appeared not to have a rate dependence at 68°F (20°C) or 600°F (316°C), but it was seen to increase monotonically with increasing logarithmic rate at 1000°F (538°C), as shown in Fig. Figure 2.6. More significantly, at all rates tested, yield strength increased between 68°F (20°C) and 600°F (316°C), followed by an equally substantial decline between 600°F (316°C) and 1000°F (538°C). Beyond 600°F (316°C), it appears the mechanism responsible for the onset of yielding changes abruptly, as yield strength falls off rapidly for higher temperatures.

Ultimate tensile strength results show significant scatter when plotted as a function of temperature (Table 2.2). Ultimate strength decreases with increasing temperature, as expected; however, two of the 68°F (20°C) specimens failed even before the slope of the stress-strain curve fell to less than 20% of elastic modulus, resulting in lower ultimate strengths than might be expected under other loadings at low temperatures. As with yield strength, a consistent trend of increasing ultimate strength with strain rate was observed at 1000°F (538°C), with no apparent

trend in the strengths at lower temperatures. Since differences in ultimate strengths at the different rates are very similar to the differences in yield strength for the same rates, it may be surmised that the dependence of ultimate strengths on strain rate at 1000°F (538°C) is due mostly to the dependence of the yield strengths on these rates. Strain rate hardening in the plastic region of the curve is less significant to the ultimate strengths for the rates considered.

As expected, failure strain also increases as a function of temperature, although significant scatter was observed in this data. Failure strains at 68°F (20°C) ranged from 0.24% to 0.75%, while at 1000°F (538°C), failure occurred at strains of 1.30-1.62%. No trend is apparent in the failure strain data with respect to strain rate.

Stress levels and curve profile in the plastic zone are strongly influenced by temperature, and strain-rate dependence is apparent at high temperatures. As it may be noted in Figs. Figure 2.5 and Figure 2.6, at high temperatures and low rates, there are significant fluctuations in stress level about a mean over narrow increments in strain. This is due to a phenomenon known as *serrated yielding*, equivalently known as dynamic recrystallization, that is known to occur at low strain rates and high temperatures [18] [19].

In order to characterize the mechanisms leading to tensile rupture, two regions of fractured specimens were examined: fracture surface and cross-section of the gage section near fracture surface. Scanning electron microscopy (SEM), using the Zeiss Ultra-55 field-emission SEM, was carried out to examine the deformed and fractured specimens and to characterize the failure mechanisms under tension at each strain rate and testing temperature.

In order to study the effect of the temperature on the spatial distribution of damage and failure mechanisms, a fix strain rate of 10^{-2} mm/mm-s was selected, and the specimens TE10 (72°F, 20°C), TE05 (600°F, 316°C), and TE06 (1000°F, 538°C) were sectioned in the longitudinal direction (loading direction) using a low speed diamond saw. Each sectioned sample was polished up to 1 μm and finished with colloidal silica. For clearer distinction of constituent microstructure, Keller's Reagent was used to etch the metallographically prepared samples. Microstructural evolution with temperature at this fixed rate was examined by SEM.

At the macroscopic level, all of the composite specimens failed in characteristic brittle matter. As observed in Fig. Figure 2.9, there is no evidence of necking, and the fracture surface is generally flat. A combination of different failure mechanisms was observed to be common for all of the specimens: (i) a crack propagating through the eutectic region and also through the silicon network, (ii) the growth and coalescence of voids in the matrix, (iii) partial debonding at the particle-matrix interface, and (iv) a less-frequent fracture of reinforcing particles close to the fracture surface.

SEM was used to determine the predominant failure mechanisms characteristic of the composite under the different tested conditions. Figure 2.10(a) shows that a microcrack in the composite follows the silicon-rich interdendritic eutectic. Failure of all of the specimens appeared to be controlled by failure of the silicon-rich interdendritic eutectic and not the silicon carbide particles. The Si network fails first as the load increases, through fracture of the Si particles. These fractured Si particles are linked together ensuing the final failure of the specimen. It is observed in Fig. Figure 2.10(b) that a bimodal distribution of dimples which correspond to voids

nucleated around the reinforcement particles and voids originated during the fracture process in the ductile matrix. Because the failure strain of silicon is much smaller than that of the aluminum matrix, the silicon phase fractured first as the deformation increases followed by the nucleation and growth of voids at the silicon–aluminum interfaces. Figure 2.10(c) shows a SiC particle-matrix debonding during fracture which was caused by a particle poorly bonded to the matrix. Although this mechanism was observed in few locations for all of the specimens under study, it was not the predominant mechanism. The micrograph seen in Fig. Figure 2.10(d) shows a region close to the fracture surface (loading direction) which appears to involve some particle fracture along crack propagation. From the four mechanisms discussed above, the last two described were the most rarely observed in all of the tested specimens. From the observations mentioned above, it is conclude that fracture of the composite appears to be controlled by failure of the matrix which is dominated by the fracture of the silicon particle network. This failure mode is consistent with tensile results of Li and co-authors [20].

Tensile failure mechanisms in the A359-SiC_p-30% composite are not significantly affected by the rate of deformation over the range of strain rates considered. In order to study the effect of the temperature on the spatial distribution of damage and failure mechanisms, a fixed strain rate of 10^{-2} 1/s was selected, and the specimens tested at 68°F (20°C) , 600°F (316°C) , and 1000°F (538°C) were sectioned in the longitudinal direction (loading direction). Figure 2.11 shows the evolution of the morphology of brittle silicon in the eutectic region as a function of testing temperature. In Figs. Figure 2.11(a,b) a silicon with a sharp-edged and fibrous rod-like morphology (e.g., eutectic) is observed. Figure 2.11(c) shows a silicon with a more cylindrical

and less sharp-edged morphology. For the last case, the amount of eutectic silicon is smaller than in the other two cases.

As discussed by Ogris and colleagues [21], the strength and ductility of the A359 matrix is predominantly influenced by the brittle eutectic silicon and its morphology. It was observed that an increase in strength and decrease of ductility occurs in sharp-edged and fibrous rod-like eutectic silicon, which is consistent with results presented here. It is also known that a decrease in the amount of eutectic silicone leads to an increase in total ductility.

2.5 Numerical Approach

The numerical approach applied in the current study is that of classic associative viscoplasticity, as described in Simo and Hughes [22]. The material is assumed to be elastically isotropic with isotropic hardening. A von Mises yield criterion is applied for determination of the stresses capable of inducing plastic deformation. The elastic behavior is governed by the tensorial version of Hooke's law, i.e.,

$$\sigma_{ij} = C_{ijkl} : \epsilon_{kl}^{el} \tag{1}$$

where ϵ_{kl}^{el}, the elastic strain tensor, satisfies

$$\epsilon_{kl}^{el} = \epsilon_{kl} - \epsilon_{kl}^{vp} \tag{2}$$

and ϵ_{kl}, ϵ_{kl}^{vp} are the total and viscoplastic strain tensors, respectively. The elastic response is assumed to be linear, so that

$$C_{ijkl} = \lambda\delta_{ij}\delta_{kl} + 2\mu\left[\frac{1}{2}\left(\delta_{ik}\delta_{jl} + \delta_{il}\delta_{jk}\right)\right] \tag{3}$$

where

$$\lambda = \frac{E\nu}{(1+\nu)(1-2\nu)} \tag{4}$$

$$\mu = \frac{E}{2(1+\nu)} \tag{5}$$

are the Lamé constants, and E and ν are the elastic modulus and Poisson's ratio, respectively. The yield function is given by

$$f = \|\eta_{ij}\| - \sqrt{\frac{2}{3}}K(\alpha; \dot{\alpha}_{avg}, T) \tag{6}$$

where

$$\eta_{ij} = d\text{ev}[\sigma_{ij}] \tag{7}$$

is the stress deviator. The term $K(\alpha)$ is the isotropic hardening function, α is the von Mises equivalent strain, $\dot{\alpha}_{avg}$ is the average plastic strain rate, and T is the temperature in Kelvin. The von Mises equivalent strain, follows

$$\dot{\alpha} = \gamma\sqrt{\frac{2}{3}} \tag{8}$$

where

$$\gamma = \frac{\langle f \rangle}{\eta} \tag{9}$$

The symbols ⟨ ⟩ are the Macaulay brackets and η is a parameter controlling the hardening response; as $\eta \to 0$, rate-independent classical plasticity is recovered. Flow is defined as follows:

$$\dot{\epsilon}_{ij}^{vp} = \gamma \frac{\partial f}{\partial \sigma_{ij}} \tag{10}$$

The isotropic hardening is defined as

$$K(\alpha; \dot{\alpha}_{avg}, T) = \sigma_{ys}(\dot{\alpha}_{avg}, T) + \sigma_{ZC}(\alpha; \dot{\alpha}_{avg}, T) \tag{11}$$

where σ_{ys} is the 0.02% yield stress and σ_{ZC} is the von Mises stress calculated in the Zhou-Clode torsion model:

$$\sigma_{ZC} = C[1 - \exp(-b\alpha^n)] \sinh^{-1}\left[B\dot{\alpha}^m \exp\left(\frac{Qm}{kT}\right)\right] \tag{12}$$

where k is the ideal gas constant and Q is the energy in joules. In order to ensure stability of the numerical integration of the governing equations, the equivalent viscoplastic strain rate $\dot{\alpha}_{avg}$ is taken to be an averaged value which is specified as a parameter to the model. The terms b and n in the expression for the von Mises stress control the shape of the hardening portion of the stress-strain curve. The hardening is expected to be rate and temperature dependent, so b and n are defined in terms of the temperature-compensated strain rate [9]:

$$b = \alpha_b Z_\epsilon^{\beta_b} \tag{13}$$

$$n = \alpha_n Z_\epsilon^{\beta_n} \tag{14}$$

Where

$$Z_\epsilon = \dot{\epsilon} \exp\left(\frac{Q}{kT}\right) \tag{15}$$

Similarly, the elastic modulus is expected to be temperature dependent, and the yield strength is taken to depend on both temperature and strain rate. The elastic modulus is assumed to be thermally activated of the form

$$E = \alpha_E \exp\left[\frac{\beta_{E,1}}{T}\left(\frac{\beta_{E,2}}{T} - 1\right)\right] \tag{16}$$

The dependence of the yield strength on temperature is discussed in Section 5. In order to apply the model, several parameters must be determined. These parameters are listed in Table 2.3.

The model is implemented as a user-programmable feature (UPF) in the ANSYS general-purpose finite element software suite. The algorithm is based on the algorithms for nonlinear isotropic/kinematic J_2 plasticity and linear isotropic/kinematic J_2 viscoplasticity given in Simo and Hughes [22].

2.6 Determination of Parameters

Parameters of the constitutive model were calibrated to match data obtained by uniaxial tensile tests of the material (Figs. Figure 2.5 and Figure 2.6). In the Zhou-Clode formulation, parameters controlling saturated stress were obtained via quasi-linear regression. For the current investigation, a variant of the Levenberg-Marquardt (L-M) algorithm [23] was used to provide an optimal least squares fit of the stress-strain curves obtained in tensile testing. The L-M algorithm was obtained as part of the MINPACK optimization suite [24]. Since the current framework includes an elastic portion of the stress-strain curve, plasticity occurs only after the yield strength is reached. Hence the saturated stress is replaced by the difference between the saturated stress

and the yield stress. The data used for the L-M optimization routine for parameters C, B, m, and Q are given in Table 2.4.

Saturated stress is defined here to be the stress level at which further strain does not result in increased stress. When, in the case of the uniaxial tensile tests that were performed, engineering stresses are recorded, the saturated stress is considered to be the highest engineering stress reached before necking leads to diminished engineering stress. If the specimen fails while the slope of the stress-strain curve is still appreciably positive, the curve is fitted to a negative exponential and the ultimate tensile strength of the fitted curve is taken to be the saturated stress.

For the multiaxial version of the Zhou-Clode model, termed as modified Zhou-Clode, saturated stress is obtained as the limit of the stress as the plastic strain tends to infinity. The constitutive equation can be simplified in the uniaxial case to

$$\sigma = \sigma_{ys} + \sigma^*\left(1 - e^{-b\epsilon}\right). \tag{17}$$

where

$$\sigma^* = C\sinh\left[B\dot{\epsilon}^m \exp\left(\frac{Qm}{kT}\right)\right]. \tag{18}$$

Thus σ_s is the sum of σ_{ys} and σ^*. The L-M algorithm allows the determination of optimal *C*, *B*, *m*, and *Q* so that the difference $\left(\sigma_s - \sigma_{ys}\right) - \sigma^*$ is minimized for each data triple $\left(T, \dot{\epsilon}, \sigma_s - \sigma_{ys}\right)$. It is necessary to provide the algorithm with a set of objective functions to be minimized along with the gradient of each function. The set of objective functions is

$$\{g_i(C, B, m, Q)\}_{i=1}^{N} \tag{19}$$

where N is the number of data triples, i.e., the number of tests performed under various conditions,

$$g_i = \left(\sigma_s - \sigma_{ys}\right)_i - \sigma_i^* \tag{20}$$

and

$$\sigma_i^* = C\sinh^{-1}\left(B\dot{\epsilon}_i^m \exp\left(\frac{Qm}{kT_i}\right)\right) \tag{21}$$

An initial guess for the set of parameters was selected based on the parameters used to model AA5252 in [9]. A convergence criterion of 10^{-8} was set to ensure an optimal fit was obtained. The result was a factor of six reduction in the root mean square of residuals due to each test, from 32.1MPa to 5.1MPa. Initial and final values of the parameters are shown in Table 2.5.

The parameters α_b, β_b defining the stress hardening portion of the stress-strain curve may be found through a two step process. In the first step, the optimal value of the strain coefficient b is determined. This is achieved by linear regression of the points (ϵ, σ_{ref}), where

$$\sigma_{ref} = \ln\left(1 - \frac{\sigma - \sigma_{ys}}{\sigma^*}\right) \tag{22}$$

for each experiment. The slope of the resulting line (with intercept set to zero) is b. A sample regression analysis is shown in Fig. Figure 2.12, and the results are summarized in Table 2.6. In the second step, the temperature-adjusted strain rate $Z_\epsilon = \dot{\epsilon}\exp\left(\frac{Q}{kT}\right)$ is computed for each test. The coefficient b is a function of Z_ϵ with parameters α_b and β_b:

$$b = \alpha_b Z_\epsilon^{\beta_b}. \tag{23}$$

On application of the natural logarithm, the expression becomes

$$\ln b = \ln \alpha_b + \beta_b \ln Z_\epsilon \tag{24}$$

to which a line with slope β_b and intercept $\ln(\alpha_b)$ may be fitted.

The yield strength was modeled as a function of temperature for low temperatures at which strain rate dependence was slight and as a function of both temperature and rate at higher temperatures. Following standard temperature-activation models for mechanical properties, to identify yield strength trends, the natural logarithms of the yield strengths were compared to the inverse of the temperatures in Kelvin. Since the yield strength appeared to peak around 600°F (316°C), the yield strengths were assumed to be piecewise linear on the temperature-activation plot between 68°F (20°C) and 600°F (316°C). Between 600°F (316°C) and 1000°F (538°C), the natural logarithm of the yield stress is defined to be a bilinear function of the inverse temperatures and the logarithm of the rate. Contours of the resulting yield strengths plotted against temperature and logarithmic strain rate are shown in Fig. Figure 2.13.

Elastic modulus was assumed to be dependent on temperature only, with variations in modulus at different rates attributed to scatter in the data. On a temperature activation plot, a linear regression of the elastic modulus data gives a d.o.f.-adjusted R^2 value of 0.496, whereas a quadratic regression gives a degree-of-freedom-adjusted R^2 value of 0.798. Since the quadratic regression gives a better adjusted R^2, the quadratic model was selected for the temperature dependence of the elastic modulus. The resulting formula is

$$E = 2.974 \exp\left[-\frac{189.66}{T}\left(\frac{3020}{T} - 1\right)\right] \tag{25}$$

which may be considered to represent the action of two different mechanisms.

2.7 Numerical Results

In order to test the efficacy of the constitutive model described in the previous two sections, the model was implemented as a user-programmable feature (UPF) in the ANSYS finite-element analysis software suite. Simulated strain-controlled tensile tests were performed on a single SOLID185 element at various rates and temperatures. The stress-strain curves for these tests were obtained, and contours for yield strength and ultimate tensile strength were plotted against temperature and the logarithmic strain rate. Yield strengths imposed in stress-strain curve comparisons are exact due to the wide variability in these values and their strong influence on the resulting ultimate tensile strength, as noted in the experimental results section. Elastic moduli are as given in the previous section, and plasticity is modeled using the constants indicated in Table 2.5.

At a strain rate of 10^{-3} 1/s, good agreement is observed between the simulated and experimental stress-strain curves, as shown in Fig. Figure 2.14. In the linearly elastic region, simulated and experimental curves are almost indistinguishable at 68°F (20°C) and 1000°F (538°C). Near the yield point, the 68°F (20°C) simulation overestimates the stress. At 68°F (20°C) and 600°F (316°C), the stresses in the plastic region are underestimated by the simulation by between 5 and 15 MPa, but slopes match well. At 1000°F (538°C), serrated yielding makes it more difficult to determine the quality of the fit, but since high-temperature low-rate testing suggests a Portevin-

LeChatelier effect [18] with stress drops during locking-unlocking events, it appears that stress levels are again slightly underestimated by the simulation.

Similar trends may be observed by comparing the stress-strain curves at the higher strain rate of 10^{-2} 1/s, as shown in Fig. Figure 2.15. The elastic regions of the curves match well, except at 1000°F (538°C), where it appears that some partial yielding occurred at low stress in the experimental curve. Again, simulated stresses tend to underestimate experimental stresses, although to a lesser extent at 1000°F (538°C). The room temperature (68°F, 20°C) experiment resulted in an early failure, so the saturated stress level was not reached in this case.

Strain-rate hardening becomes pronounced at high temperatures. In Fig. Figure 2.16, simulated and experimental stress-strain curves at 1000°F and at various strain rates are displayed. Since elastic modulus was assumed to be a function of temperature only, there is some discrepancy in the linearly elastic portion of the curves for the higher strain rates. In regions of plasticity, slopes of simulated and experimental curves are similar, although stress levels are underestimated in two of the three cases. Saturated stress was reached in all three cases. Simulations were stopped at the strains corresponding to ultimate tensile strength.

Ultimate strengths for all temperatures between 68°F (20°C) and 1000°F (538°C) and all rates between 10^{-5} 1/s and 10^{-2} 1/s were predicted on the basis of the model for yield strength and the calibrated model for saturated plastic stresses. The results are shown in Fig. Figure 2.17. A comparison of the contours for yield strength and ultimate strength show the strong influence of yield strength on the shape of the contours at high temperatures, but it is important to note that the form of the yield function is such that temperature dependence of plastic stresses becomes

stronger for higher temperatures as well. The error in the modeled ultimate strength is between 5 and 10% for all elevated-temperature tests and for the 68°F (20°C) test at 10^{-3} 1/s; however, early failure in the remaining 68°F (20°C) tests resulted in large errors for these. Further study regarding modeling of ductility in the composite will address this issue.

2.8 Conclusions

As-cast A359-SiC_p-30% was characterized mechanically and metallographically under tensile conditions and temperatures ranging from room temperature to 1000°F and at a variety of strain rates between 10^{-5} and 10^{-2}. Stress-strain curves were obtained for all tests, and material properties were extracted. The material properties were used to calibrate a linearly-elastic, multiaxial extension to the Zhou-Clode plasticity model. Microstructural analysis with optical and scanning electron microscopy was performed to identify possible mechanisms responsible for the trends observed in material properties. The material properties of A359-SiC_p-30% exhibit strong rate dependence at high temperatures and temperature dependence at all rates. The 0.02%-offset yield strength reaches a maximum between 600°F and 1000°F and decreases for temperatures above that at which the maximum occurs. Further study will seek to identify the temperature corresponding to the yield strength maximum. Elastic modulus, yield strength, and the shape of the plasticity curve may be modeled accurately over a range of temperatures and strain rates using the models formulated in the foregoing sections. Ultimate strength can be modeled accurately at elevated temperatures, and can be modeled accurately at room temperature when the specimen reaches saturated stress before failure. Ductility modeling will be necessary to improve ultimate strength estimates at room temperature. Simulated tensile tests indicated the highest ultimate strength occurred at a strain rate of 10^{-2} 1/s and at a temperature of 68°F (20°C).

2.9 Acknowledgments

The authors would like to recognize the U.S. Army Research Laboratory (Kyo Cho and Brandon McWilliams) and MC-21 (David Schuster, Mike Skibo and Allen Drake) for their valuable support in this research.

2.10 References

[1] K. Park, J. E. Lavernia, and F. A. Mohamed, "High temperature creep of silicon carbide particulate reinforced aluminum," *Acta metallurgica et materialia*, vol. 38, no. 11, pp. 2149-2159, 1990.

[2] Y. Li, K. T. Ramesh, and E. S. C. Chin, "The mechanical response of an A359/SiCp MMC and the A359 aluminum matrix to dynamic shearing deformations," *Materials Science and Engineering A*, vol. 382, pp. 162-170, 2004.

[3] R. Rodríguez-Castro, R. C. Wetherhold, and M. H. Kelestemur, "Microstructure and mechanical behavior of functionally graded Al A359/SiCp composite," *Materials Science and Engineering A*, vol. 323, pp. 445-456, 2002.

[4] M. Song, "Effects of volume fraction of SiC particles on mechanical properties of SiC/Al composites," *Transactions of Nonferrous Metals Society of China*, vol. 19, pp. 1400-1404, 2009.

[5] M. Song, "Effects of volume fraction of SiC particles on mechanical properties of SiC/Al composites," *Transactions of Nonferrous Metals Society of China*, vol. 19, pp. 1400-1404, 2009.

[6] O. A. Hamed, M. A. Shady, and A. R. El-Desouky, "Creep behavior of a cast 359/SiC/10p

aluminum composite," *Materials and Design*, vol. 22, pp. 473-479, 2001.

[7] N. P. Hung, C. S. Lim, Y. K. Ho, Y. C. Tan, and W. G. Tan, "Cumulative creep and hot isostatic pressing of particle-reinforced metal matrix composites," *Journal of Materials Processing Technology*, vol. 101, pp. 104-109, 2000.

[8] P. K. Rohatgi, R. B. Thakkar, J. K. Kim, and A. Daoud, "Scatter and statistical analysis of tensile properties of cast SiC reinforced A359 alloys," *Materials Science and Engineering A*, vol. 398, pp. 1-14, 2005.

[9] M. Zhou and M. P. Clode, "Hot torsion tests to model the deformation behavior of aluminum alloys at hot working temperatures," *Journal of Materials Processing Technology*, vol. 72, pp. 78-85, 1997.

[10] C. Triveño Rios, C. Bolfarini, W. J. Botta F., and C. S. Kiminami, "Rapidly Solidified Al-Si-Mg Alloy," *Journal of Metastable and Nanocrystalline Materials*, pp. 594-598, 2004.

[11] W. H. Hunt, D. M. Schuster, M. D. Skibo, M. T. Smith, and D. R. Herling, "Lower Cost Cast Aluminum MMC Process and Products," in *State of the art in cast metal matrix composites in the next millenium; proceedings of a symposium*, 2000, pp. 265-272.

[12] D. P. Myriounis, S. T. Hasan, N. M. Barkoula, A. Paipetis, and T. E. Matikas, "Effects of Heat Treatment on Microstructure and the Fracture Toughness of SiCp/Al Alloy Metal Matrix Composites," *Journal of advanced materials*, vol. 41, no. 3, pp. 18-27, 2009.

[13] Y. Li, K. T. Ramesh, and E. S. C. Chin, "Viscoplastic Deformations and Compressive Damage in an A359/SiCp Metal-Matrix Composite," *Acta mater.*, vol. 48, pp. 1563-1573,

2000.

[14] ASTM, *ASTM E-1012-05. "Standard Practice for Verification of Test Frame and Specimen Alignment Under Tensile and Compressive Axial Force Application"*. West Conshohocken, PA, vol. 03.01.

[15] ASTM, *ASTM E8/E8M-08. "Standard Test Methods for Tension Testing of Metallic Materials"*. West Conshohocken, PA, vol. 03.01.

[16] ASTM, *ASTM E21-09. "Standard Test Methods for Elevated Temperature Tension Tests of Metallic Materials"*. West Conshohocken, PA, vol. 03.01.

[17] J. G. Kaufman and E. L. Rooy, *Aluminum Alloy Castings: Properties, Processes, and Applications*. Materials Park, OH: ASM International, 2004.

[18] P. Rodriguez, "Serrated plastic flow," *Bulletin of Material Science*, vol. 6, no. 4, pp. 653-663, September 1984.

[19] J. Sarkar and M. K. Surappa, "Serrated yielding in thermomechanically processed 6061 Al-SiCp composite," *Journal of Materials Science Letters*, pp. 835-837, 1994.

[20] Y. Li, K. T. Ramesh, and E. S. C. Chin, "Plastic Deformation and Failure in A359 Aluminum and an A359-SiCp MMC under Quasistatic and High-strain-rate Tension," *Journal of Composite Material*, vol. 41, pp. 27-40, 2007.

[21] E. Ogris, A. Wahlen, H. Luchinger, and P. J. Uggowitzer, "On the silicon spheroidization in Ai-Si alloys," *Journal of Light Metals*, vol. 2, pp. 263-269, 2002.

[22] J.C. Simo and T.J.R. Hughes, *Computational Inelasticity*, 1st ed., J.E. Marsden, L. Sirovich,

and S. Wiggins, Eds. New York, U.S.A.: Springer-Verlag, 1998.

[23] C. T. Kelley, *Iterative Methods for Optimization*. Philadelphia: Society for Industrial and Applied Mathematics, 1999, Also available at http://www.siam.org/books/textbooks/fr18_book.pdf.

[24] J. J. Moré, B. S. Garbow, and K. E. Hillstrom, "User Guide for MINPACK-1," Argonne National Laboratory, Argonne, ANL-80-74, 1980.

[25] G. E. Dieter, H. A. Kuhn, and S. L. Semiatin, Eds., *Handbook of Workability and Process Design*. Materials Park, OH: ASM International, 2003.

[26] D. P. Myriounis, S. T. Hasan, and T. E. Matikas, "Microdeformation behaviour of Al-SiC metal matrix composites," *Composite Interfaces*, vol. 15, no. 5, pp. 495-514, 2008.

[27] Y. Li, K. T. Ramesh, and E. S. C. Chin, "The compressive viscoplastic response of an A359/SiCp metal-matrix composite and of the A359 aluminum alloy matrix," *International Journal of Solids and Structures*, vol. 37, pp. 7547-7562, 2000.

[28] A. Madgwick, C. Ungpinitpong, T. Mori, and P. J. Withers, "Observation and quantitative analysis of damage caused by creep in an Al A359/SiCp composite," *Materials Science and Engineering A*, vol. 342, pp. 201-206, 2003.

[29] ASTM, *ASTM E143-02: Standard Test Method for Shear Modulus at Room Temperature*. West Conshohocken, PA.

[30] ASTM, *ASTM A938-07: Standard Test Method for Torsion Testing of Wire*. West Conshohocken, PA.

[31] D. R. Barraclough, H. J. Whittaker, K. D. Nair, and C. M. Sellars, "Effect of Specimen Geometry on Hot Torsion Test Results for Solid and Tubular Specimens," *Journal of Testing and Evaluation*, vol. 1, no. 3, pp. 220-226, May 1973.

[32] ASTM, *ASTM B598-09: Standard Practice for Determining Offset Yield Strength in Tension for Copper Alloys*. West Conshohocken, PA.

2.11 Tables

Table 2.1: Chemical composition of A359 (vol%) [10]

Si	Fe	Cu	Mn	Mg	Zn	Sn	(Trace)	Al
9.45	0.11	<0.006	<0.05	0.67	<0.05	0.02	0.2	Bal.

Table 2.2: Tensile experiments on A359-SiC_p-30%

Spec. ID	Temp., T (°F (°C))	Strain Rate, $d\varepsilon/dt$ (1/s)	Young's Modulus, E (GPa)	0.02% Yield Strength, σ_{ys} (MPa)	Ultimate Strength, σ_{UTS} (MPa)	Fracture Strain, ε_f
TE10	68 (20)	10^{-2}	124	77	171	0.0037
TE02	68 (20)	10^{-3}	115	95	213	0.0075
TE11	68 (20)	10^{-5}	108	84	142	0.0024
TE05	600 (316)	10^{-2}	132	115	192	0.0100
TE03	600 (316)	10^{-3}	104	118	172	0.0045
TE04	600 (316)	10^{-5}	107	120	185	0.0113
TE06	1000 (538)	10^{-2}	50	82	132	0.0162
TE07	1000 (538)	10^{-3}	88	73	116	0.0128
TE08	1000 (538)	10^{-4}	78	48	83	0.0130

Table 2.3: Constitutive modeling constants

Parameter	Units	Significance
α	mm/mm/s	Average viscoplastic strain
α_b	(unitless)	Scaling factor for temperature-compensated strain rate (TCSR) in strain hardening coefficient
α_n	(unitless)	Scaling factor for TCSR in strain hardening exponent
B	s	Scaling factor for combined effect of rate and temperature
β_b	(unitless)	Exponent for TCSR in strain hardening coefficient
β_n	(unitless)	Exponent for TCSR in strain hardening exponent
c	MPa	Scaling factor for stress; does not affect rate or temperature dependence
m	(unitless)	Exponent for combined effect of rate and temperature
Q	J/mol	Exponent that differentiates effect of temperature from rate

Table 2.4: Levenberg-Marquardt optimization inputs

Temp., T (°F (°C))	Strain Rate, dε/dt (1/s)	Saturated Stress, σ_S (MPa)	0.02% Yield Strength, σ_{ys} (MPa)
68 (20)	10^{-2}	206	77
68 (20)	10^{-3}	215	95
68 (20)	10^{-5}	203	84
600 (316)	10^{-2}	192	115
600 (316)	10^{-3}	188	118
600 (316)	10^{-5}	178	120
1000 (538)	10^{-2}	132	82
1000 (538)	10^{-3}	116	73
1000 (538)	10^{-4}	83	48

Table 2.5: Comparison of initial and converged modeling parameters

Parameter (Units)	Initial Value	Final Value
C'	10.0000	15.0600
B' (s)	0.05000	1.20200
m	0.20000	0.11550
Q (J/mol)	165750	175752

Table 2.6: Optimized hardening constants

Spec. ID	Temp., T (°F (°C))	Strain Rate, $d\varepsilon/dt$ (1/s)	Hardening Constant, b
TE10	68 (20)	10^{-2}	767.2
TE02	68 (20)	10^{-3}	527.3
TE11	68 (20)	10^{-5}	1220.9
TE05	600 (316)	10^{-2}	561.8
TE03	600 (316)	10^{-3}	1139.4
TE04	600 (316)	10^{-5}	399.8
TE06	1000 (538)	10^{-2}	627.0
TE07	1000 (538)	10^{-2}	559.3
TE08	1000 (538)	10^{-4}	592.7

2.12 Figures

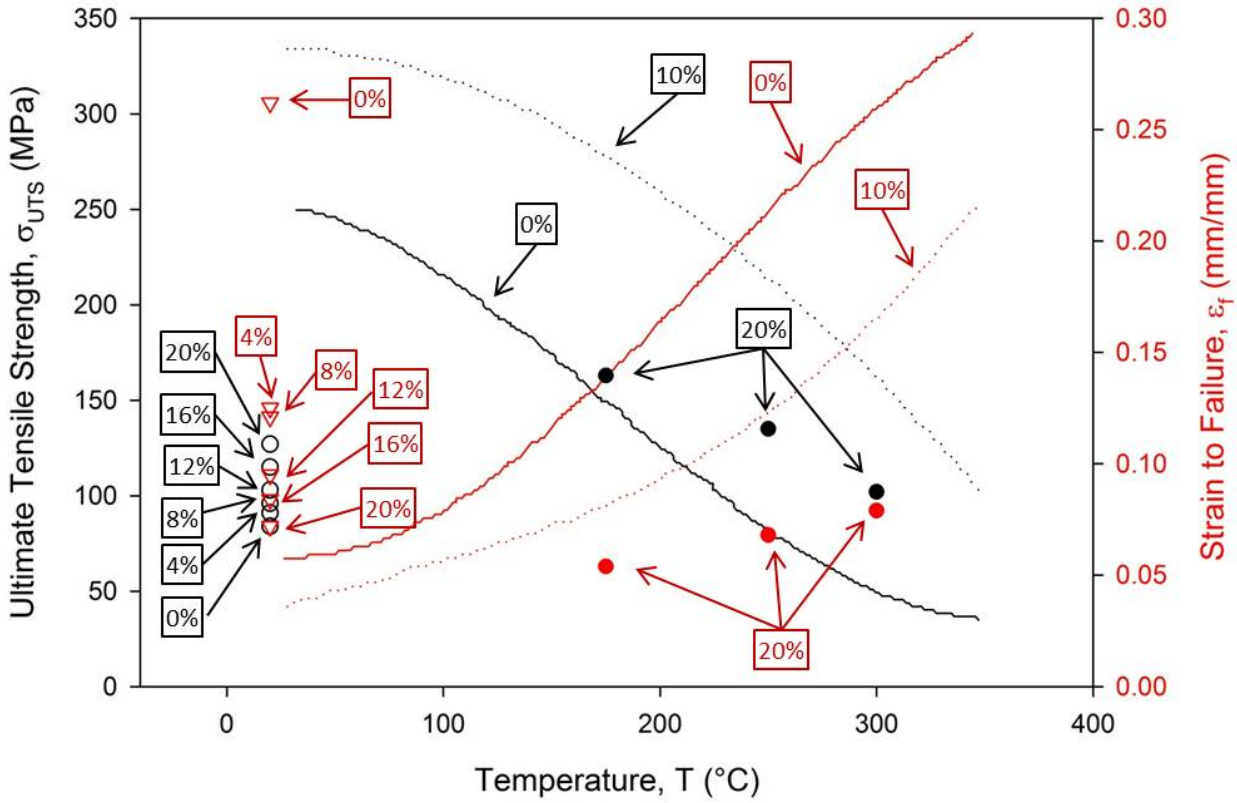

Figure 2.1: Temperature dependence of various A359-SiC_p-XX%

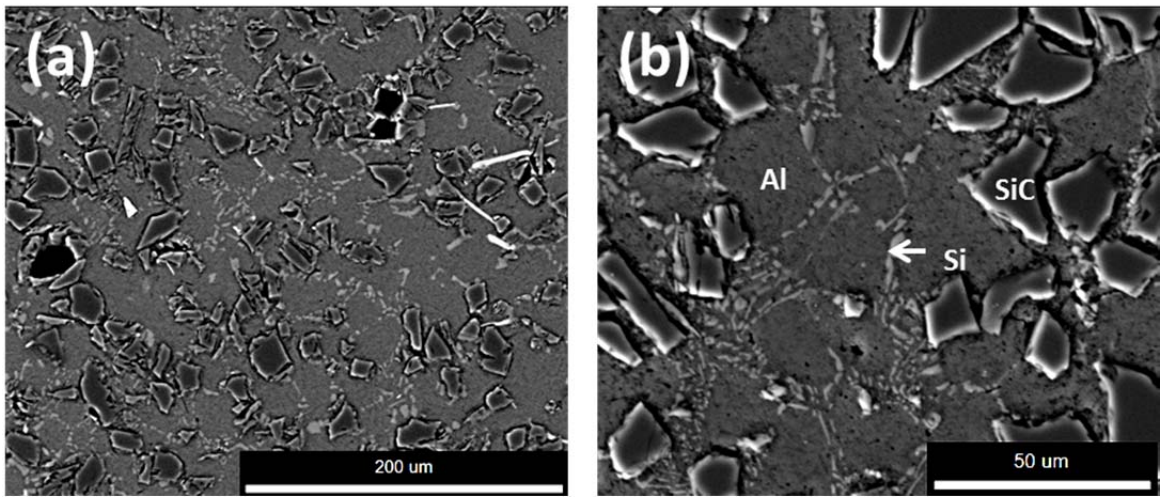

Figure 2.2: Backscatter electron micrographs from the as-cast A359-SiC_p-30%.

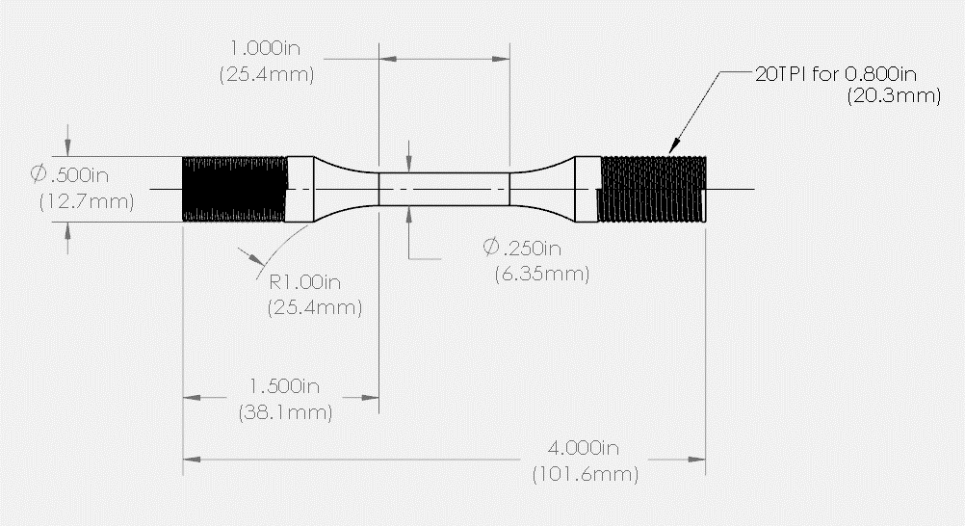

Figure 2.3: Tensile specimen dimensions.

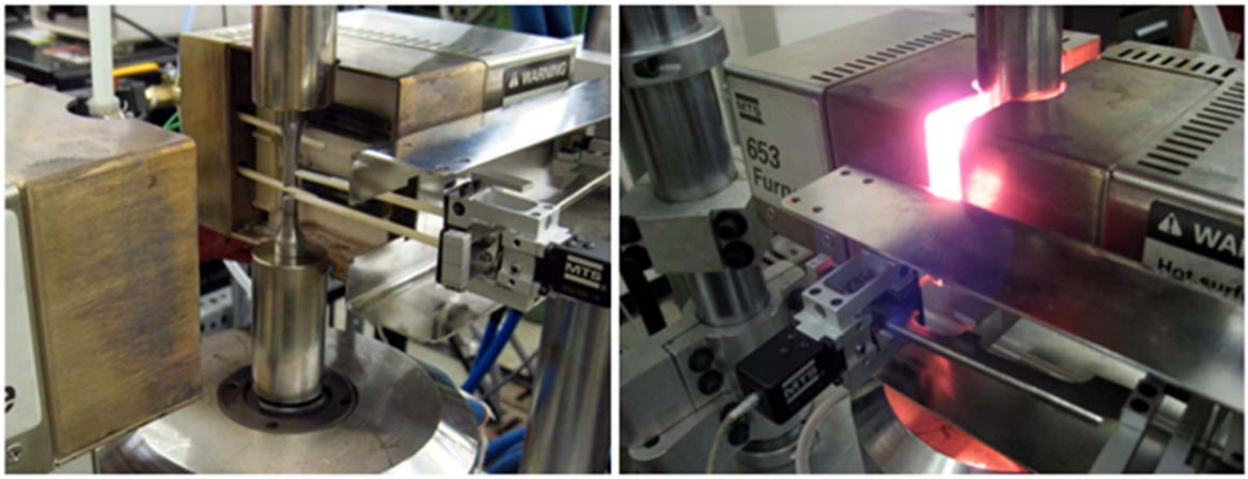

Figure 2.4: Profile of mechanical test assembly.

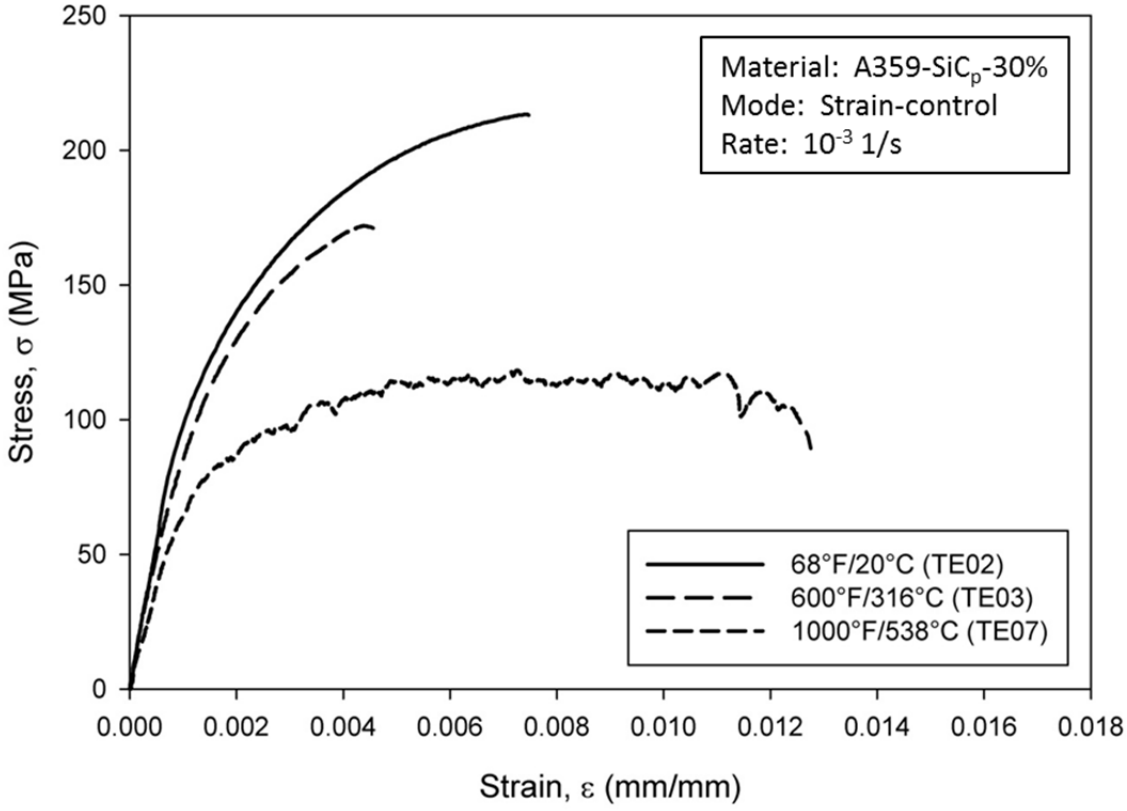

Figure 2.5: Temperature dependence of tensile response of A359-SiC_p-30% under moderate strain rates.

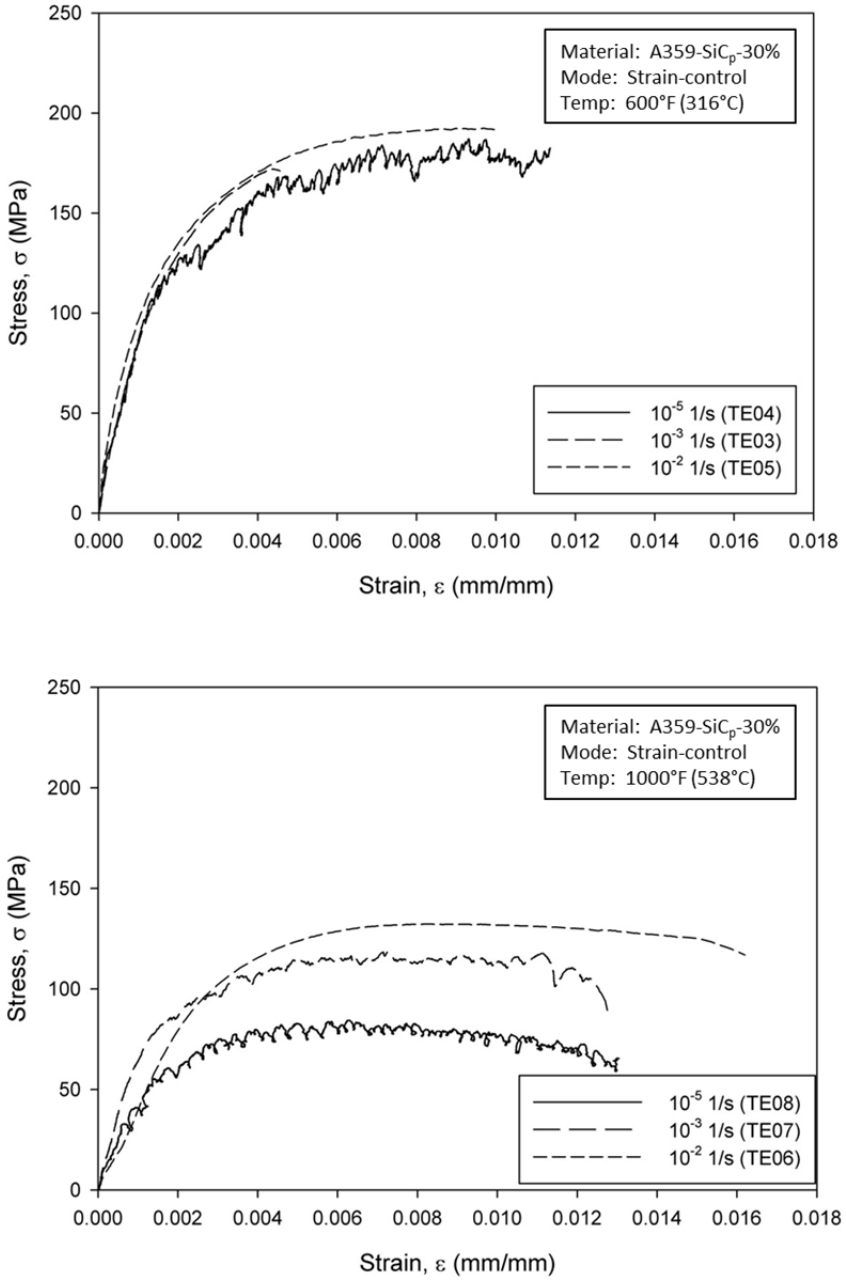

Figure 2.6: Strain rate dependence of tensile response of A359-SiC_p-30% at various temperatures.

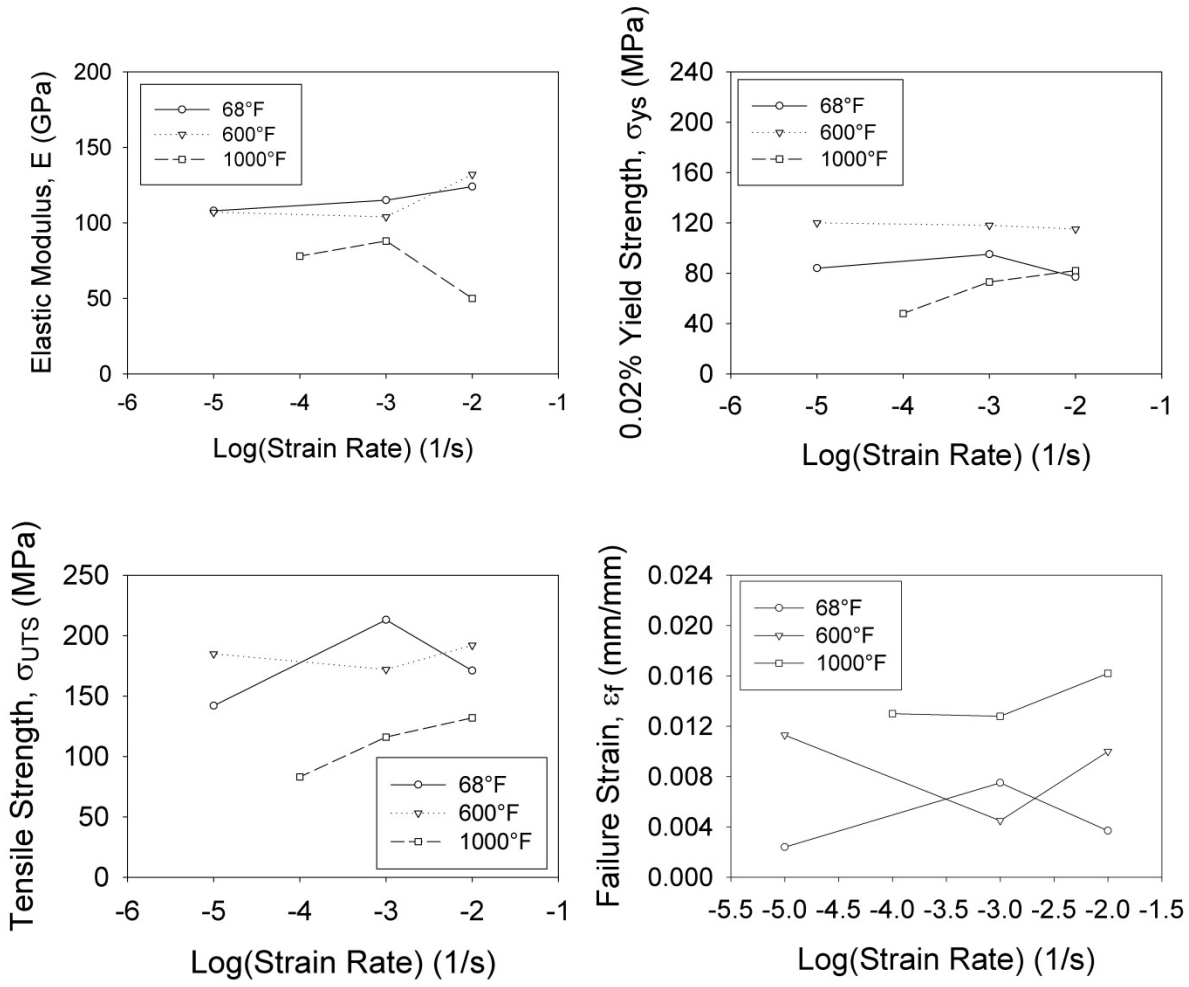

Figure 2.7: Rate dependence of tensile properties of A359-SiC_p-30%.

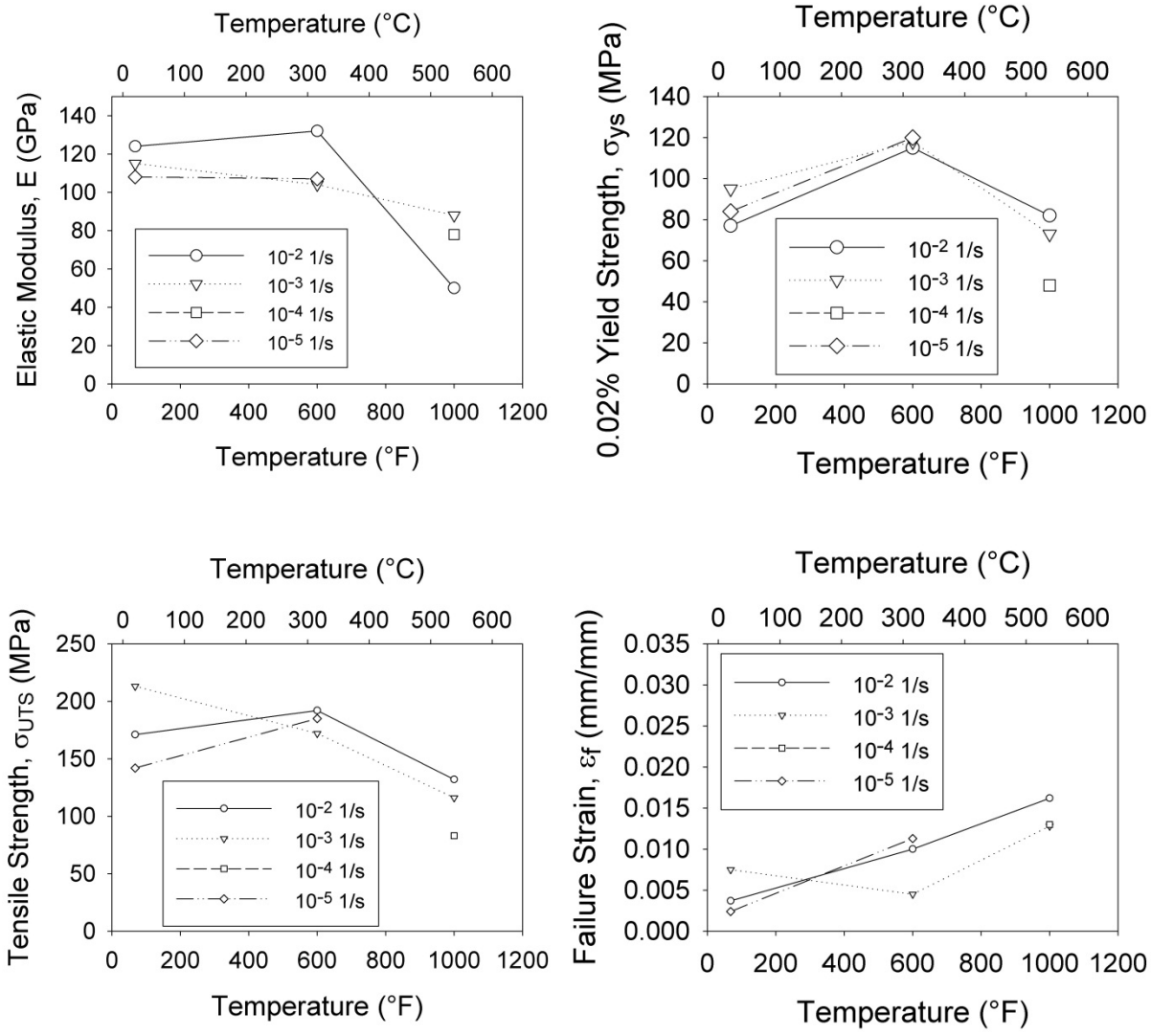

Figure 2.8: Temperature dependence of tensile properties of A359-SiCp-30%.

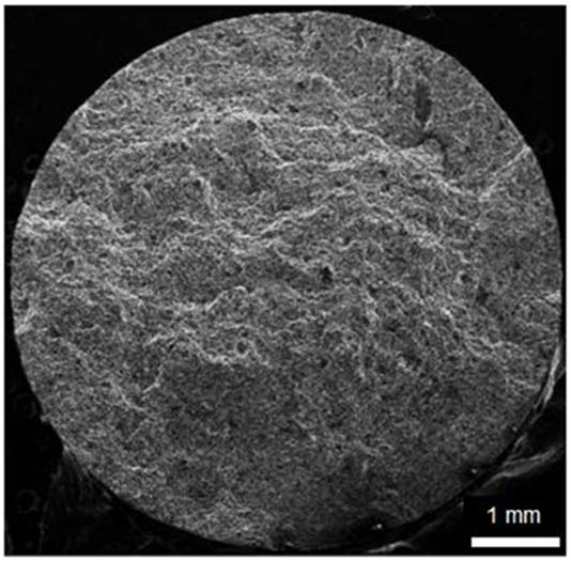

Figure 2.9: Secondary electron micrograph from the fracture surface of composite in the as-cast condition tested at 10^{-3} s^{-1} and 1000°F (538°C).

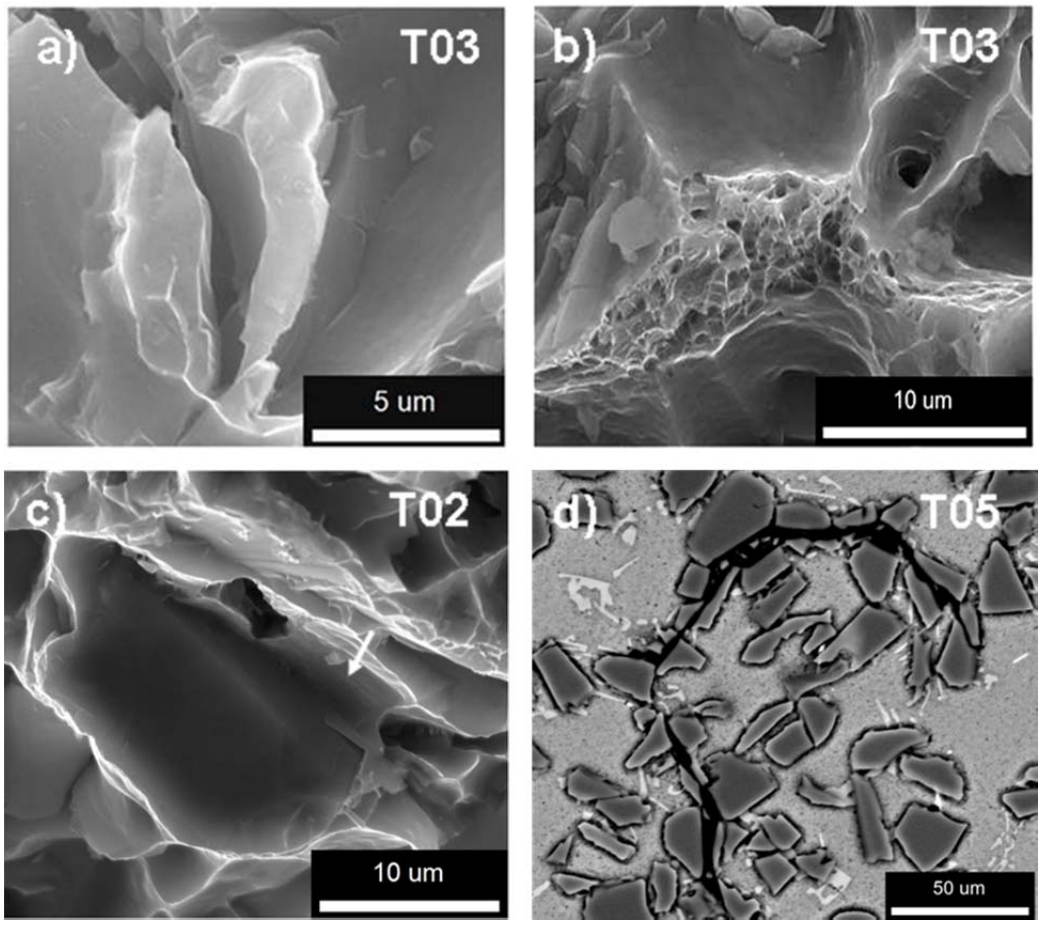

Figure 2.10: (a-c) Secondary and (d) backscatter electron micrographs illustrating the various characteristic of fracture in tensile tested A359-SiC_p-30%.

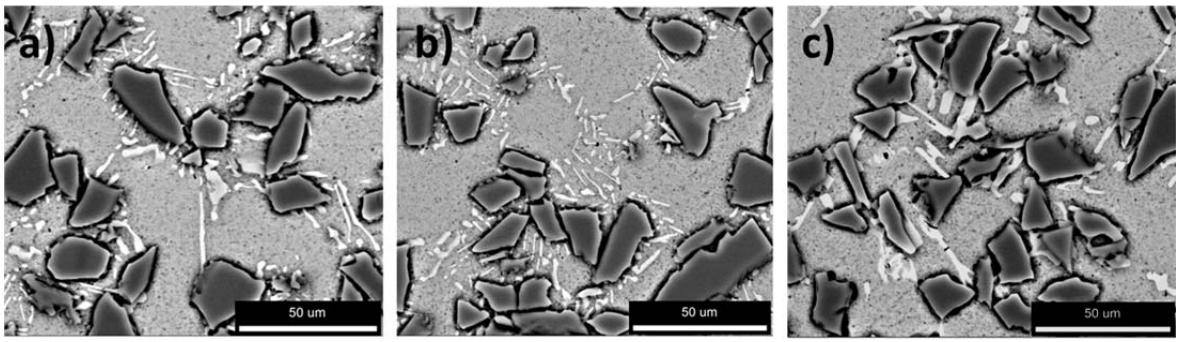

Figure 2.11: Backscatter electron micrographs of evolving Si-eutectic morphology in A359-SiC_p-30%.

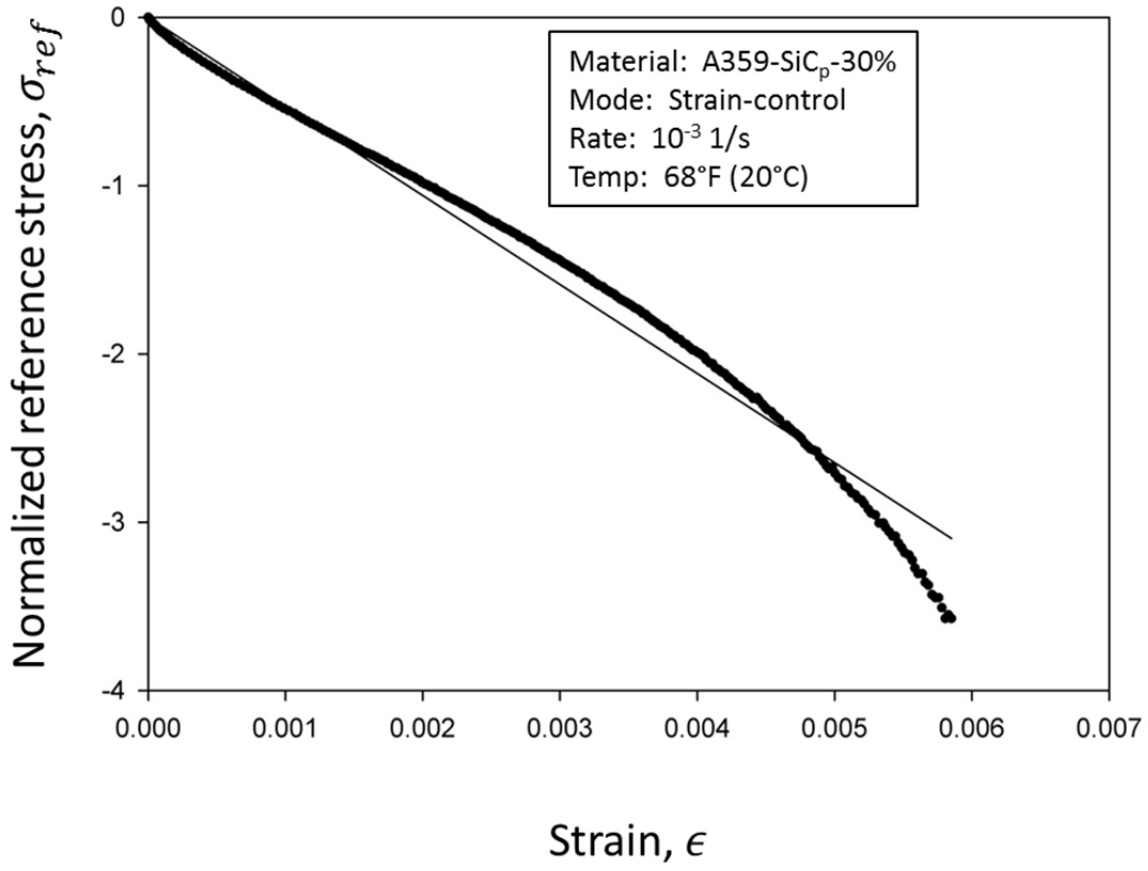

Figure 2.12: Linear regression for determination of stress-hardening parameter b.

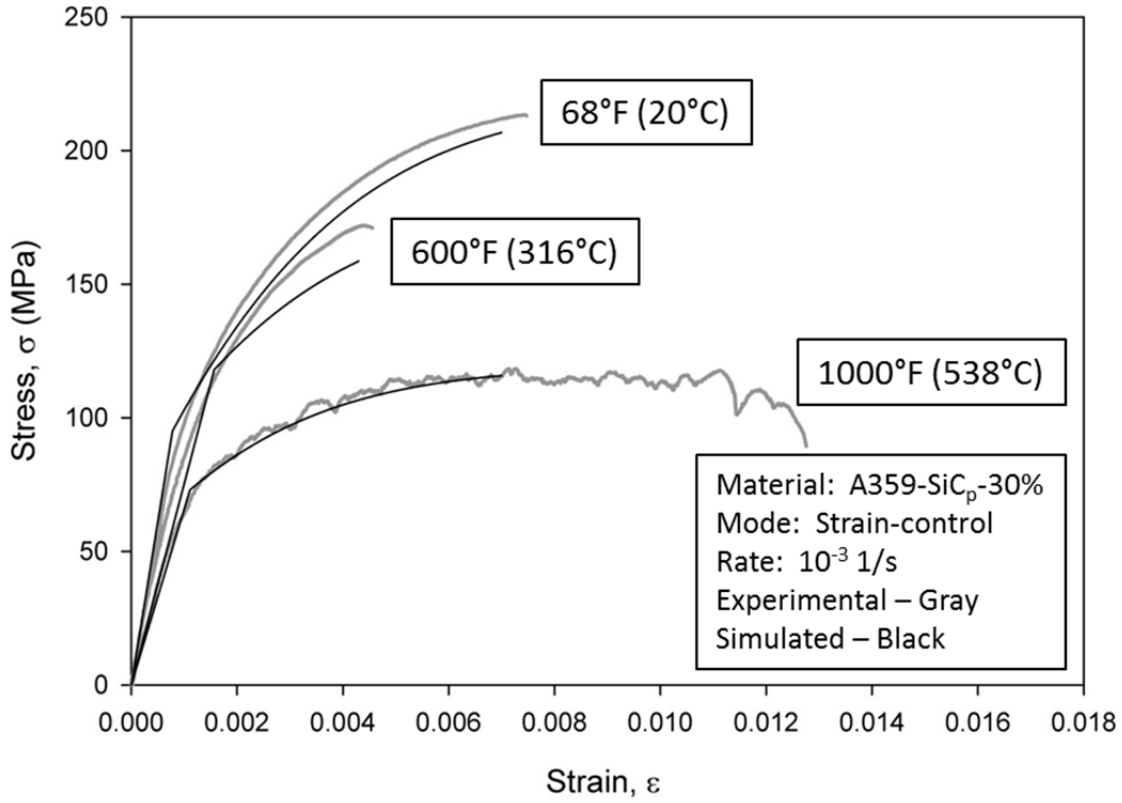

Figure 2.13: Comparison of simulated and experimental tensile response of A359-SiC_p-30% at various temperatures at a strain rate of 10^{-3} s^{-1}.

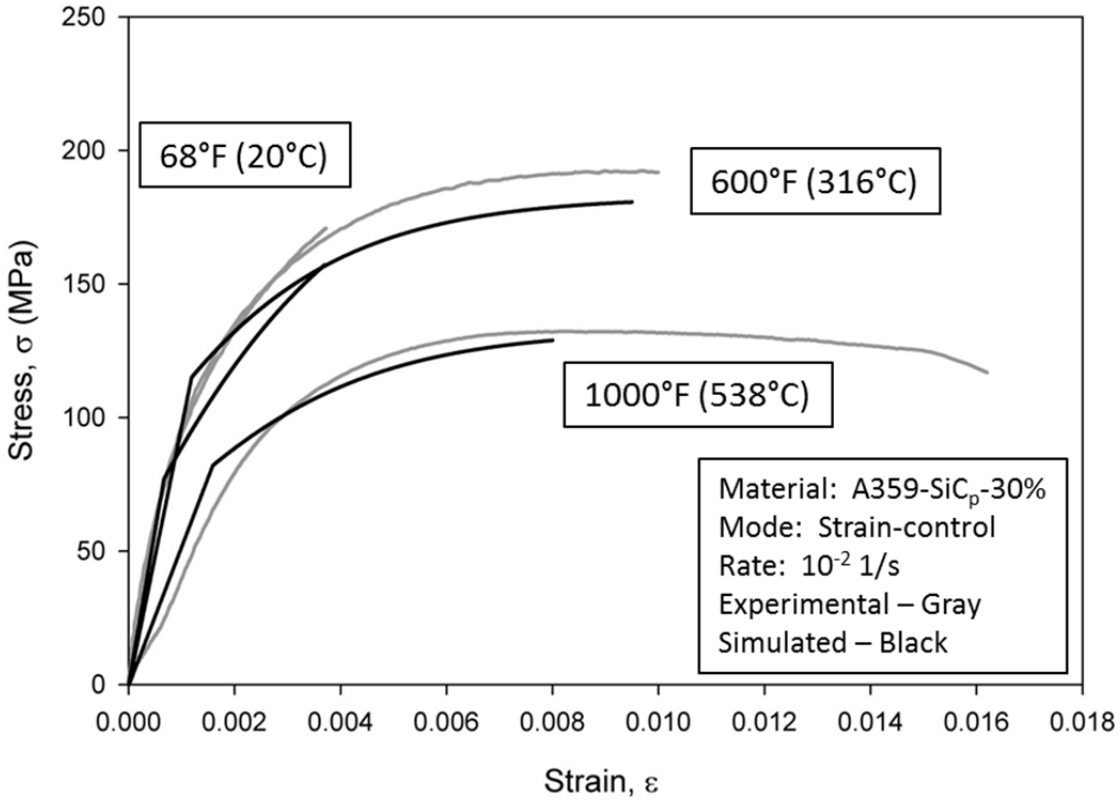

Figure 2.14: Comparison of simulated and experimental tensile response of A359-SiC_p-30% at various temperatures at a strain rate of 10^{-2} s^{-1}.

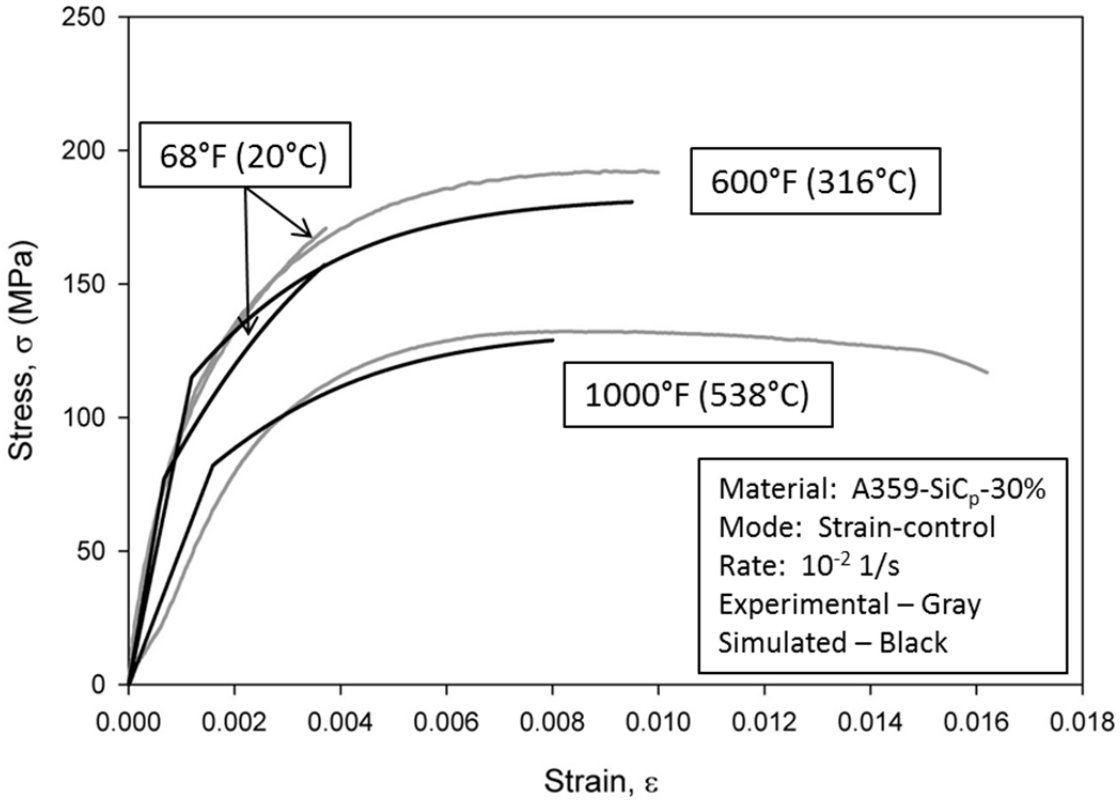

Figure 2.15: Comparison of simulated and experimental tensile response of A359-SiC_p-30% at various strain rates at 1000°F (538°C).

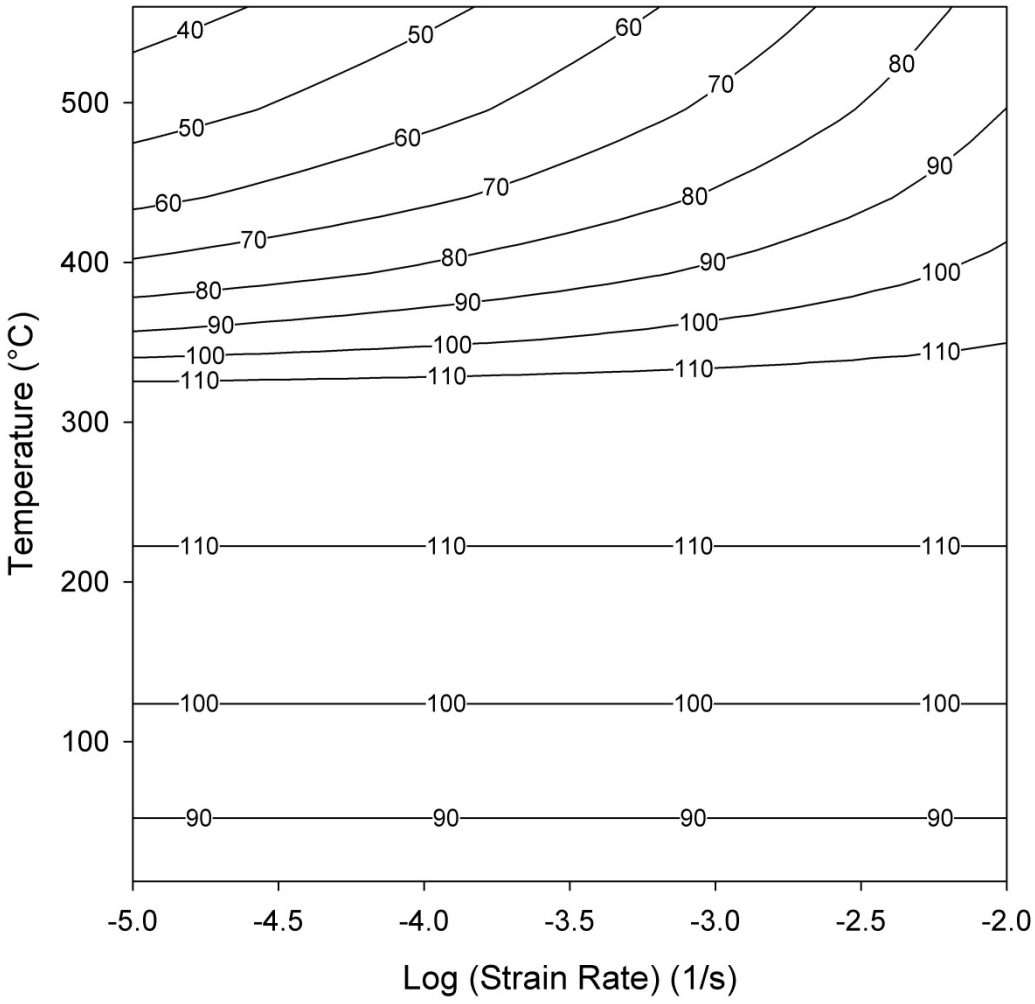

Figure 2.16: Simulated rate and temperature dependence of the yield strength, σ_{ys}, of A359-SiC_p-30%.

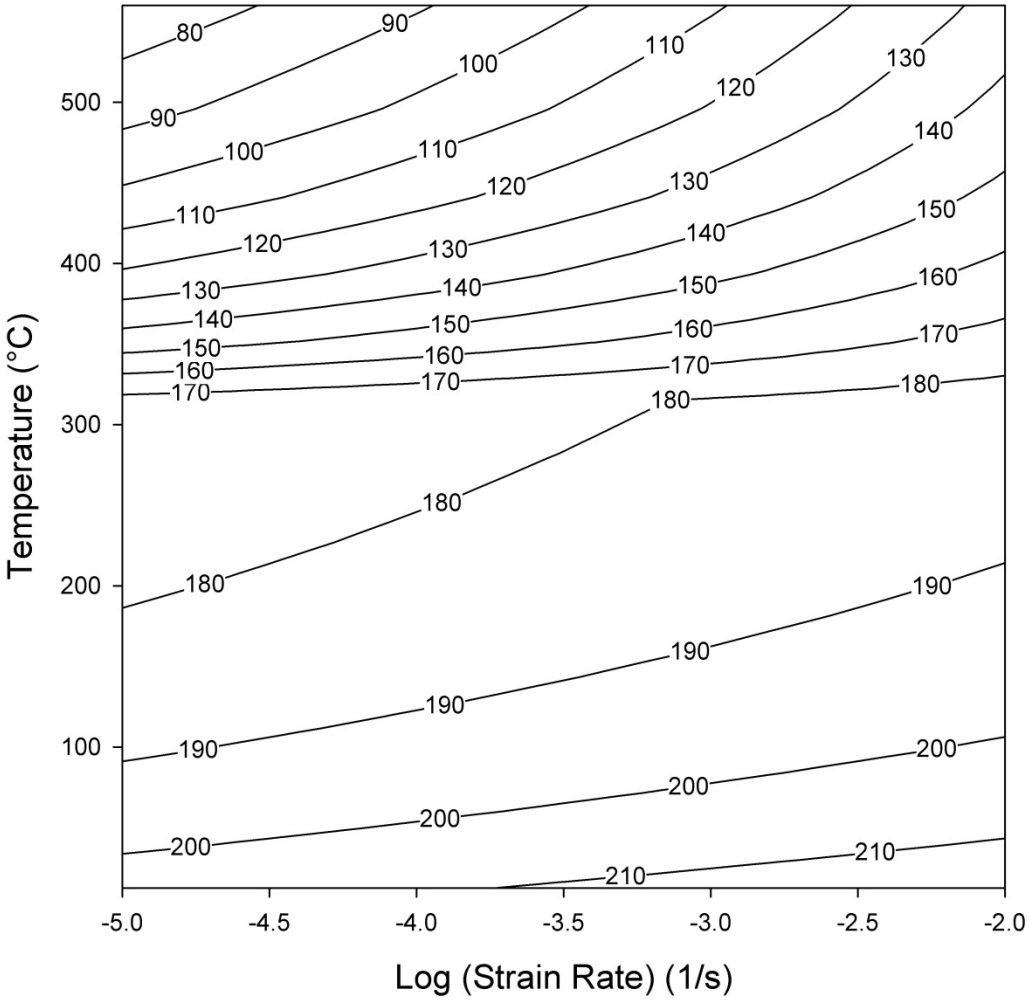

Figure 2.17: Simulated temperature and rate dependence of the saturated stress, σ_s, of A359-SiC_p-30%.

CHAPTER 3: CHARACTERIZATION OF THE TORSIONAL RESPONSE OF AS-CAST A359-SiC_p-30% AT ELEVATED TEMPERATURES

Characterization of the torsional response of as-cast A359-SiC_p-30% at elevated temperatures. By James DeMarco, Justin Karl, Yongho Sohn, Ali P. Gordon

The contents of this chapter will be submitted for publication in the Journal of Materials Processing Technology

3.1 Abstract

Aluminum metal-matrix composites are lightweight materials that have the potential to supplant steel in many applications. The current work helps to identify the parameters that confer maximal strength and ductility. Torsion tests were performed on the as-cast aluminum metal-matrix composite A359-SiC_p-30% at a variety of temperatures and twist rates. Dependence of material properties on temperature and strain rate were identified from equivalent stress-strain curves constructed from the reduced data. Examination of the microstructure was performed on the as-cast material and on fracture surfaces. A temperature- and strain rate-dependent constitutive model was applied to simulation of the mechanical response of the torsion specimen. Trends in material properties corroborate and extend trends identified previously under tensile loading with regard to temperature and strain rate dependence. (Something about microstructure.) Shear properties of simulated specimens generally agree with properties obtained through experimentation.

Keywords: metal-matrix composites, mechanical characterization, temperature-dependent modeling, strain-dependent modeling, hot rolling simulation

3.2 Introduction

Aluminum metal-matrix composites (Al-MMCs) have become increasingly popular in recent years. While unreinforced aluminum alloys have low densities and high ductilities, they are not suitable for many applications due to their lack of strength and stiffness. To provide added strength and stiffness while maintaining favorable densities, it has become common to reinforce aluminum alloys with silicon carbide in various forms, although usually the inclusions are in the form of whiskers or particles. The result is a composite material with superior specific strength and stiffness. While whisker reinforced composites are expensive due to the necessity of processing by nonstandard techniques and have low transverse properties when rolled, particle reinforced Al-MMCs have transverse material property values almost as high as the longitudinal properties and are not as expensive to process as whisker-reinforced Al-MMCs [1].

As-cast sheets of silicon carbide particle-reinforced Al-MMC are rolled at elevated temperatures in order to break up silicon-carbide particles and redistribute them more uniformly throughout the sheet. During this process, material may be lost due to edge cracking, in which lateral expansion at the transverse edges of the billet results in the formation of cracks. Cracked material must be removed before further rolling, and the removed material is lost. Additional cost savings could be attained in the processing of particle-reinforced materials through the reduction of edge cracking.

The rolling process imparts compressive and torsional stresses on the rolled material. Under the assumption of isotropy, previous work by the authors sought to characterize the tensile response of a candidate Al-MMC at elevated temperatures and various strain rates in order to predict material response during rolling. In the current work, investigation is expanded to the torsional

response of specimens of as-cast A359-SiC_p-30%. Study of the response of reduced-size specimens of the as-cast material under carefully controlled conditions may provide insight into the determination of parameters for the hot rolling process such as roll rate, roll temperature, reduction ratio, and so on, as noted in [25]. Hot working simulation tests include tensile testing, uniaxial compression, cam plastometer testing, and torsion testing. Tensile testing and compression suffer from limiting instabilities of necking and barreling, respectively. Compression and cam plastometer testing do not allow determination of limits to workability. Hot torsion has no limiting instability, and materials may be tested under torsion to failure [25]. For these reasons, torsion testing is often considered the best choice for testing hot workability.

While identification of the material properties at various temperatures and strain rates may in itself be useful for increasing the efficiency of the rolling process, further insight may be gained by the incorporation of microexamination of fracture surfaces and numerical modeling. Microexamination may reveal the mechanisms responsible for material failure, or it may provide a microstructural explanation for improvements in material properties under various conditions. If failure mechanisms are temperature or strain rate dependent, this dependence may be evident in features or patterns identified through microexamination. Numerical modeling may provide insight into material response at temperatures and strain rates between those studied. Furthermore, if a constitutive model may be identified which provides a sufficiently accurate representation of material response under a variety of load configurations, temperatures and strain rates, it becomes possible to create a computational model of the rolling process in which geometries are represented exactly, and a parametric study of the rolling process may be

performed to identify the influence of temperature, strain rate, and other rolling parameters on the stresses and strains that result in the rolled sheet.

The remainder of this study is organized as follows. In Sec. 2, the experimental procedures employed for torsion testing, microexamination of fracture surfaces, and data reduction are described. In Sec. 3, a computational model of the mechanical response of the candidate material under torsion testing is developed. In Sec. 4, results of torsion experiments, microexamination, and numerical modeling are analyzed. Section 5 provides conclusions and avenues for future work.

3.3 Experimental Procedure

The material under examination is the aluminum metal-matrix composite A359-SiC_p-30%. Aluminum metal matrix composites are valued for having high specific stiffness. The matrix alloy, A359, is a high-silicon cast aluminum. Its chemical composition is given in Table 3.1. Previous studies of the composite or similar materials have addressed torsion [2], fracture [12], [26], [3], high-strain rate conditions [13] (compression), [27] (compression), [20] (tension), and creep [6], [7], [28]. However, previous studies have not examined the material as cast.

The microstructure of the composite shows four main regions: (i) solid solution fcc aluminum, (ii) α-SiC, (iii) eutectic silicon, and (iv) precipitates and dispersoids rich in magnesium and iron. The average size of silicon-carbide reinforcement particles is 17±5 μm, which is in agreement with measurements conducted in [11]. Distribution of silicon-carbide particles is non-uniform in the as-cast material, with some particle clustering and also some regions sparse in particles. The uneven distribution may be attributed to a combination of solidification shrinkage and

incomplete infiltration. Figure 3.1(a) shows the arrangement of SiC particles within the matrix in a sample region. Figure 3.1(b) shows the presence of eutectic silicon in the A359 matrix.

A series of mechanical tests were performed in order to provide data regarding the response of the candidate material to torsion loadings under a variety of conditions. This information is used in the characterization of the behavior of the material in general, as well as to establish correlations with previously-performed tensile experiments and computational results. Unprocessed slabs of material were machined by an ISO-9001 compliant facility into specimens with a 2.0 inch (50.8mm) long and 0.25 inch (6.35mm) diameter gage section. Additional relevant dimensions are illustrated in Fig. Figure 3.2.

Monotonic torsion tests were conducted under a variety of temperatures and strain rates. A total of 14 specimens of the as-cast material were tested in a static lab air environment on an MTS Bionix electromechanical load frame. Frame alignment was verified by the system manufacturer before testing, as an international standard has not yet been set. Torque and twist levels during each experiment were controlled and logged by an MTS Bionix control and acquisition system linked to a PC running MTS Systems' TestWorks4 software. Temperature was maintained to within 1°F (0.55°C) of the target temperature in the middle of the gage section during elevated temperature testing, illustrated in Fig. Figure 3.3.

A resistance-type furnace manufactured by the Mechanics of Materials Research Group (MOMRG) lab at the University of Central Florida (UCF) provided heat. Heat application was regulated via a thermocouple and Watlow temperature controller coupled to a programmable Xantrex power supply.

Monotonic tests were conducted by applying twist rates that matched equivalent strain rates of $0.001s^{-1}$, $1.0s^{-1}$, and $10.0s^{-1}$ at the effective radii. Specimen ends were free to strain axially without restraint or load. Experiments were conducted at both room temperature and elevated temperatures. A standard for this specific torsion application is not yet available, but testing complied with specifications from similar ASTM standards E143 [29] and A938 [30]. Elevated temperature testing was performed at 207°F (97.2°C), 359°F (181.7°C), 600°F (315.6°C), 625°F (329.4°C), 650°F (343.3°C), 675°F (357.2°C), and 1000°F (537.8°C) High temperature test procedures conformed to suggested heat soak times and other guidelines from ASTM standard E21 [16].

For the purposes of simulation of the torsion tests, it was necessary to determine whether a non-uniform temperature distribution along the length of the specimen had an influence on simulated results; to this end, temperatures were recorded every 6.35 mm (0.25 in) along the specimen surface by thermocouples for three different target temperatures: 316°C (600°F), 399°C (750°F) and 538°C (1000°F). The resulting distributions are shown in Fig. Figure 3.4.

(Any further microscopy description Dr. Sohn's group can offer)

Torsion experiments provide measurements of torque and twist, which must be converted into quantities for shear stress and strain prior to application in the calibration or testing of constitutive models. The method applied in the current work was introduced by Barraclough et al. in 1973 [31]. It involves the introduction of an effective radius for calculation of strain and strain rate. The shear stress is computed as

$$\tau = \frac{3M}{2\pi R^3}$$

where M is the torque measured at the load cell and R is the specimen radius in the gage section. The shear strain is estimated to be

$$\gamma = \frac{r_{ef}}{L}\theta$$

where $r_{ef} = 0.724R$ is the effective radius, θ is the angle of twist measured at the grip, and L is the length of the gage section. The von Mises criterion is used to convert shear quantities into equivalent tensile quantities, so that

$$\sigma_{eq} = \frac{3\sqrt{3}M}{2\pi R^3}$$

is the equivalent stress, and

$$\epsilon_{eq} = \frac{r_{ef}}{\sqrt{3}L}\theta, \dot{\epsilon}_{eq} = \frac{r_{ef}}{\sqrt{3}L}\dot{\theta}$$

are the equivalent strain and strain rate, respectively. Twist rates for torsion experiments were set to provide a specified equivalent strain rate by application of the above rate equation. Equivalent stress-strain curves were used to identify equivalent material properties for comparison with results obtained previously through tensile testing.

3.4 Computational Modeling

To study the hot rolling of as-cast A359-SiC_p-30%, it is necessary to understand the behavior of the material at arbitrary temperatures and strain rates in the range of interest. To this end, a constitutive model was developed which is both temperature- and strain rate-dependent. The model is based on classical Perzyna viscoplasticity [22]. Elastic behavior is linear; since the equivalent Young's modulus under torsion did not show significant temperature dependence, the modulus for the model was defined to be the average modulus determined for all experiments

performed. Inelastic response is assumed to be nonlinear, isotropic, temperature dependent and strain rate dependent, with an onset yield strength which is temperature dependent at low temperatures and temperature and strain rate dependent at high temperatures.

The flow stress is based on that of Zhou and Clode [9]. It is defined as

$$K\left(\alpha;\dot{\alpha}_{avg},T\right)=\sigma_{ys}(\dot{\alpha}_{avg},T)+\sigma_{ZC}\left(\alpha;\dot{\alpha}_{avg},T\right)$$

where σ_{ys} is to be determined and

$$\sigma_{ZC}=C[1-\exp(-b\alpha)]\sinh^{-1}\left[B\dot{\alpha}^{m}\exp\left(\frac{Qm}{kT}\right)\right]$$

is the von Mises stress of the Zhou-Clode model. The hardening parameter b in the above is assumed to depend on the temperature-compensated strain rate, $Z_{\epsilon}=\dot{\epsilon}\exp\left(\frac{Q}{kT}\right)$, as follows:

$$b=\alpha_{b}Z_{\epsilon}^{\beta_{b}}$$

In order to complete the model, several parameters must be determined. These parameters, along with their influence on the resulting model, are shown in Table 3.2. The parameters were calibrated to provide the best model for the candidate material by extracting material properties from a series of tensile tests, as described in [ref to JAM article]. The tests performed to calibrate the model are listed in Table 3.3. Properties of the as-cast AlMMC were determined at several temperatures and strain rates.

The Levenberg-Marquardt algorithm was used to identify the flow stress parameters C, B, m, and Q that provide the best fit to strain rate and temperature dependence data. Since the flow stress is not activated until the yield strength is reached, the saturated stress level of the flow is identified with the difference between ultimate strength and yield strength. This difference may

be obtained from the material properties extracted through tensile testing at different temperatures and rates. The Levenberg-Marquardt algorithm may then be applied to the data triples $(T, \dot{\epsilon}, \sigma_{UTS} - \sigma_{ys})$ over the set of temperatures and rates tested.

A user-programmable feature (UPF) in the ANSYS finite element suite was created to implement the model. The discrete version of the Perzyna formulation with the flow stress as specified above was implemented on the basis of algorithms given in Simo and Hughes [22] for nonlinear isotropic/kinematic J_2 plasticity and linear isotropic J_2 viscoplasticity.

To study the mechanical response of the test samples, a 3D model of the torsion specimen was constructed in ANSYS. Exact dimensions of the machined specimens were used. Geometry was created by rotation of a plane drawing of a radial slice of the test specimen, and twenty-node SOLID186 elements were chosen to provide a regular pattern for the mesh. In actual tests, test specimens are gripped by chucks at the grip section. One end is held fixed, and twist is applied at this end. The other end is free to move longitudinally, and torque is measured by a transducer at this end. Accordingly, for the computational model, the fixed end was established by setting all displacements to zero on the longitudinal surface of the grip section. The free end was prevented from expanding radially by imposition of a pressure on the radial surface of the grip section. The pressure was arbitrarily chosen to be between 30% and 70% of the material's yield strength at the given temperature. This was found to be sufficient to minimize radial expansion while avoiding plastic deformation at the grip. Longitudinal displacements at the free end were unconstrained. Twist was applied at this end through the use of the ANSYS node-to-surface contact algorithm. A pilot node was defined along the specimen axis but exterior to the specimen, and target nodes were set to be all nodes on the longitudinal surface of the free end

grip section. Through the resulting multipoint contact (MPC) elements defined internally by ANSYS, a rotation applied at the pilot node was conveyed to the longitudinal surface nodes, resulting in a twist about the specimen axis. Simulations consisted of applying a twist at least as large as the twist associated to maximum torque for the specimen under consideration. The geometry, mesh, and boundary conditions are illustrated in Fig. Figure 3.5

As noted in the previous section, temperature distributions along the specimen length were determined at each of three target temperatures. The resulting data were fitted by a function

$$T = T(T_0, y)$$

where T_0 is the target temperature and y is the axial distance in millimeters from the fixed end of the specimen. For $|y - 50.8| < 19.05$, the distribution is defined by a best-fit surface to the temperature distribution data obtained at the target temperatures and a constant distribution imposed at room temperature, i.e., 20°C (68°F). This region corresponds to the gage section of the specimen, which is fully enclosed by the furnace. The temperature distribution is defined to be quadratic in y and T_0 in this portion of the specimen. For $|y - 50.8| \in [19.05,50.8]$, a similar approach is taken, with the resulting distribution defined as the maximum of 20°C (68°F) and a best-fit function to the temperature distribution data and a constant distribution imposed at room temperature which is linear in y and quadratic in T_0, and which is required to produce the same temperature at $|y - 50.8| = 19.05$ as the distribution obtained in the gage section. The surface fits were obtained via user functions created in TableCurve3D. The surface and data points for the gage section are shown in Fig. Figure 3.6. The temperature distribution is defined in such a way that the user of the simulation software needs to specify only the target

temperature, and the distribution is imposed automatically. For simulations below 24°C (75°F), the distribution is defined to be constant.

3.5 Results

Experiments performed on A359-SiC_p-30% on the MTS Bionix torsion load frame resulted in torque and twist histories for each temperature and twist rate configuration studied. These histories were used to construct torque-twist, shear stress-strain, and equivalent stress-strain diagrams for each specimen. Shear and equivalent data were obtained by the method described in Sec. 2. The matrix of tests performed and material properties obtained under torsion is shown in Table 3.4. The resulting equivalent material properties were plotted against equivalent strain rate and temperature and compared to tensile material properties obtained previously (see Table 3.3).

Shear stress-shear strain curves produced from the reduced data show marked differences at varying strain rates and temperatures. In Fig. Figure 3.7, it may be observed that temperature has a less pronounced effect on the shear response when the strain rate is high, which indicates an interaction of the strain rate and temperature dependences. Fig. Figure 3.8 shows that, conversely, increased temperature leads to greater variation of the stress response with strain rate.

It is possible to identify further trends in the mechanical response through comparison of material properties obtained through torsion and tension testing at different strain rates and temperatures. Plots of the dependence of various properties on strain rate are shown in Fig.

Figure 3.9, and dependence on temperature is shown in Fig. Figure 3.10; trends noted in the material properties are discussed below.

Elastic modulus clearly decreased at high temperature under tension, although the equivalent elastic modulus determined in torsion showed little if any consistent decrease with temperature. Equivalent elastic moduli remained around 75±15 GPa at all temperatures. In neither torsion nor tension did the elastic modulus show a consistent trend with strain rate.

The 0.02%-offset yield strength [32] was chosen to mark the onset of plasticity, due to the low ductility of the material at low temperatures. Yield strengths increased consistently with strain rate at high temperatures only under tension. Under torsion, yield strengths were flat between 10^{-3} s^{-1} and 10^{0} s^{-1} but increased at all three temperatures studied between 10^{0} s^{-1} and 10^{1} s^{-1}. Yield strength increase at high strain rate was slight at 20°C (68°F) and substantial at 538°C (1000°F). Of more interest is the trend in yield strength with temperature. Under both tension and torsion and at all rates studied, 0.02%-offset yield strengths peaked near 316°C (600°F). Increases between 20°C (68°F) and 316°C (600°F) were less substantial under torsion than under tension, but the trend is still apparent. Yield strengths dropped off significantly above 316°C (600°F) under both load scenarios.

Despite the peak in yield strengths in the vicinity of 316°C (600°F), ultimate strengths nevertheless generally decreased with increasing temperature for the temperatures and rates studied. Exceptions to this occurred at 20°C (68°F) at strain rates of 10^{-3} s^{-1} and 10^{-2} s^{-1} under tension. However, early failure of the specimen (prior to stress saturation) is the probable cause for these exceptions, as the material is rather brittle at low temperatures and is therefore more prone to rupture, particularly at high strain rates. As a function of strain rate, ultimate strengths

followed the trends identified for yield strengths. A consistent increase in ultimate strength with strain rate was observed only at high temperature under tension, and ultimate strength was flat with increasing rate up to 10^0 s^{-1}, with temperature-dependent increases at 10^1 s^{-1}. The increase in ultimate strength between 10^0 s^{-1} and 10^1 s^{-1} for elevated temperatures was much larger than the increase in yield strength in this range of strain rates.

Failure strain was defined to be the strain level attained at the last data point prior to a 50% or greater drop in the stress below the ultimate stress level. Although wide scatter in failure strain data as a function of strain rate was observed under both torsion and tension, a general trend of increasing failure strain with strain rate was noted particular for elevated temperature torsion. With the exception of the same cases of early failure noted with regard to ultimate strengths, failure strains at all rates reached a minimum around 316°C (600°F). Particularly at the higher strain rates for each test regime, failure strain increased substantially between 316°C (600°F) and 538°C (1000°F).

Any microstructural examination results/observations should go here.

Simulated shear stress-strain curves were obtained in two ways. The first method was to capture the data at a surface node on the lengthwise midplane of the specimen at each step of the simulation. The location of the node used for data capture is shown in Fig. Figure 3.5. The second method was to obtain time histories of the y-axis rotation and y-axis reaction torque at the pilot node, which were then converted by standard mechanics of materials formulas to shear stress and strain histories.

Simulations were performed both with and without the imposition of temperature distributions discussed in the previous section; in the latter case, the temperature at all nodes was set to the

target temperature regardless of position. Figure 3.11 shows simulated and experimental shear stress-strain curves for tests performed at 316°C (600°F) and 538°C (1000°F) and an equivalent strain rate of 10^0 s^{-1}. The simulated stress levels obtained under a distributed temperature distribution were lower or nearly the same in all cases examined in the plastic regions of the curves. However, since simulations under a constant distribution do not show a systematic bias toward higher stress levels than obtained through experimentation, the use of a temperature distribution does not in general improve the accuracy of simulations. Also, the model was calibrated under the assumption of constant temperature via tensile testing in which a similar furnace was used to heat the specimen. Since a similar temperature distribution to that identified in the torsion specimens may be presumed for the tension experiments, it may be expected that calibration performed by the aid of data obtained from such experiments under the constant-temperature assumption should be no less accurate for the torsion tests under a constant temperature assumption than for tests simulated with a temperature distribution in place. Furthermore, the temperature distribution is dependent on the specimen geometry, specifics of the furnace, and possibly other factors; therefore any distribution obtained in the current study may differ from those obtained elsewhere, so that findings based on a temperature-distributed model may not be considered to be general. On the basis of these considerations, the remainder of the results described in this section are obtained using a constant temperature distribution throughout the specimen.

Data obtained by direct acquisition of shear stress and strain at the specimen surface at the midplane of the gage section were found to be in better agreement with experimental data in the hardening portion of the shear stress-strain curve than data obtained through reduction of torque

twist data obtained at the pilot node. While saturated stresses obtained by either method were nearly the same, in the hardening portion of the curve shear strains obtained through reduction were lower than those obtained directly in the gage section, as may be seen in Fig. Figure 3.12. Since in most cases experimental data showed lower shear strains for the same level of shear stress than even the directly-captured shear stress-strain data, the data captured at the gage surface were considered to be superior to that obtained through reduction of torque and twist from the pilot node. The remainder of the simulation results presented here are obtained directly from the gage surface, unless stated otherwise.

Shear stress and von Mises stress contours at saturated stress were obtained at the specimen surface and at a transverse cross section at the midplane of the specimen. The shear and von Mises contours at the specimen surface for a simulation performed at 538°C (1000°F) and an equivalent strain rate of 10^0 s^{-1} are shown in Fig. Figure 3.13. The contours were obtained after a rotation of 0.5 rad. It may be observed that the von Mises stress is essentially uniform in the gage section, does not depend on angle, and reduces as the radius expands throughout the rest of the model. Shear stress is also maximum in the gage section, although since the xy-component was chosen to represent shear stress, the value at a given point on any circumference depends on its angle with respect to the x-axis. Cross section contours at the specimen midplane are shown in Fig. Figure 3.14 for the same test conditions. The cross section for von Mises stress shows that the stress is saturated or nearly saturated throughout most of the specimen, and drops quickly to zero in the interior closest to the specimen axis, where the amount of circumferential displacement is relatively low.

Simulations of torsion tests were performed at constant temperatures of 20°C (68°F), 316°C (600°F) and 538°C (1000°F) and at equivalent strain rates of 10^{-3} s^{-1}, 10^{0} s^{-1}, and 10^{1} s^{-1}, and the resulting shear stress-strain curves were plotted on the same sets of axes, along with experimental data. Figure Figure 3.15 shows that while the simulated response diverges somewhat from the experimental results in the hardening portion of the curve, the simulations reliably reproduce acceptable approximations of the ultimate stress at each temperature. Simulations performed at the highest temperature studied, at which strain rate dependence is expected to be most significant, show that the rate dependence is captured well at rates which were used to calibrate the model, while underestimating the stress levels obtained at the highest rate, as may be observed in Fig. Figure 3.16. It may also be seen that the shape of the hardening curves match well for the two lower-rate cases. In general, however, hardening was seen to occur at a greater rate in simulations than in actual tests. A difference in the rates of hardening in torsion versus tension testing has been observed repeatedly, as noted in [25], and may be due to a difference in the effective strain rate under torsion as opposed to tension. Since rate dependence of the hardening parameter was calibrated under tension for the numerical model employed, the greater rate of hardening observed in simulations may be explained by the adherence of the model to hardening rates observed under tension.

3.6 Conclusions

Torsion experiments were performed on the as-cast aluminum metal-matrix composite A359-SiC_p-30% at a variety of temperatures and twist rates. The torque and twist histories obtained from the test apparatus were reduced to shear and equivalent stress and strain histories by application of the effective radius and von Mises equivalents. Stress-strain diagrams were

constructed for the shear and equivalent quantities. These were used to determine equivalent material properties for the material, which were compared with properties previously obtained through tensile testing. The strain rate and temperature dependence of material properties were analyzed to determine trends.

A numerical model which was defined and calibrated to simulate the tensile response of the material was applied to simulate torsion tests at various twist rates and temperatures. The mesh used in simulations was a 3-D replica of the torsion specimen, and simulations were conducted with and without the imposition of experimentally-determined temperature distributions. Imposition of the temperature distribution was not found to improve accuracy of simulations. It is believed that this is due to the fact that the material model was calibrated using tensile data that was obtained under the assumption of a uniform temperature distribution, even though actual temperatures may have been similarly distributed. Shear stress-strain data was captured at the model specimen gage surface and also through the reduction of torque-twist data obtained from the pilot node used to twist the free end of the specimen model. Data obtained directly from the gage surface was found to provide shear stress-strain curves more closely aligned with experimental data than those obtained by reduction of torque-twist data at the pilot node. Simulated shear stress-strain curves produced under varying temperature and strain rate conditions sufficiently matched trends in experimental data to allow prediction of material response at intermediate temperatures throughout the range of temperatures studied, and at intermediate strain rates in the 10^{-3}-10^{0} s^{-1} range.

3.7 References

[1] K. Park, J. E. Lavernia, and F. A. Mohamed, "High temperature creep of silicon carbide particulate reinforced aluminum," *Acta metallurgica et materialia*, vol. 38, no. 11, pp. 2149-2159, 1990.

[2] Y. Li, K. T. Ramesh, and E. S. C. Chin, "The mechanical response of an A359/SiCp MMC and the A359 aluminum matrix to dynamic shearing deformations," *Materials Science and Engineering A*, vol. 382, pp. 162-170, 2004.

[3] R. Rodríguez-Castro, R. C. Wetherhold, and M. H. Kelestemur, "Microstructure and mechanical behavior of functionally graded Al A359/SiCp composite," *Materials Science and Engineering A*, vol. 323, pp. 445-456, 2002.

[4] M. Song, "Effects of volume fraction of SiC particles on mechanical properties of SiC/Al composites," *Transactions of Nonferrous Metals Society of China*, vol. 19, pp. 1400-1404, 2009.

[5] M. Song, "Effects of volume fraction of SiC particles on mechanical properties of SiC/Al composites," *Transactions of Nonferrous Metals Society of China*, vol. 19, pp. 1400-1404, 2009.

[6] O. A. Hamed, M. A. Shady, and A. R. El-Desouky, "Creep behavior of a cast 359/SiC/10p aluminum composite," *Materials and Design*, vol. 22, pp. 473-479, 2001.

[7] N. P. Hung, C. S. Lim, Y. K. Ho, Y. C. Tan, and W. G. Tan, "Cumulative creep and hot isostatic pressing of particle-reinforced metal matrix composites," *Journal of Materials Processing Technology*, vol. 101, pp. 104-109, 2000.

[8] P. K. Rohatgi, R. B. Thakkar, J. K. Kim, and A. Daoud, "Scatter and statistical analysis of tensile properties of cast SiC reinforced A359 alloys," *Materials Science and Engineering A*, vol. 398, pp. 1-14, 2005.

[9] M. Zhou and M. P. Clode, "Hot torsion tests to model the deformation behavior of aluminum alloys at hot working temperatures," *Journal of Materials Processing Technology*, vol. 72, pp. 78-85, 1997.

[10] C. Triveño Rios, C. Bolfarini, W. J. Botta F., and C. S. Kiminami, "Rapidly Solidified Al-Si-Mg Alloy," *Journal of Metastable and Nanocrystalline Materials*, pp. 594-598, 2004.

[11] W. H. Hunt, D. M. Schuster, M. D. Skibo, M. T. Smith, and D. R. Herling, "Lower Cost Cast Aluminum MMC Process and Products," in *State of the art in cast metal matrix composites in the next millenium; proceedings of a symposium*, 2000, pp. 265-272.

[12] D. P. Myriounis, S. T. Hasan, N. M. Barkoula, A. Paipetis, and T. E. Matikas, "Effects of Heat Treatment on Microstructure and the Fracture Toughness of SiCp/Al Alloy Metal Matrix Composites," *Journal of advanced materials*, vol. 41, no. 3, pp. 18-27, 2009.

[13] Y. Li, K. T. Ramesh, and E. S. C. Chin, "Viscoplastic Deformations and Compressive Damage in an A359/SiCp Metal-Matrix Composite," *Acta mater.*, vol. 48, pp. 1563-1573, 2000.

[14] ASTM, *ASTM E-1012-05. "Standard Practice for Verification of Test Frame and Specimen Alignment Under Tensile and Compressive Axial Force Application"*. West Conshohocken, PA, vol. 03.01.

[15] ASTM, *ASTM E8/E8M-08. "Standard Test Methods for Tension Testing of Metallic Materials"*. West Conshohocken, PA, vol. 03.01.

[16] ASTM, *ASTM E21-09. "Standard Test Methods for Elevated Temperature Tension Tests of Metallic Materials"*. West Conshohocken, PA, vol. 03.01.

[17] J. G. Kaufman and E. L. Rooy, *Aluminum Alloy Castings: Properties, Processes, and Applications*. Materials Park, OH: ASM International, 2004.

[18] P. Rodriguez, "Serrated plastic flow," *Bulletin of Material Science*, vol. 6, no. 4, pp. 653-663, September 1984.

[19] J. Sarkar and M. K. Surappa, "Serrated yielding in thermomechanically processed 6061 Al-SiCp composite," *Journal of Materials Science Letters*, pp. 835-837, 1994.

[20] Y. Li, K. T. Ramesh, and E. S. C. Chin, "Plastic Deformation and Failure in A359 Aluminum and an A359-SiCp MMC under Quasistatic and High-strain-rate Tension," *Journal of Composite Material*, vol. 41, pp. 27-40, 2007.

[21] E. Ogris, A. Wahlen, H. Luchinger, and P. J. Uggowitzer, "On the silicon spheroidization in Ai-Si alloys," *Journal of Light Metals*, vol. 2, pp. 263-269, 2002.

[22] J.C. Simo and T.J.R. Hughes, *Computational Inelasticity*, 1st ed., J.E. Marsden, L. Sirovich, and S. Wiggins, Eds. New York, U.S.A.: Springer-Verlag, 1998.

[23] C. T. Kelley, *Iterative Methods for Optimization*. Philadelphia: Society for Industrial and Applied Mathematics, 1999, Also available at http://www.siam.org/books/textbooks/fr18_book.pdf.

[24] J. J. Moré, B. S. Garbow, and K. E. Hillstrom, "User Guide for MINPACK-1," Argonne National Laboratory, Argonne, ANL-80-74, 1980.

[25] G. E. Dieter, H. A. Kuhn, and S. L. Semiatin, Eds., *Handbook of Workability and Process Design*. Materials Park, OH: ASM International, 2003.

[26] D. P. Myriounis, S. T. Hasan, and T. E. Matikas, "Microdeformation behaviour of Al-SiC metal matrix composites," *Composite Interfaces*, vol. 15, no. 5, pp. 495-514, 2008.

[27] Y. Li, K. T. Ramesh, and E. S. C. Chin, "The compressive viscoplastic response of an A359/SiCp metal-matrix composite and of the A359 aluminum alloy matrix," *International Journal of Solids and Structures*, vol. 37, pp. 7547-7562, 2000.

[28] A. Madgwick, C. Ungpinitpong, T. Mori, and P. J. Withers, "Observation and quantitative analysis of damage caused by creep in an Al A359/SiCp composite," *Materials Science and Engineering A*, vol. 342, pp. 201-206, 2003.

[29] ASTM, *ASTM E143-02: Standard Test Method for Shear Modulus at Room Temperature*. West Conshohocken, PA.

[30] ASTM, *ASTM A938-07: Standard Test Method for Torsion Testing of Wire*. West Conshohocken, PA.

[31] D. R. Barraclough, H. J. Whittaker, K. D. Nair, and C. M. Sellars, "Effect of Specimen Geometry on Hot Torsion Test Results for Solid and Tubular Specimens," *Journal of Testing and Evaluation*, vol. 1, no. 3, pp. 220-226, May 1973.

[32] ASTM, *ASTM B598-09: Standard Practice for Determining Offset Yield Strength in*

Tension for Copper Alloys. West Conshohocken, PA.

3.8 Tables

Table 3.1: Chemical composition of A359

Si	Fe	Cu	Mn	Mg	Zn	Sn	(Trace)	Al
9.45	0.11	<0.006	<0.05	0.67	<0.05	0.02	0.2	Bal.

Table 3.2: Constitutive modeling constants for Zhou-Clode inelasticity model, as identified via tensile testing

Parameter	Units	Value	Significance
α_b	(unitless)	507.97	Scaling factor for temperature-compensated strain rate (TCSR) in strain hardening coefficient
B	s	1.202	Scaling factor for combined effect of rate and temperature
β_b	(unitless)	0.00315	Exponent for TCSR in strain hardening coefficient
C	MPa	15.06	Scaling factor for stress; does not affect rate or temperature dependence
m	(unitless)	0.1155	Exponent for combined effect of rate and temperature
Q	J/mol	175752.75	Exponent that differentiates effect of temperature from rate

Table 3.3: Tensile experiments performed on A359-SiC_p-30%

Spec. ID	Temp., T (°F (°C))	Strain Rate, $d\varepsilon/dt$ (s^{-1})
TE10	68 (20)	10^{-2}
TE02	68 (20)	10^{-3}
TE11	68 (20)	10^{-5}
TE05	600 (316)	10^{-2}
TE03	600 (316)	10^{-3}
TE04	600 (316)	10^{-5}
TE06	1000 (538)	10^{-2}
TE07	1000 (538)	10^{-3}
TE08	1000 (538)	10^{-4}

Table 3.4: Equivalent material properties of A359-SiC_p-30% identified through torsion testing

Specimen ID	Temperature (°C (°F))	Equivalent Strain Rate (s^{-1})	Equivalent Young's Modulus (MPa)	Equivalent 0.02%-Offset Yield Strength (MPa)	Equivalent Ultimate Strength (MPa)	Equivalent Strain to failure (mm/mm)
C2	20 (68)	10^{-3}	89	100	234	0.0162
C1	20 (68)	10^{0}	72	102	241	0.0233
C3	20 (68)	10^{1}	80	113	254	0.021
C19	97 (207)	10^{-3}	90	115	225	0.016
C20	182 (359)	10^{-3}	75	99	194	0.0138
C5	316 (600)	10^{-3}	77	101	194	0.0161
C18	316 (600)	10^{0}	75	109	181	0.0086
C4	316 (600)	10^{1}	61	122	227	0.0171
C27	357 (675)	10^{-3}	88	87	187	0.011
C25	343 (650)	10^{-3}	70	92	150	0.0141
C24	329 (625)	10^{-3}	64	73	131	0.0119
C23	538 (1000)	10^{-3}	61	62	103	0.0121
C21	538 (1000)	10^{0}	72	62	104	0.0218
C22	538 (1000)	10^{1}	65	90	194	0.0287

3.9 Figures

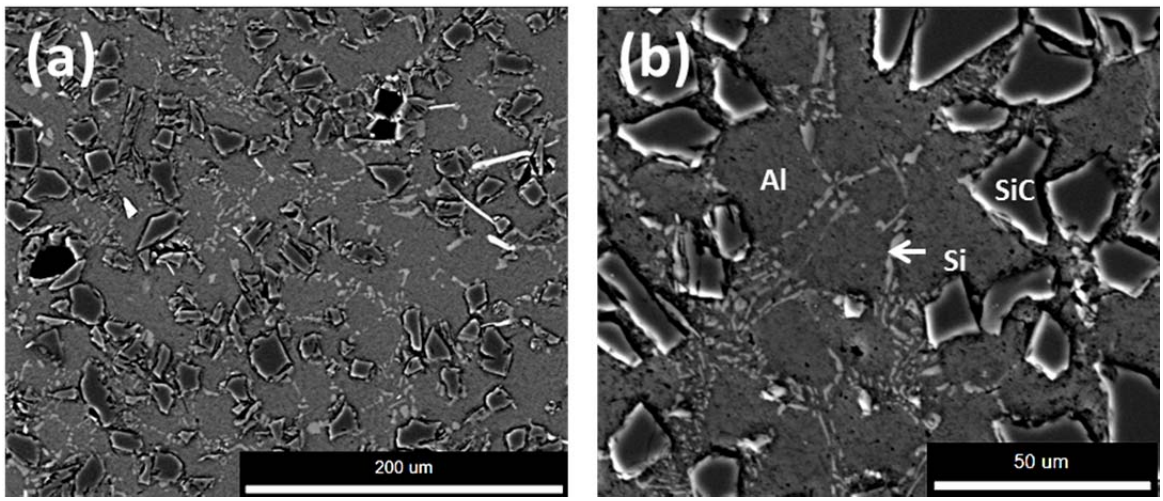

Figure 3.1: Microstructure of as-cast A359-SiC_p-30%

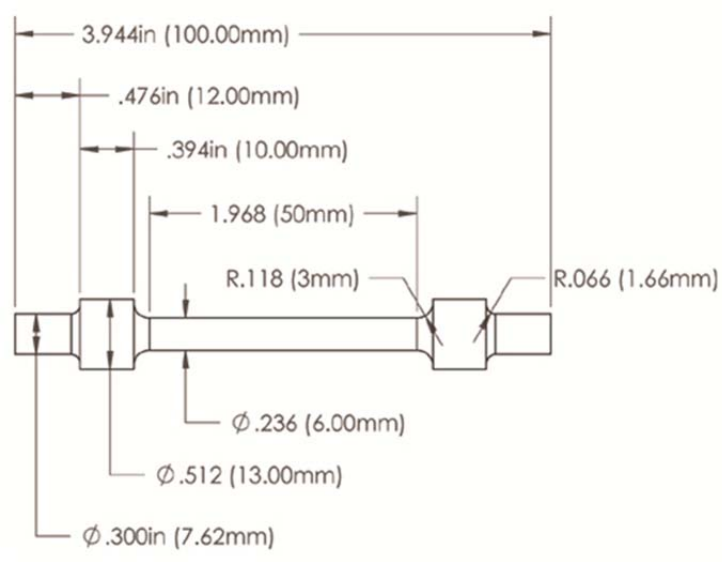

Figure 3.2: Torsion specimen dimensions

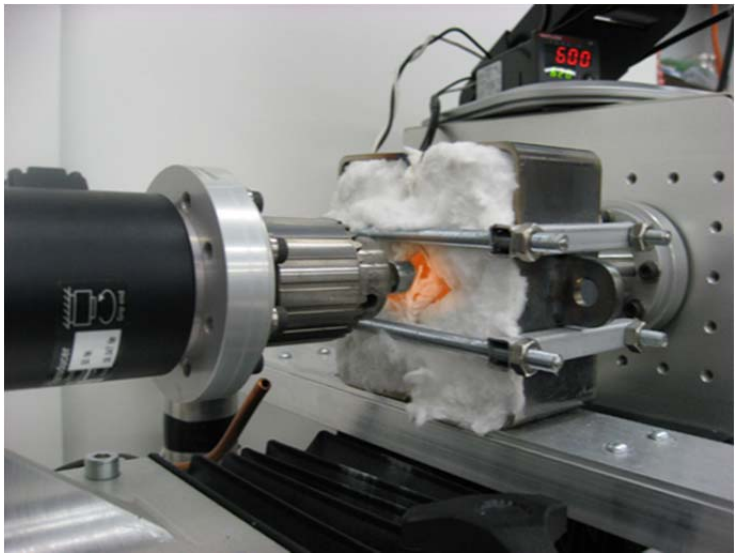

Figure 3.3: Profile of mechanical test specimen, heater, and extensometer

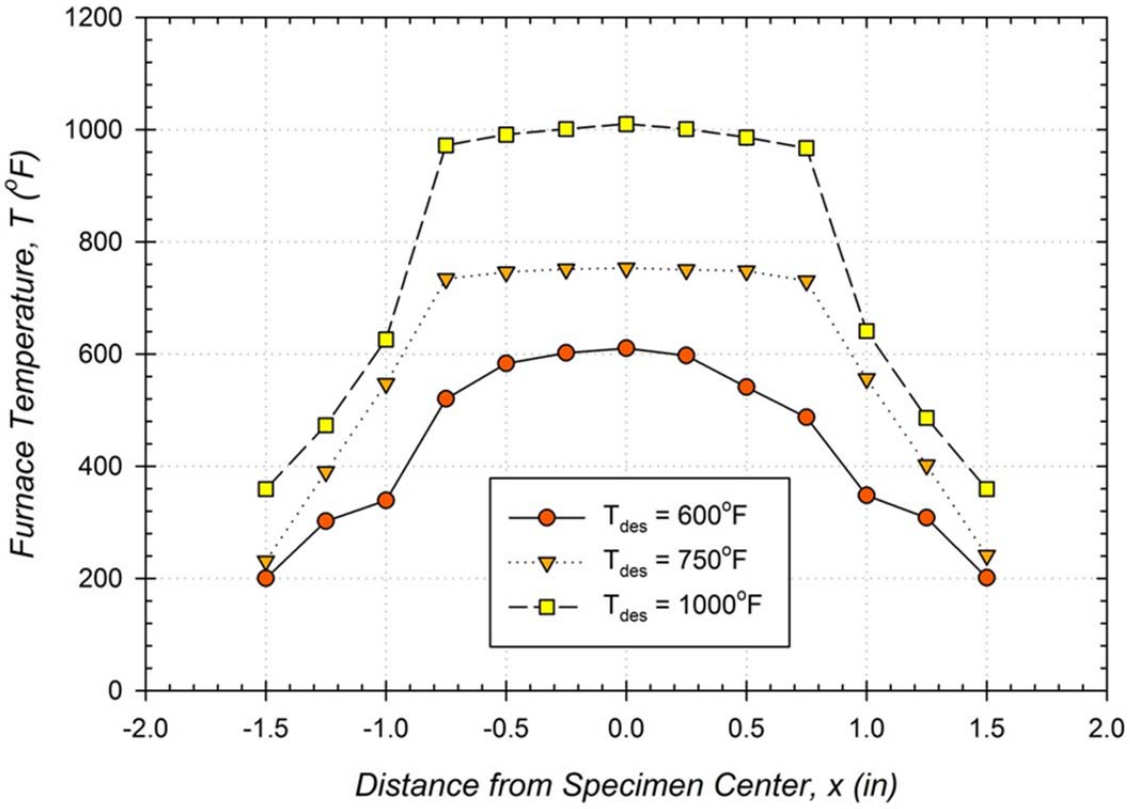

Figure 3.4: Temperature distributions along torsion specimen surface at specified target temperatures.

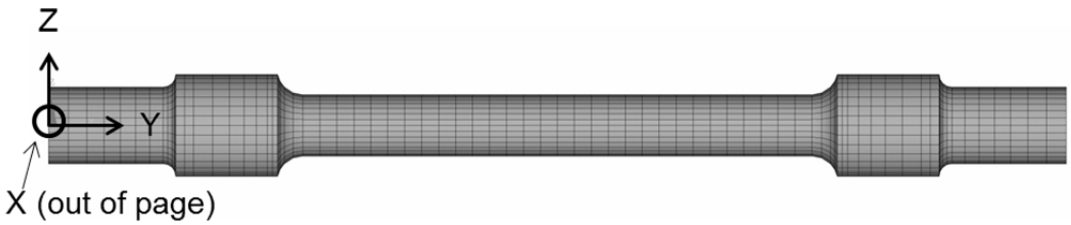

Figure 3.5: Image of ANSYS model geometry and mesh for torsion specimen

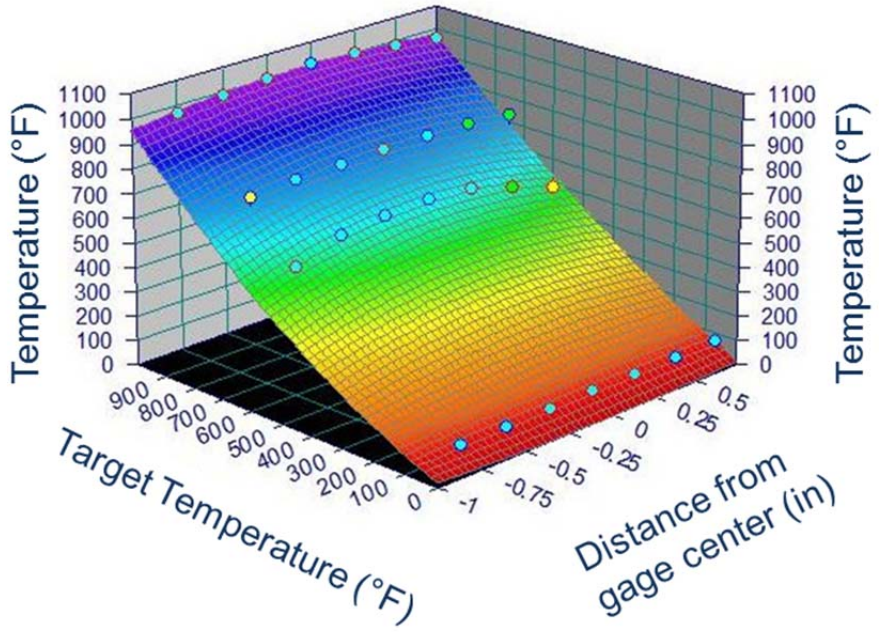

Figure 3.6: Temperature distribution fit.

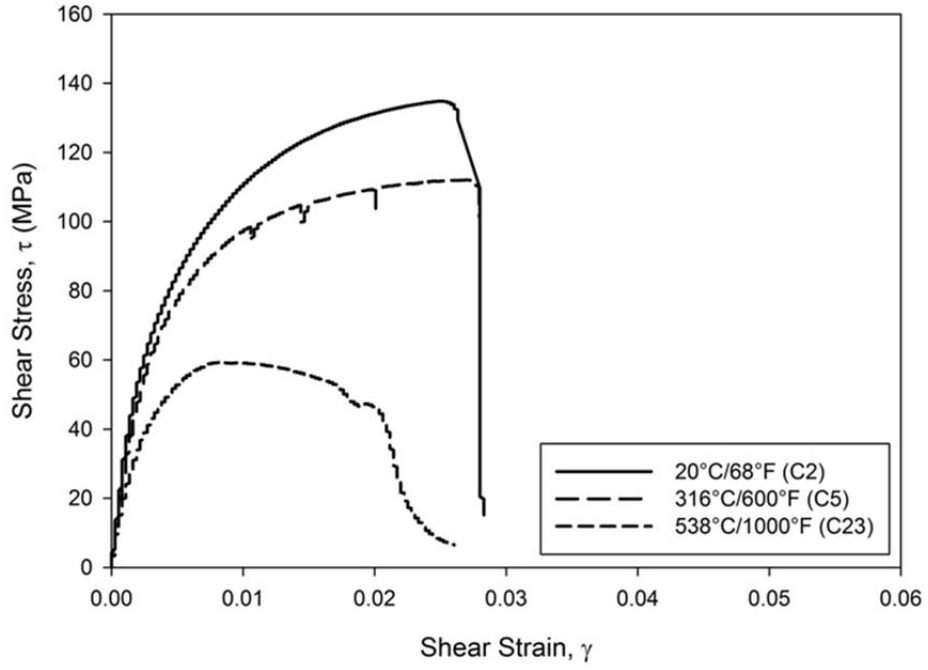

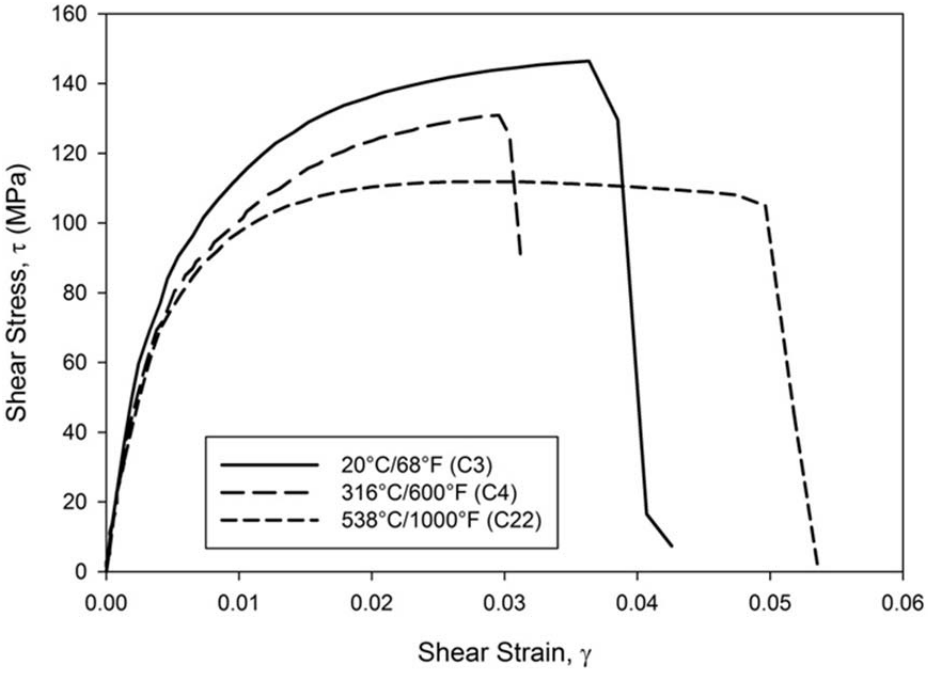

Figure 3.7: Torsion behavior of as-cast A359-SiC_p-30% at various temperatures at a strain rate of (a) 10^{-3} s^{-1}, (b) 10^{1} s^{-1}

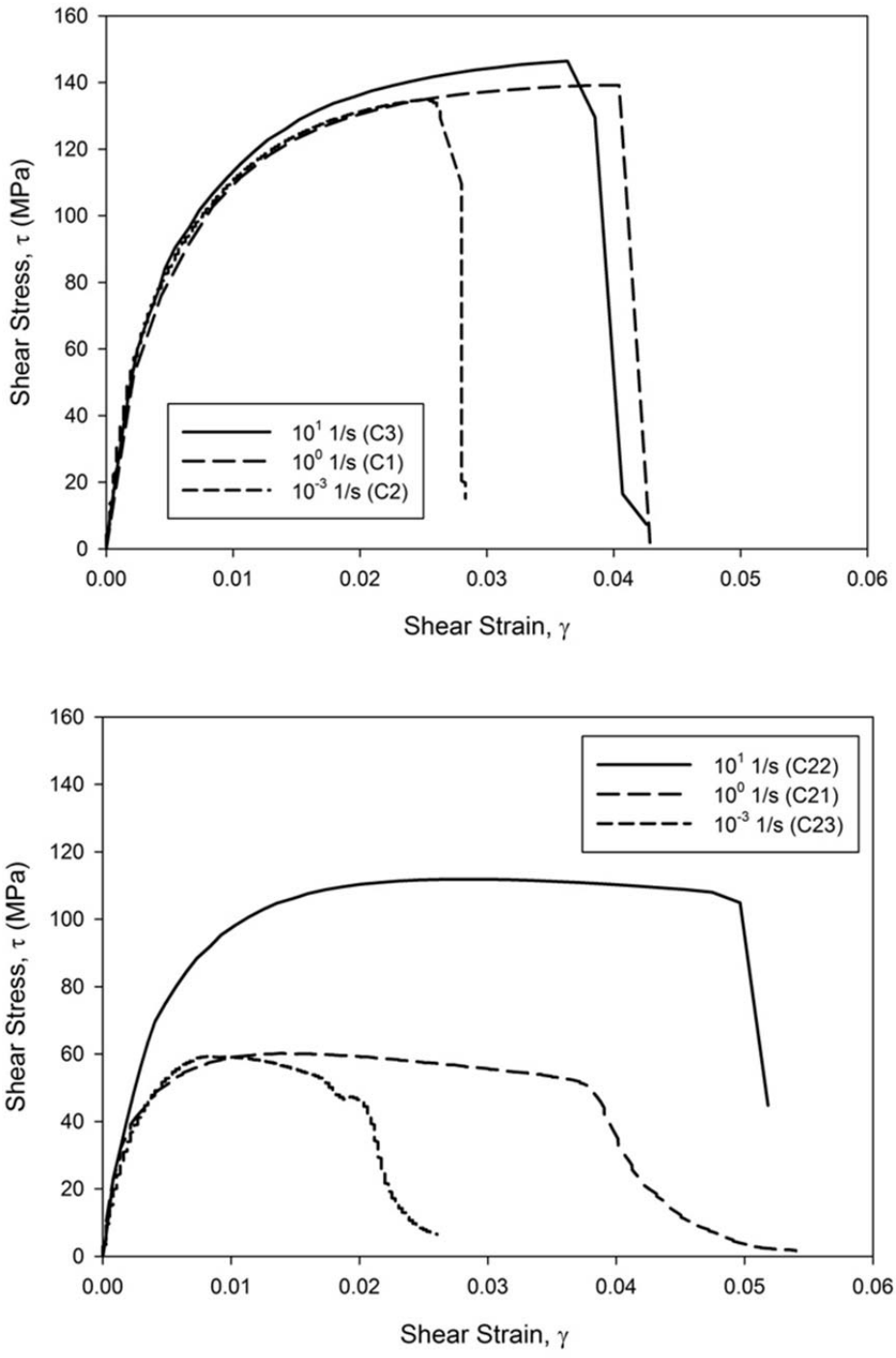

Figure 3.8: Torsion behavior of as-cast A359-SiC_p-30% at various strain rates at temperatures of 20°C (68°F) and 538°C (1000°F)

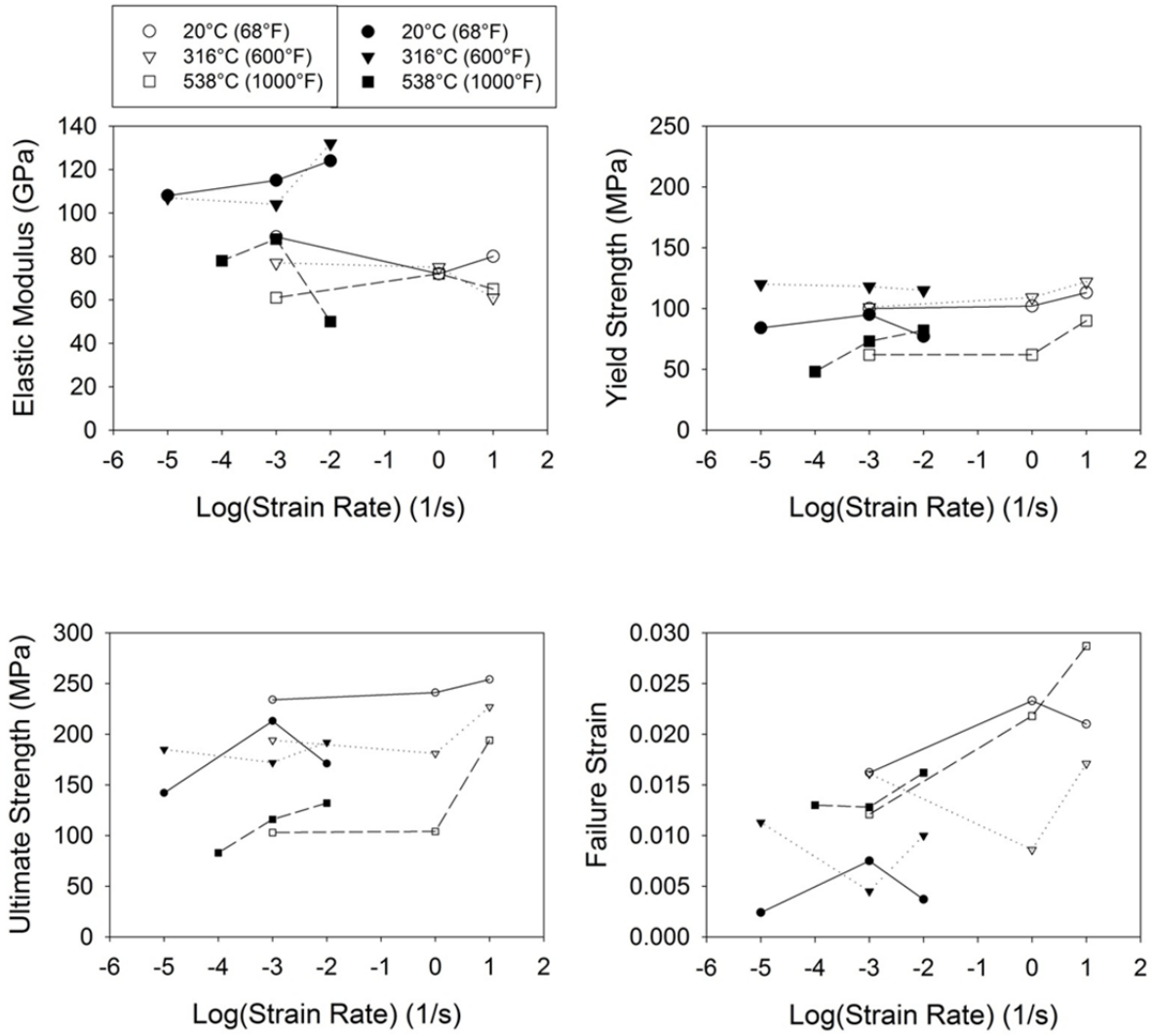

Figure 3.9: Dependence of equivalent material properties on strain rate for tension and torsion; filled symbols represent tension, empty symbols torsion

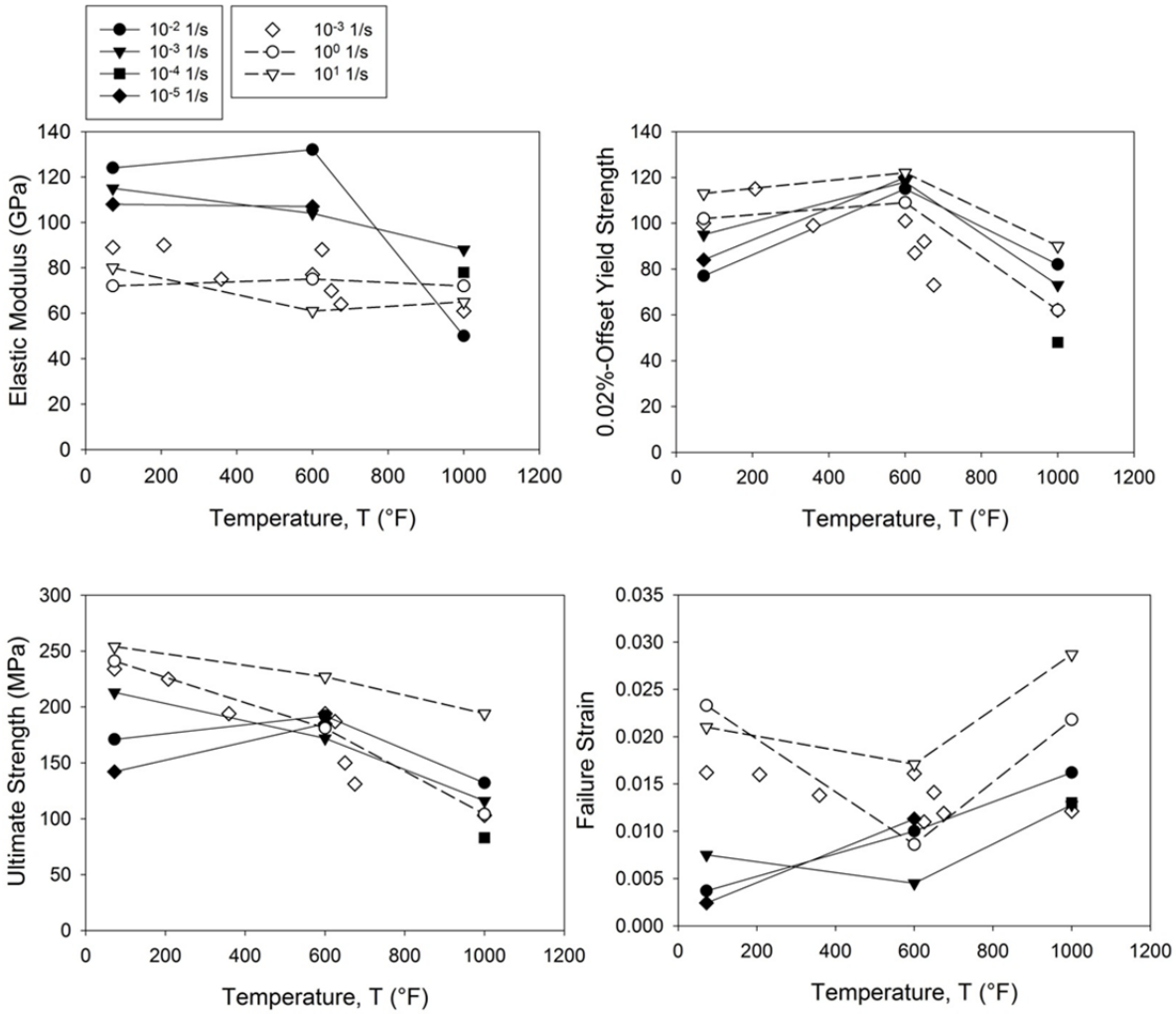

Figure 3.10: Dependence of equivalent material properties on temperature for tension and torsion; filled symbols represent tension, empty symbols torsion

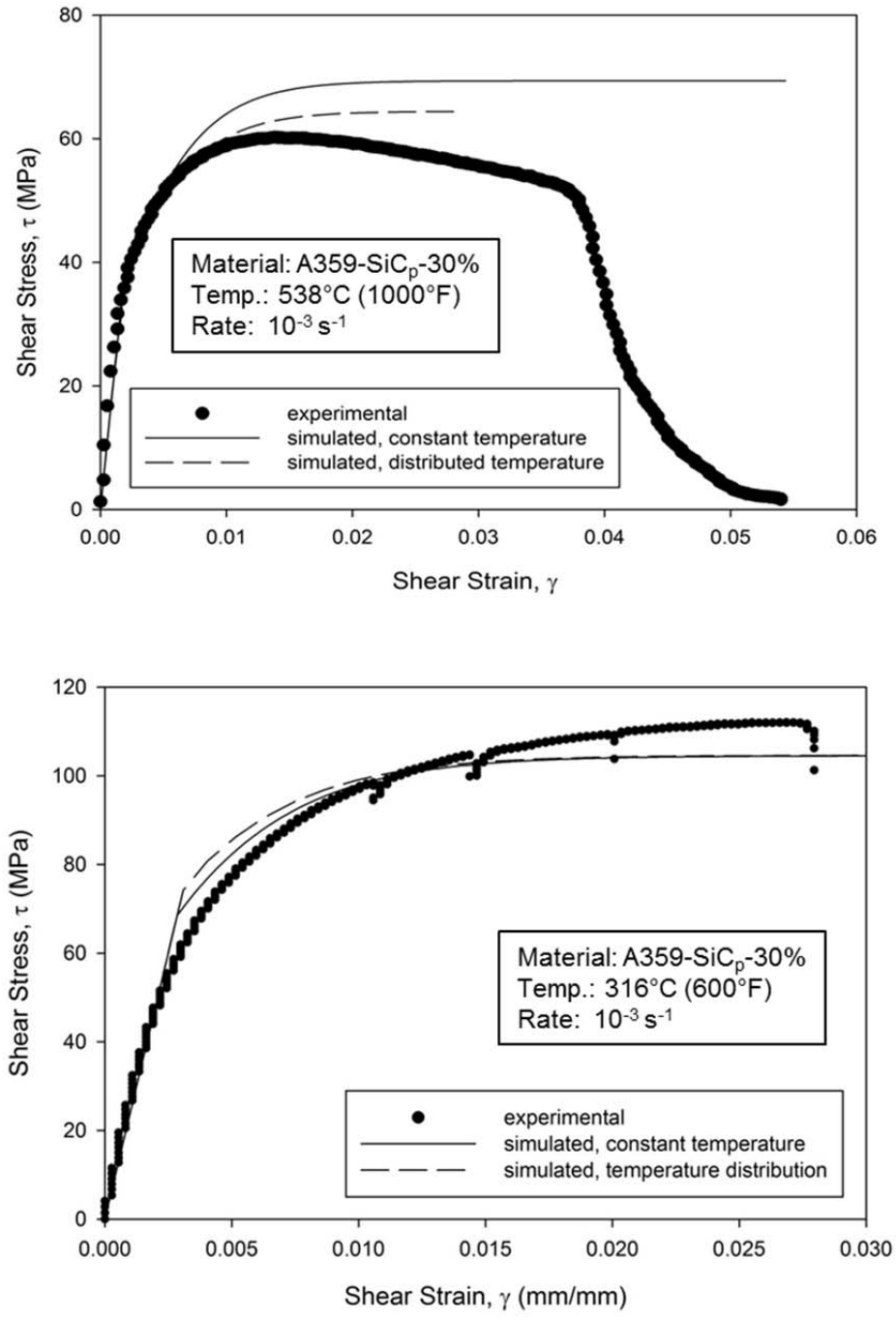

Figure 3.11: Comparison of shear stress-strain curves obtained with and without temperature distribution imposed on specimen.

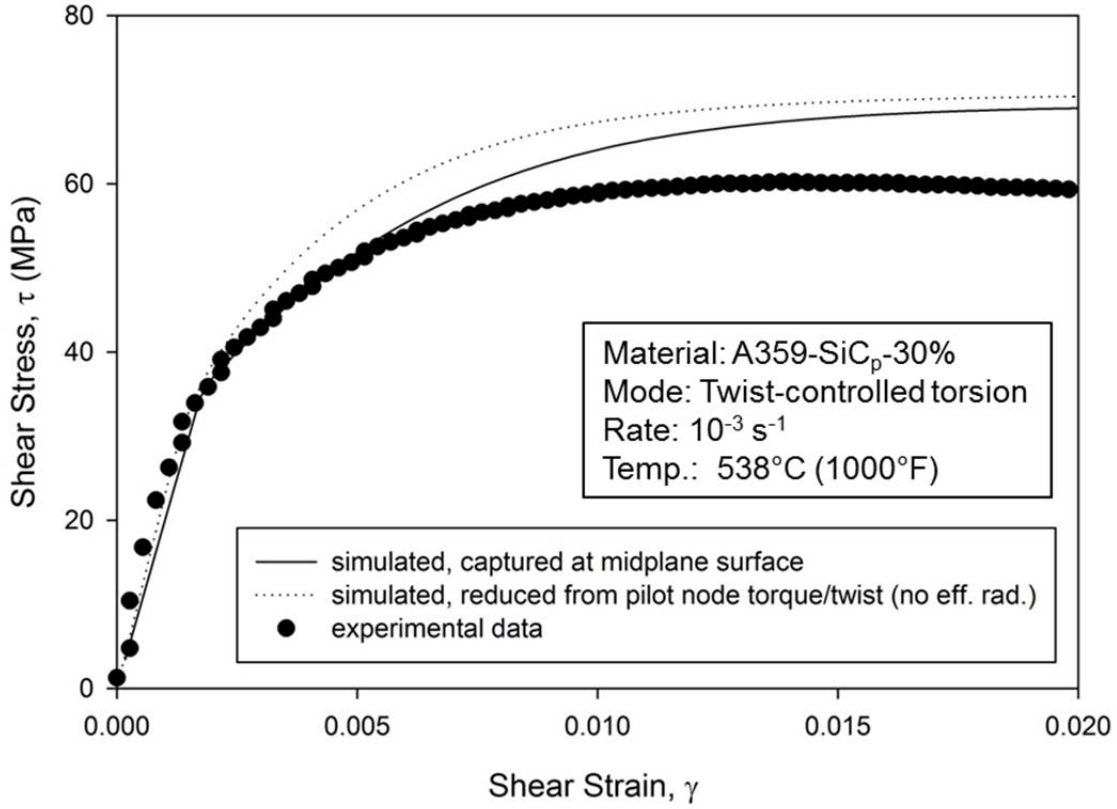

Figure 3.12: Comparison of shear stress-strain curves obtained directly from gage surface and by reduction of pilot-node torque-twist data.

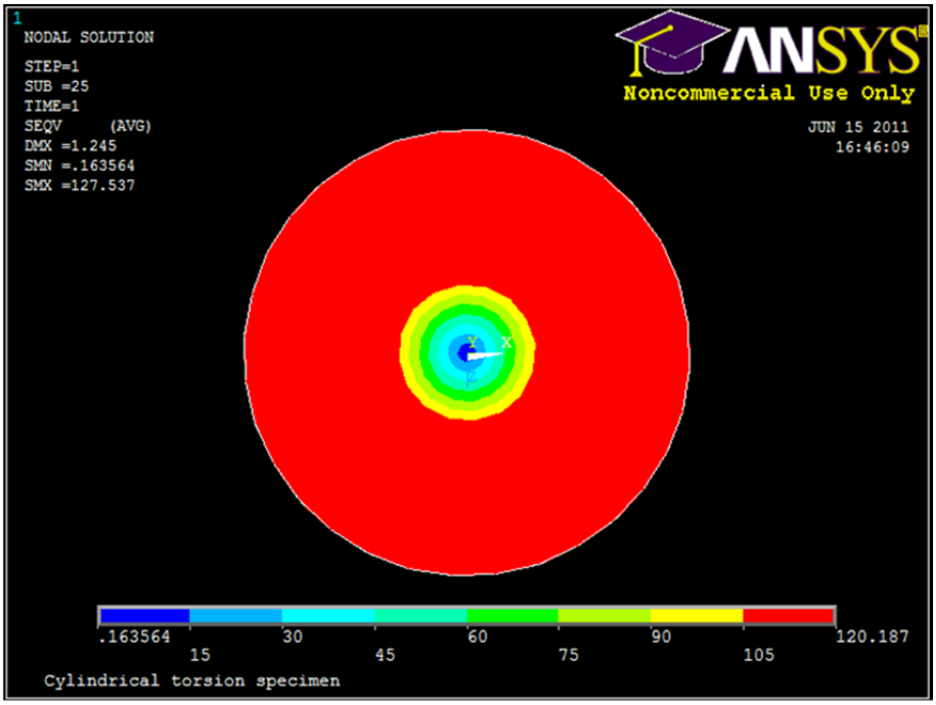

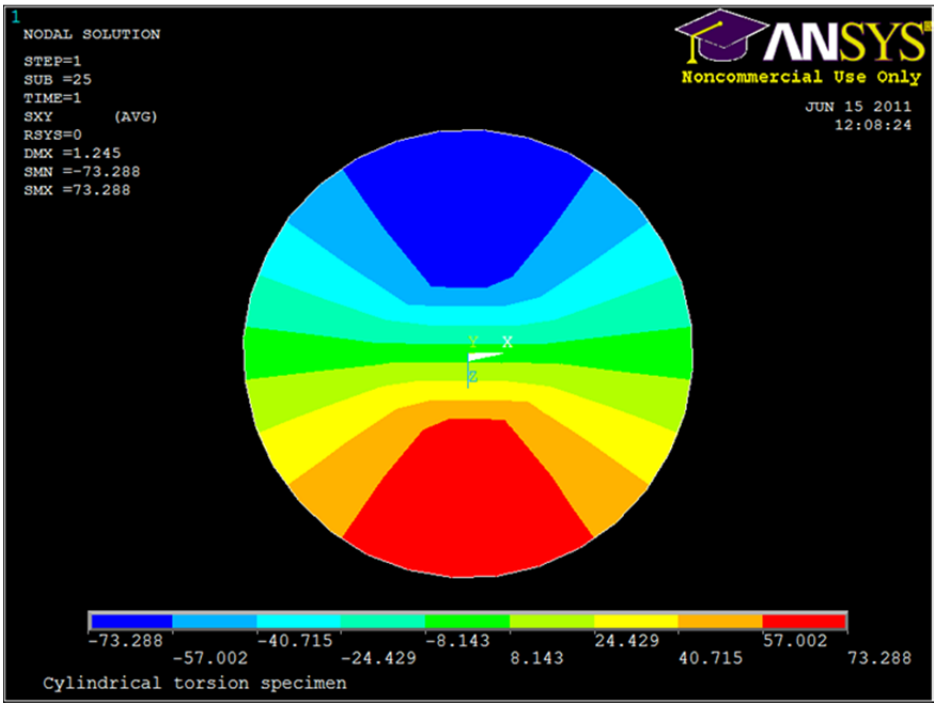

Figure 3.13: (a) von Mises, and (b) x-y shear stress contours at midplane of specimen, 1000°F, equivalent strain rate 10 s^{-1}

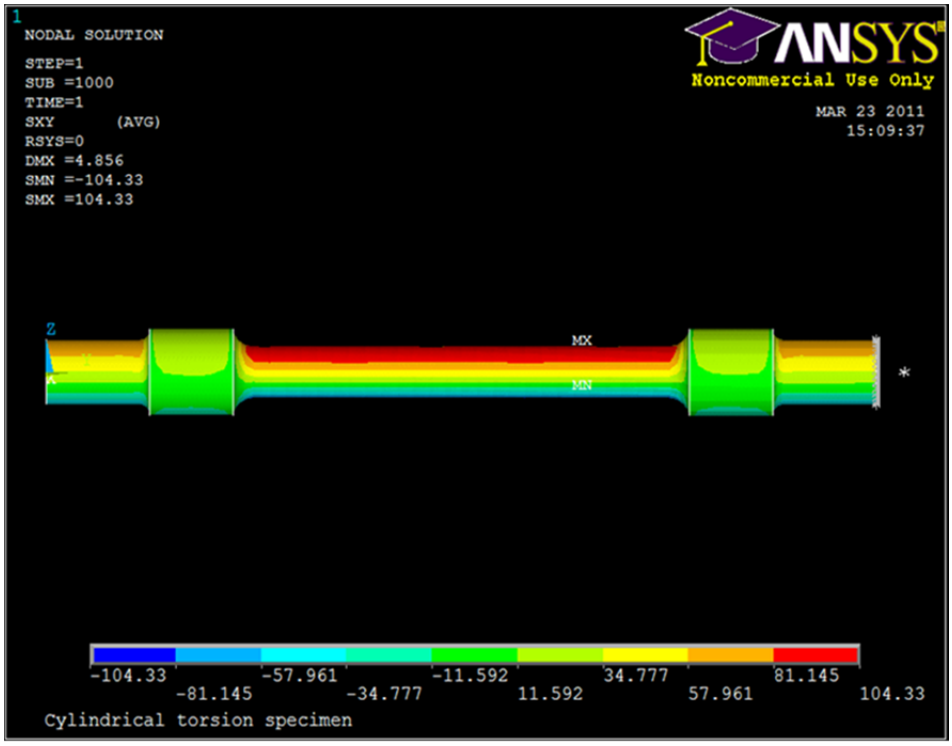

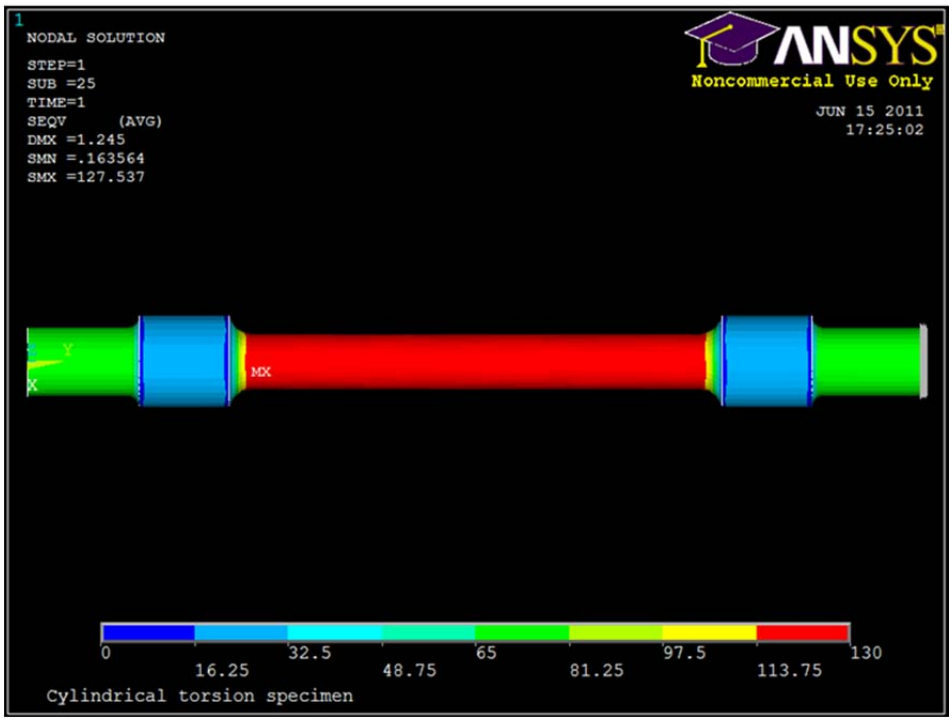

Figure 3.14: (a) von Mises, and (b) x-y shear stress contours at midplane of specimen, 1000°F, equivalent strain rate 10 s^{-1}

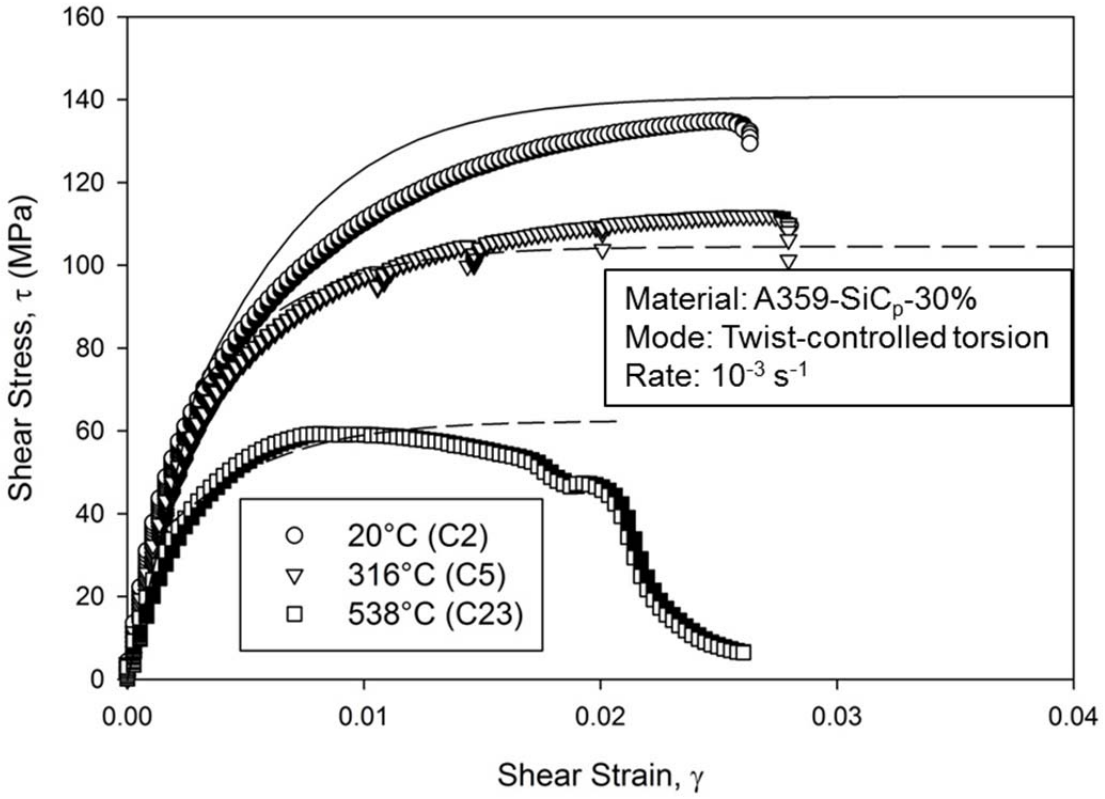

Figure 3.15: Comparison of simulated and experimental tensile response of A359-SiCp-30% at various temperatures at an equivalent strain rate of 10^{-3} s^{-1}.

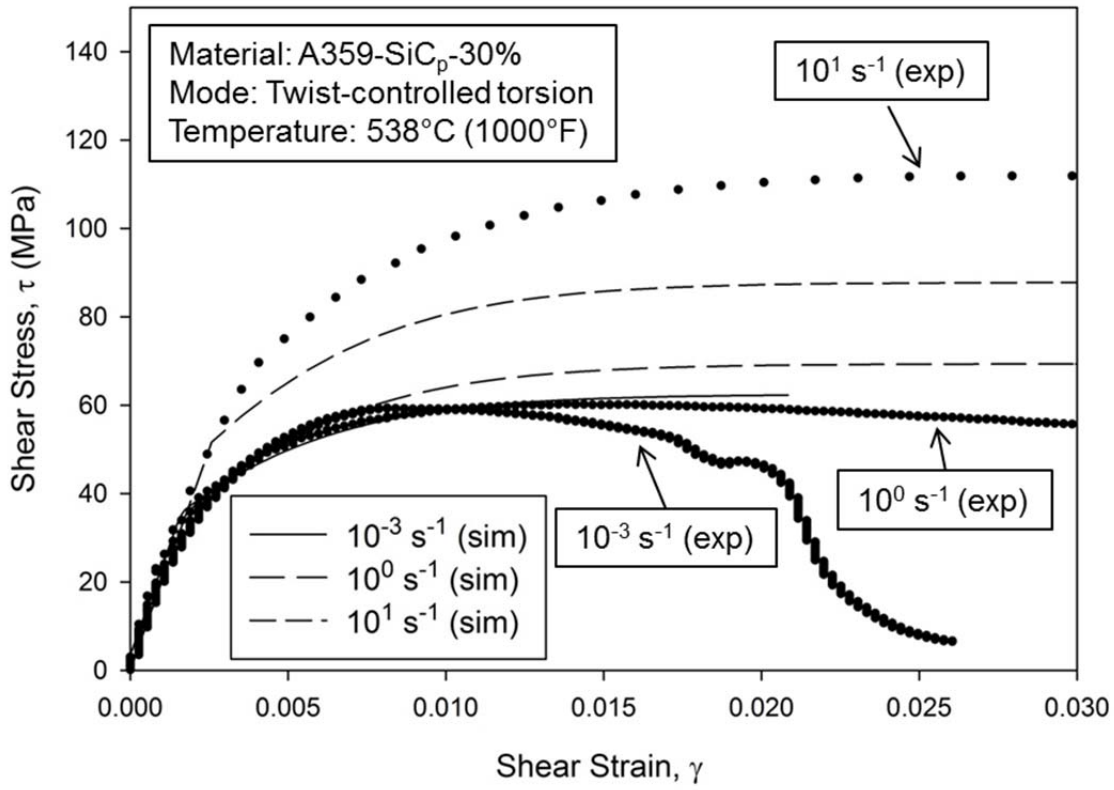

Figure 3.16: Comparison of simulated and experimental shear response of A359-SiC_p-30% at various strain rates at 538°C (1000°F)

CHAPTER 4: AN APPROACH FOR MODELING DUCTILITY OF AS-CAST A359-SiC_p-30% AT ELEVATED TEMPERATURES

An approach for modeling the ductility of as-cast A359-SiC_p-30% at elevated temperatures. By James P. DeMarco, Jr., Nathan Mutter, and Ali P. Gordon.

The contents of this chapter are to be submitted for publication in the Journal of Engineering Materials and Technology

4.1 Abstract

Hot rolling of aluminum metal-matrix composites (MMCs) frequently results in edge cracking, leading to loss of material. Therefore minimization of the amount and extent of edge cracking may lead to an increase in processing efficiency and a concomitant reduction of processing cost. In the following, a model for damage is applied to finite-element simulation of A359-SiC_p-30%. The model extends the Cockcroft-Latham damage model through incorporation of temperature and strain rate dependence of the failure criterion. Experimental data obtained through tension and torsion testing are used to calibrate the temperature and rate dependence of the model. Applications to torsion specimen and hot rolling simulation are discussed.

Keywords: Damage modeling, aluminum metal-matrix composites, hot rolling

4.2 Introduction

Aluminum metal-matrix composites (MMCs) are an attractive alternative to steel for certain applications in which their high strength-to-weight ratio and specific stiffness allow the engineer to meet durability constraints of a component at a fraction of the weight. However, the cost of processing these materials may prevent their use. Typically, cast aluminum MMCs are hot rolled from an initial billet to produce sheets of appropriate thickness for the application of interest.

During the hot rolling process, edge cracking frequently occurs. Cracked edges must be trimmed, which results in a loss of material.

The aluminum metal-matrix composite A359-SiC_p-30% is currently under consideration by MC21, Inc. for use as the base material for tank hatches. However, current equipment in use by MC21 rolls one-inch billets down to thicknesses of 0.25 in or less, and the sheets used for the hatch must be one inch thick or more. It is not cost effective to retool the rolling factory to attempt to minimize rolling through experimentation, even through a fractional factorial approach. Therefore a parametric study of edge cracking through hot rolling simulations is preferred.

Previous studies of A359-SiC_p MMCs include investigation into the material response under tension [1], compression [2], [3] torsion [4], creep [5], [6], [7]and fracture [8], [9], [10]. However, none of these studies address the properties of the as-cast material. Furthermore, after an extensive survey of the literature, the authors have found no previous study on the accumulation of damage in these materials.

In order to simulate hot rolling of as-cast A359-SiC_p-30% at a variety of strain rates and temperatures, a strain-rate- and temperature-dependent constitutive model is necessary. Such a model was introduced for tensile loading of A359-SiC_p-30% in CHAPTER TWO and verified in the simulation of torsion testing in CHAPTER THREE. The model was calibrated through experimental determination of material parameters at key temperatures between room temperature and the melting point of the material and at strain rates representative of those expected in hot rolling.

Efforts to characterize or reduce edge cracking have been addressed in [11], [12], [13], [14], [15], [16]. In [16], 3-D simulation of the hot rolling process incorporated damage modeling, which identified increased values of the damage parameter at the lateral edges of the rolled plate. However, the failure criterion used in the Cockcroft-Latham model was fixed, since the study focused on cold rolling.

In the current work, the constitutive model described in CHAPTER TWO is paired with a modified Cockcroft-Latham damage model in which the failure criterion is defined to be a function of the temperature and strain rate. The model is calibrated by consideration of plastic strain energies obtained from torsion testing. Experimental procedure and microscopic findings are described in Section 2. A derivation of the model is given in Section 3. Results of simulations of hot torsion testing and hot rolling are analyzed in Section 4. Conclusions are discussed in Section 5.

4.3 Microscopy and Testing

The material examined in the current study is as-cast A359-SiC_p-30%. Chemical composition of the aluminum foundry product A359 is given in Table 1 [17]. The alloy is reinforced with 30% volume fraction particulate silicon carbide, which imbues stiffness and some strength to the composite.

Microscopic examination of specimens of the material obtained from MC21 revealed particles whose average size was 17±5 μm, which accords with low-cost measurements taken in [18]. Particle distribution was non-uniform, with areas of high concentration of particles and areas

with low concentration distributed randomly throughout the material. This may be due to incomplete infiltration of reinforcing particles during the casting process or to solidification shrinkage. A micrograph of a section of the material is shown in Fig. Figure 4.1. Four key regions may be observed. The majority of the image consists of solid solution fcc aluminum. The second most prevalent constituent is α-SiC. Regions of eutectic silicon and regions of precipitates and dispersoids rich in magnesium and iron may be observed with less frequency. *However, networks of eutectic silicon may play a crucial role in the failure of the composite, due to the low strength of silicon.*

Tensile data were obtained through monotonic tensile testing of specimens of the as-cast material. Details of the test procedure may be found in CHAPTER TWO. Tests were performed at several different strain rate and temperature combinations. Torsion data were obtained by torsion testing on an MTS Bionix electromechanical load frame. Torque and twist levels were logged by the data acquisition system, and results were reduced to equivalent stress and strain values by means of the effective radius approach put forth by Barraclough et al. [19]. Details of torsion testing and data reduction may be found in CHAPTER THREE. The matrix of tests performed at various conditions is given in Table 2.

Equivalent stress-strain curves obtained through tension and torsion tests were analyzed to identify a set of material properties for each set of test conditions. Ultimate stresses were found by determination of the maximum stress over all data points in a test. Failure strains were identified by a 30% reduction in stress level from the ultimate stress. Toughness values were

obtained by numerical integration of the stress-strain curve up to the failure strain using the trapezoid rule.

In general, the strength of as-cast A359-SiC_p-30% decreases with increasing temperature and increases with increasing rate. The effect of temperature on the mechanical response is readily observed in Fig. Figure 4.2, which shows equivalent stress-strain curves for tests performed at an equivalent strain rate of 10^{-3} s^{-1}. The effect of strain rate is strongest at high temperatures. Strain-rate dependence is demonstrated by the equivalent stress-strain curves shown in Fig. Figure 4.3, which correspond to tests performed at 538°C (1000°F).

The failure strain of the composite is slightly more complicated. For slightly elevated temperatures, failure strain appears to decrease somewhat with increasing temperature. However, above 316°C (600°F), the failure strain increases sharply with temperature. Failure strain generally increases with increasing strain rate, although there is significant scatter in the data. These trends may be observed in Fig. Figure 4.4, in which plots of the failure strain and the ultimate strength versus rate and temperature are shown.

The toughness of the material was generally found to increase with increasing strain rate, while toughness reached a minimum at or near 316°C (600°F) for several different strain rates. These trends may be observed in Fig. Figure 4.5. While the toughness of a material is dictated by the entirety of the stress-strain curve used for its calculation, it is strongly correlated to ultimate strength and failure strain for most materials. Thus it is possible to observe a high toughness value at a particular combination of strain rate and temperature and determine through consideration of the failure strain and ultimate strength that, for example, the high stress levels

reached during the test were more responsible for the resulting toughness value than the amount of strain. In general, however, the trends in failure strain and ultimate strength are too complicated to make direct predictions of trends in the toughness.

4.4 Numerical Approach

The damage model is based on that of Cockcroft and Latham [40]. In the Cockcroft-Latham model, damage is considered to occur whenever the principle stress is tensile and plastic strain is occurring. The damage parameter, D, is defined by

$$D = \int \max(\sigma_1, 0)\, d\bar{\epsilon}_p,$$

where σ_1 represents positive principal stress and the overbar indicates the von Mises equivalent, so that $\bar{\epsilon}_p$ represents the von Mises equivalent plastic strain. The integral is taken over the plastic strain range. A second parameter, C, represents the value D obtains when the material reaches failure, which is assumed to be the same regardless of the mode of loading. That is,

$$C = \int_0^{\bar{\epsilon}_p^*} \max(\sigma_1, 0)\, d\bar{\epsilon}_p\,,$$

where $\bar{\epsilon}_p^*$ is the equivalent plastic strain at failure. Hereafter, C is referred to as the absolute damage, and D is referred to as the damage limit.

In the case of uniaxial tension, the principal stress is equal to the tensile stress, and the equivalent plastic strain is the total tensile strain minus the elastic tensile strain. Therefore C can be calculated by integration of the stress-strain diagram for a tensile test from the yield point to the point of failure.

To determine the damage limit from data obtained through torsion testing, the torque and twist read by the tester may be reduced to equivalent stress and strain through various approaches. The approach taken here is to determine shear stress and strain through application of the effective radius method introduced by Barraclough et al. [19], which is then converted to equivalent stress and strain. The equivalent stress-strain diagram is used to determine the value of C in the same manner as that applied for uniaxial tension.

Once values for the damage limit have been obtained at various temperatures and strain rates, trends in the data may be observed. Given sufficient consistency in the temperature and rate dependence, a function may be fit to the data, so that

$$C = C(T, \dot{\epsilon}_p)$$

where T is the temperature for the test and $\dot{\epsilon}_p$ is an approximation of the average equivalent plastic strain rate. It is then possible to specify different criteria for the limit to workability of the specimen depending on the temperatures and strain rates imposed on the material during simulation.

Toughness values obtained in the previous section were found to be close approximations of the damage limit, with differences on the order of 3% or less. Therefore, on the basis of the trends observed in the toughness, a mixed polynomial in T and $\dot{\epsilon}_p$ was chosen as the model for temperature and strain rate dependence. The function for the damage limit is given by

$$C\left(T, \dot{\epsilon}_p\right) = a_0 + a_1 T + a_2 \dot{\epsilon}_p + a_3 T^2 + a_4 T \dot{\epsilon}_p + a_5 \dot{\epsilon}_p^2 + a_6 T^2 \dot{\epsilon}_p + a_7 T \dot{\epsilon}_p^2$$

where $a_0, \ldots, a_7$ are parameters which are identified by least-squares regression over the temperature and strain rate dependence data. The form of this function allows up to quadratic

dependence of the damage limit in both temperature and strain rate. Mixed-order terms allow the dependence on temperature to vary with strain rate and vice versa. As a function of either strain rate or temperature alone, the function may obtain at most one maximum or minimum over the domain of interest.

Least-squares regression was performed by application of a user-defined function in TableCurve3D. Initially, all data points were included in the toughness data used in the fit. However, the initial fit showed the presence of one data point over two standard deviations away from the fitting surface and two data points at least one standard deviation from the fitting surface. These three points, along with another borderline case, were identified as outliers and rejected as anomalous. The remaining data points were used for a second regression for which the resulting coefficient of determination was 79.96% and the degree of freedom-adjusted coefficient of determination was 63.92%. The fitted surface and data points included in the fit are shown in Fig. Figure 4.6. Experimental and predicted values as well as relative errors for all temperatures and rates tested are given in Table 3.

To allow comparison of damage levels at different thermal and rate conditions, a relative damage parameter D_R is introduced, where

$$D_R = \frac{D}{0.75C}.$$

The scale factor of 0.75 is included to account for the wide variation in the value of the damage limit from the predicted value over repeated experiments at the same conditions. The result is that all but four of the tests included in the regression reach failure for D_R in the range 0.5 to 1.

The trends predicted by the regressed damage model are in line with observations of the trends in toughness noted in the previous section. The damage limit predicted by the model generally increases with rate. Dependence on strain rate is weaker at temperatures near 316°C (600°F), which results in a damage limit maximum in this temperature range at the lowest rate and a damage limit minimum in this range at the highest rate.

4.5 Results

The damage model was implemented as part of a user-programmable feature within the ANSYS finite element software suite. The damage limit function was written into input decks used to define the parameters of the finite element solution. Two test problems were considered. The first involved 3D simulation of a torsion test specimen subjected to different test temperatures and twist rates. As the torsion of cylindrical shafts is a well-understood problem in the mechanics of materials, this was considered a good test case to confirm proper functioning of the damage model. The second test problem considered was 3D simulation of hot rolling. This case was chosen to determine whether the model could predict the increased damage expected to occur at the edges of a rolled sheet in correlation with the well-known phenomenon of edge cracking.

The model for the torsion test specimen was based on specified dimensions of the actual test specimens machined for use in the torsion testing of A359-SiC_p-30% described in (ref). A radial cross section of the specimen was drawn and revolved to produce a radially symmetric solid model, and the geometry was meshed using 20-node SOLID186 brick elements. Twist was imposed by utilization of a pilot node at one end of the specimen, and a pressure condition was

imposed in the grip section at the free end to resist radial expansion. A uniform temperature was imposed on the specimen. The mesh and boundary conditions are illustrated in Fig. **Error! Reference source not found.**.

Contours of the relative damage were determined for a simulation conducted at a temperature of 538°C (1000°F) and a strain rate of 10^1 s^{-1} to verify that simulated behavior matched with expectations based on mechanics of materials and experimental observation. The test was run until the damage limit was reached at a node on the surface of the specimen at its longitudinal midplane. Surface contours of D_R for this case are shown in Fig. Figure 4.8(a). It is observed that damage levels reach maximum only in the gage section. This conforms with conventional wisdom regarding torsion testing using properly designed specimens. All A359-SiC_p-30% specimens tested for the current study failed in the gage section, although the exact lengthwise position varied. This variation is expected due to the microscale variation in the distribution of particles and grains which are responsible for the instabilities that lead to failure. Since no microscale model or artificial asymmetry was introduced to the simulated specimen, it is expected that the surface distribution of damage does not show a well-defined maximum at a particular location in the gage section. Contours plotted in cross section of the specimen taken at its midplane show that the relative damage is axisymmetric and decreases from surface to center; see Fig. Figure 4.8(b). Since both stress and strain should decrease from their maxima to zero from the surface to the center, this pattern in the relative damage is as expected.

Histories for the damage, D, and relative damage, D_R, were obtained for simulations conducted at several different temperatures and twist rates. The simulations were conducted to rotations

exceeding those observed in actual testing so as to ensure that damage levels in excess of those necessary for failure were reached. In order to allow comparison of damage histories for simulations occurring at multiple rates, a relative time scale was adopted in which one unit of time is equivalent to one radian of axial rotation. Using this approach, the absolute damage histories are difficult to compare due to differences in damage limit depending on the conditions of the test being simulated, as shown in Fig. Figure 4.9(a). However, relative damage histories shown in Fig. Figure 4.9(b) allow for easier comparison of damage evolution, since at a given value of the relative damage, the same proportion of the damage limit has been reached, regardless of test conditions simulated. The use of the relative time scale also provides the ability to compare the workability under various test conditions, since the amount of rotation permitted for a given simulation while maintaining damage below a specified level is easily checked. Benefits of the relative damage approach also include the ability to perform parametric studies of processes in which workability is an issue and the option to apply a summation approach to damage modeling of a material subjected to varying temperature and strain rate conditions during a single process.

Hot rolling simulation was performed via the LS-DYNA explicit dynamics package within ANSYS. The setup for the simulation is illustrated in Fig. Figure 4.10. The roll speed was set to approximate a strain rate of 10^1 s^{-1} by assuming a total strain of $\ln(\frac{t_i}{t_f})$, where t_i and t_f are the initial and final half-thicknesses of the plate, and that the strain occurs over a time approximately equal to the contact time. For the purposes of this report, a simplified constitutive model provided within LS-DYNA was used to approximate the stress response of the A359-SiC_p-30%

material at 538°C (1000°F) and a strain rate of 10^1 s^{-1}. The experimentally-derived stress-strain curve and the bilinear model used to approximate it are shown in Fig. Figure 4.11. Symmetry boundary conditions were used to reduce the model to quarter-scale for computational efficiency. The roller was defined to be a rigid body, and a one-node element was used to push the sheet into the roll mill. The push node imparted a linear speed one-half that of the roller surface so that the sheet would separate from the push node upon entry into the mill. Friction between roller and sheet was defined by the dry friction model with static and dynamic friction both set to 0.9. The thickness reduction for the simulation was set to 50%.

Histories of the plastic strain and the principal stress were recorded for twenty points evenly distributed in a cross section of the sheet normal to the roll direction. The histories were used to compute damage at these points. Results are given in Fig Figure 4.12. These results show that the greatest amount of damage accrues at the lateral edges of the sheet, with no damage occurring toward the center and away from the specimen surface. Modest levels of the damage parameter were observed near the specimen surface but away from the lateral edges. The lack of damage in the sheet center may be attributed to a compressive principal stress at these nodes, while dominant plane stress conditions at free surfaces allow tensile stress to occur at these locations. These results conform with observations of hot rolling of A359-SiC_p-30%, for which edge cracking has been noted.

4.6 Conclusions

Experimental data obtained for as-cast A359-SiC_p-30% were used to identify temperature and strain rate dependence of material properties relevant to workability. The Cockcroft-Latham

damage model was modified to include temperature and rate dependence of the failure criterion. Experimental results for toughness were used to calibrate the temperature and rate dependence of the damage limit.

The resulting model was implemented via ANSYS finite element software. Simulations of torsion testing were used to verify the model. Damage histories showed the accumulation of damage over the course of the simulation, and contour plots of the surface and a cross section of the gage portion of the model showed damage maxima in the expected locations. The model was applied to the simulation of hot rolling, and it was found that the model predicted damage maxima in the regions where damage has been noted to occur most frequently during the rolling process.

4.7 Acknowledgments

4.8 References

[1] Y. Li, K. T. Ramesh, and E. S. C. Chin, "Plastic Deformation and Failure in A359 Aluminum and an A359-SiCp MMC under Quasistatic and High-strain-rate Tension," *Journal of Composite Material*, vol. 41, pp. 27-40, 2007.

[2] Y. Li, K. T. Ramesh, and E. S. C. Chin, "The compressive viscoplastic response of an A359/SiCp metal-matrix composite and of the A359 aluminum alloy matrix," *International Journal of Solids and Structures*, vol. 37, pp. 7547-7562, 2000.

[3] Y. Li, K. T. Ramesh, and E. S. C. Chin, "Viscoplastic Deformations and Compressive Damage in an A359/SiCp Metal-Matrix Composite," *Acta mater.*, vol. 48, pp. 1563-1573,

2000.

[4] Y. Li, K. T. Ramesh, and E. S. C. Chin, "The mechanical response of an A359/SiCp MMC and the A359 aluminum matrix to dynamic shearing deformations," *Materials Science and Engineering A*, vol. 382, pp. 162-170, 2004.

[5] O. A. Hamed, M. A. Shady, and A. R. El-Desouky, "Creep behavior of a cast 359/SiC/10p aluminum composite," *Materials & Design*, vol. 22, pp. 473-479, 2001.

[6] N. P. Hung, C. S. Lim, Y. K. Ho, Y. C. Tan, and W. G. Tan, "Cumulative creep and hot isostatic pressing of particle-reinforced metal matrix composites," *Journal of Materials Processing Technology*, vol. 101, pp. 104-109, 2000.

[7] A. Madgwick, C. Ungpinitpong, T. Mori, and P. J. Withers, "Observation and quantitative analysis of damage caused by creep in an Al A359/SiCp composite," *Materials Science and Engineering A*, vol. 342, pp. 201-206, 2003.

[8] D. P. Myriounis, S. T. Hasan, and T. E. Matikas, "Microdeformation behaviour of Al-SiC metal matrix composites," *Composite Interfaces*, vol. 15, no. 5, pp. 495-514, 2008.

[9] D. P. Myriounis, S. T. Hasan, N. M. Barkoula, A. Paipetis, and T. E. Matikas, "Effects of Heat Treatment on Microstructure and the Fracture Toughness of SiCp/Al Alloy Metal Matrix Composites," *Journal of advanced materials*, vol. 41, no. 3, pp. 18-27, 2009.

[10] R. Rodríguez-Castro, R. C. Wetherhold, and M. H. Kelestemur, "Microstructure and mechanical behavior of functionally graded Al A359/SiCp composite," *Materials Science and Engineering A*, vol. 323, pp. 445-456, 2002.

[11] L. S. Bayoumi, "Edge Stresses in Wide Strip Hot Rolling," *International Journal of Mechanical Sciences*, vol. 39, no. 4, pp. 397-408, 1997.

[12] F. Czerwinski et al., "The edge-cracking of AISI 304 stainless steel during hot-rolling," *Journal of Materials Science*, vol. 34, pp. 4727-4735, 1999.

[13] M. H. Han et al., "Analysis and prevention of edge cracking phenomenon during hot rolling of non-oriented electrical steel sheets," *Materials Science and Engineering A*, vol. 264, pp. 47-50, 1999.

[14] H. Riedel, F. Andrieux, T. Walde, and K. Karhausen, "The Formation of Edge Cracks during Rolling of Metal Sheet," *Steel Research International*, vol. 78, no. 10, pp. 818-824, 2007.

[15] J. Uan and H. Chen, "Uniform Equiaxed Grain Structure throughout Thickness of a Hot-Rolled 5083 Al-Mg-Mn Alloy Thick Plate after a Tempering Treatment at 350°C," *Materials Transactions*, vol. 48, no. 2, pp. 178-183, 2007.

[16] S. Ghosh, M. Li, and D. Gardiner, "A Computational and Experimental Study of Cold Rolling of Aluminum Alloys with Edge Cracking," *Transactions of the ASME*, vol. 126, pp. 74-82, February 2004.

[17] C. Triveño Rios, C. Bolfarini, W. J. Botta F., and C. S. Kiminami, "Rapidly Solidified Al-Si-Mg Alloy," *Journal of Metastable and Nanocrystalline Materials*, pp. 594-598, 2004.

[18] W. H. Hunt, D. M. Schuster, M. D. Skibo, M. T. Smith, and D. R. Herling, "Lower Cost Cast Aluminum MMC Process and Products," in *State of the art in cast metal matrix*

composites in the next millenium; proceedings of a symposium, 2000, pp. 265-272.

[19] D. R. Barraclough, H. J. Whittaker, K. D. Nair, and C. M. Sellars, "Effect of Specimen Geometry on Hot Torsion Test Results for Solid and Tubular Specimens," *Journal of Testing and Evaluation*, vol. 1, no. 3, pp. 220-226, May 1973.

4.9 Tables

Table 4.1: Chemical composition of A359 matrix

Si	Fe	Cu	Mn	Mg	Zn	Sn	(Trace)	Al
9.45	0.11	<0.006	<0.05	0.67	<0.05	0.02	0.2	Bal.

Table 4.2: Test conditions. A label of "C" indicates torsion, and "TE" indicates tension

Specimen ID	Temperature (°C (°F))	Log(Strain Rate)	Toughness (MPa)	Predicted Damage Limit (MPa)	Relative Error (%)
C2	20 (68)	-3	4.7295	1.84	156.53
C1	20 (68)	0	3.0503	3.59	-14.96
C3	20 (68)	1	4.3825	3.99	9.73
C19	97 (207)	-3	2.9638	1.87	58.57
C20	182 (359)	-3	2.2252	1.84	20.99
C5	316 (600)	-3	3.0692	1.67	83.99
C18	316 (600)	0	1.0918	1.90	-42.43
C4	316 (600)	1	2.6097	2.23	17.06
C27	329 (625)	-3	1.6378	1.64	-0.24
C25	343 (650)	-3	1.8654	1.61	15.60
C24	357 (675)	-3	1.3065	1.58	-17.52
C23	538 (1000)	-3	1.0467	1.05	-0.27
C21	538 (1000)	0	2.0512	3.08	-33.50
C22	538 (1000)	1	5.0075	4.34	15.29
TE11	20 (68)	-5	0.2185	0.25	-11.32
TE02	20 (68)	-3	1.2065	1.84	-34.56
TE10	20 (68)	-2	0.4332	2.51	-82.75
TE04	316 (600)	-5	1.7068	2.16	-20.91
TE03	316 (600)	-3	0.5577	1.67	-66.57
TE05	316 (600)	-2	1.606	1.62	-0.61
TE08	538 (1000)	-4	0.9153	0.95	-3.86
TE07	538 (1000)	-3	1.2991	1.05	23.78
TE06	538 (1000)	-2	1.8439	1.44	28.28

4.10 Figures

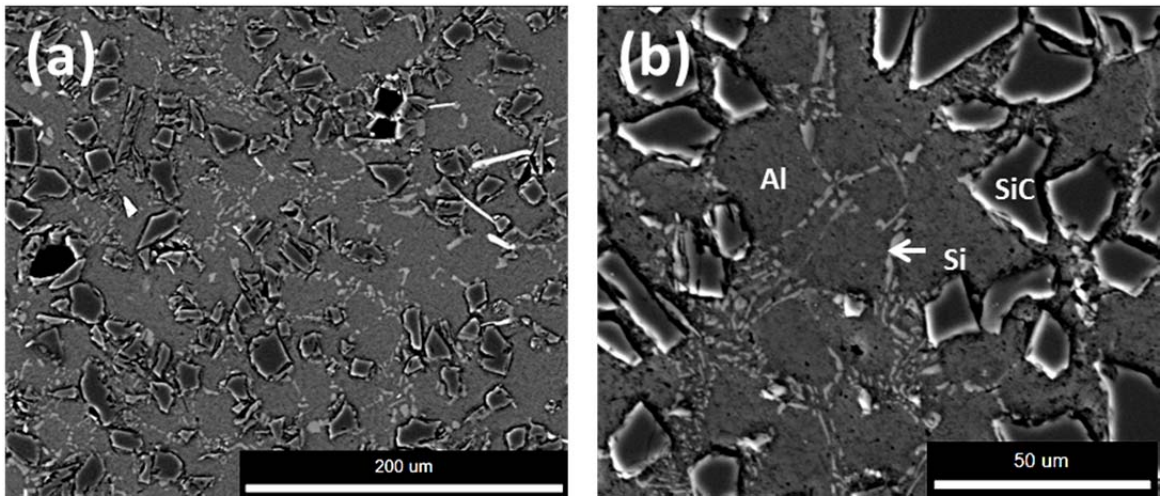

Figure 4.1: Microstructure of A359-SiC_p-30%

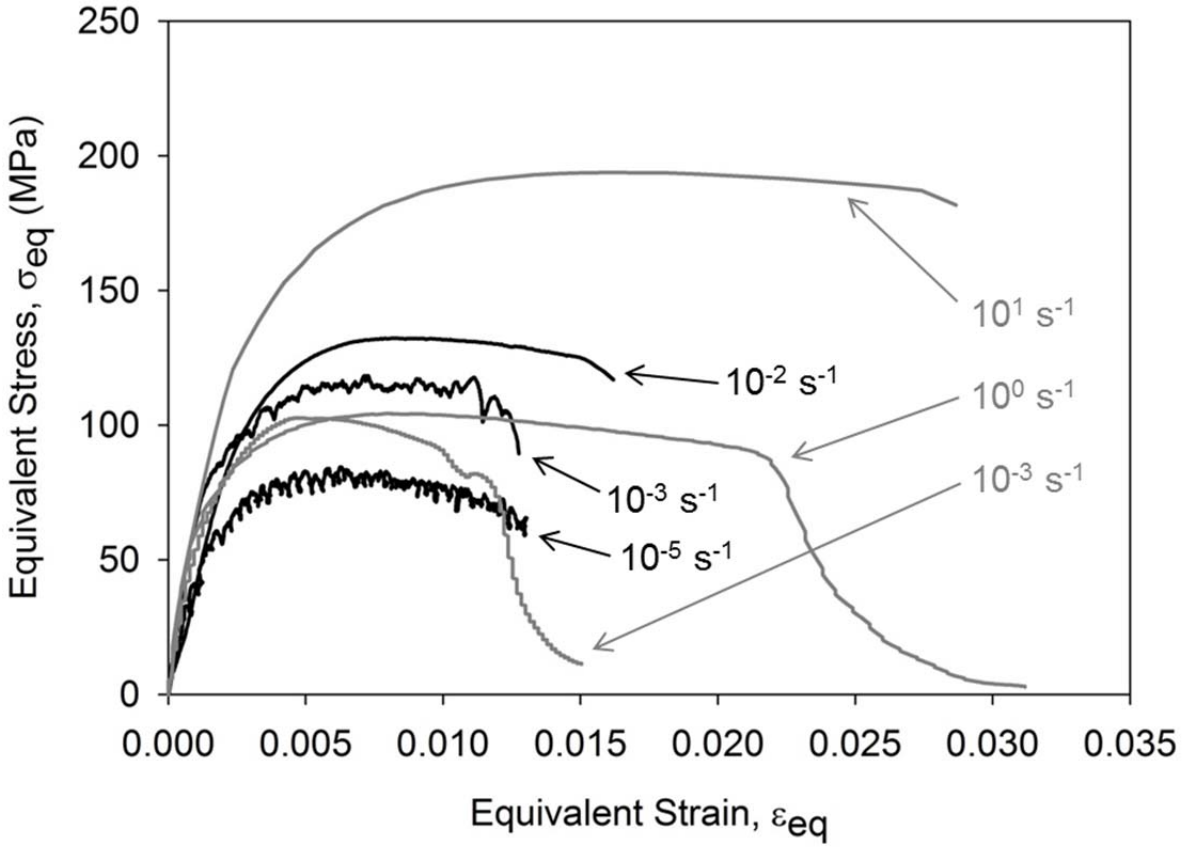

Figure 4.2: Stress-strain profiles at 538°C (1000°F). Black curves represent tension; gray curves represent torsion.

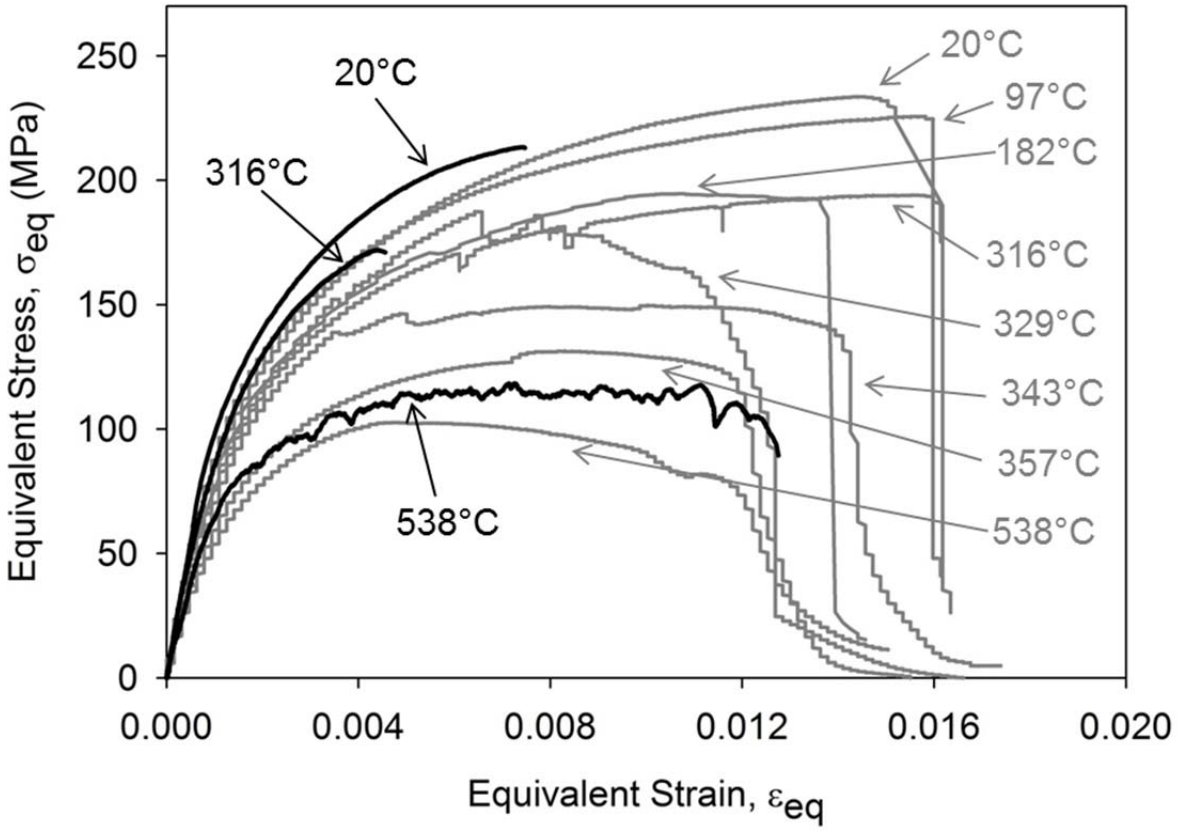

Figure 4.3: Stress-strain profiles at an equivalent strain rate of 10^{-3} s^{-1}. Black curves represent tension; gray curves represent torsion.

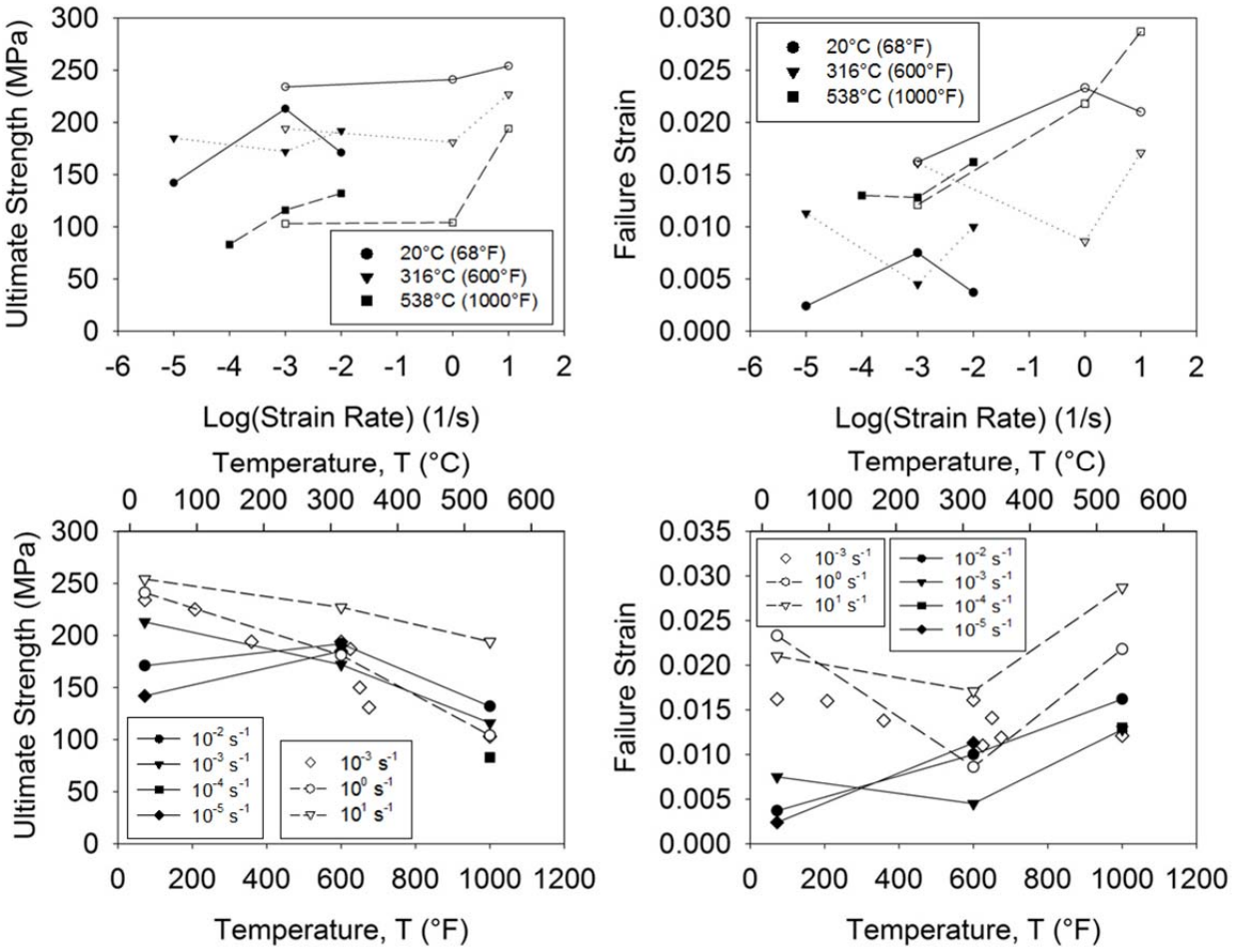

Figure 4.4: Ultimate strengths and failure strains versus (a) temperature, (b) strain rate.

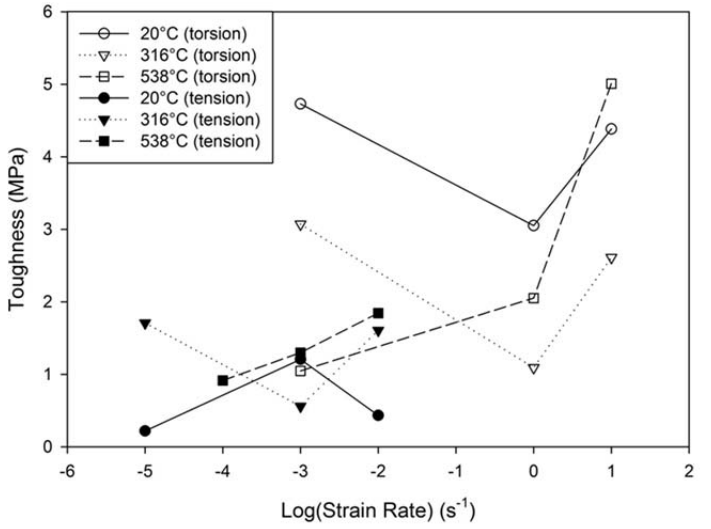

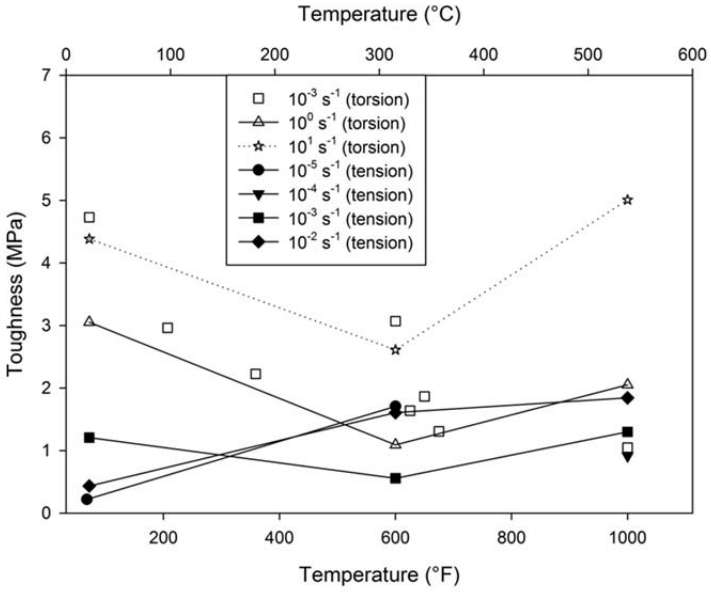

Figure 4.5: Toughness versus (a) strain rate, (b) temperature.

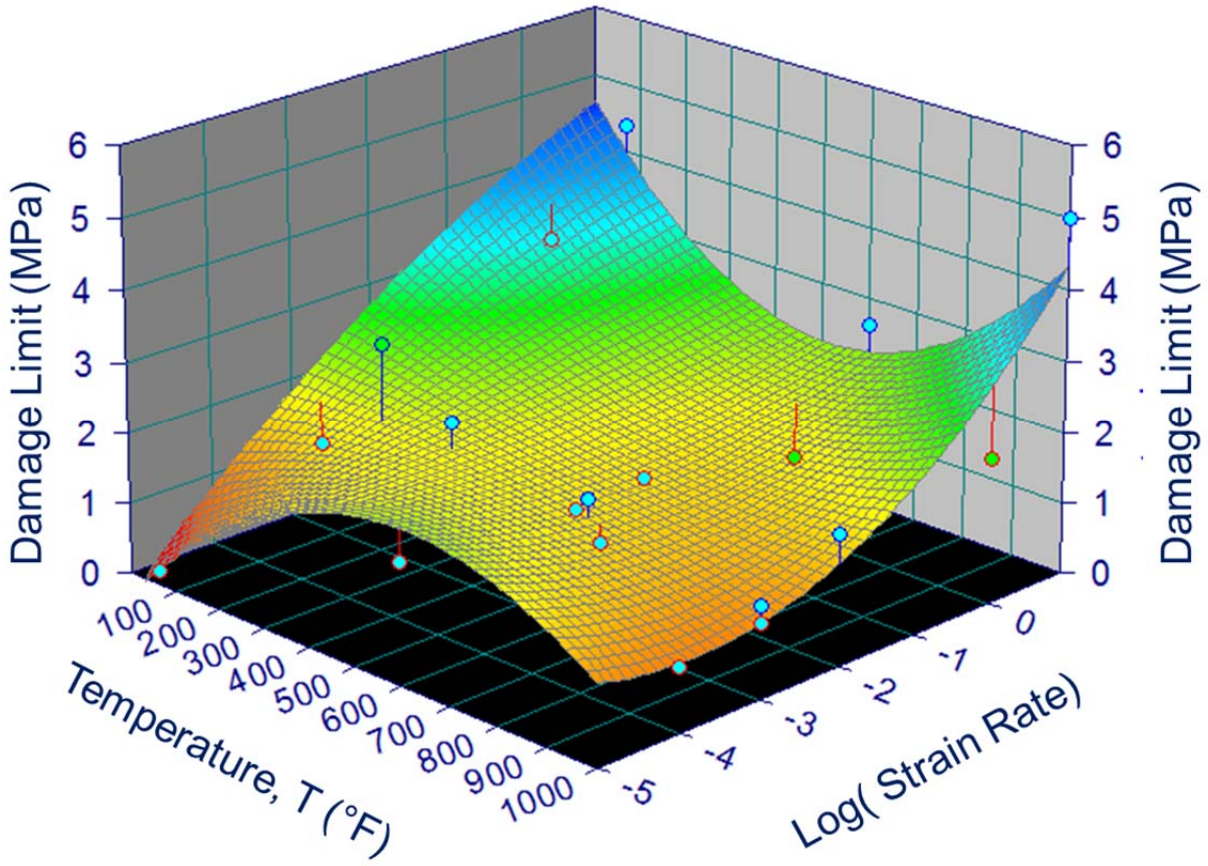

Figure 4.6: Polynomial fit to toughness versus temperature and strain rate data.

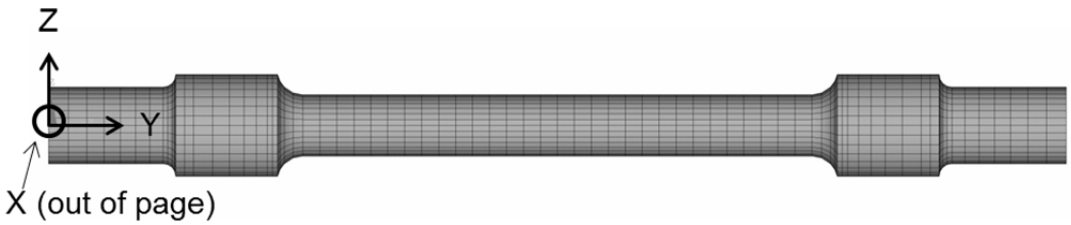

Figure 4.7: Mesh and boundary conditions for torsion simulation

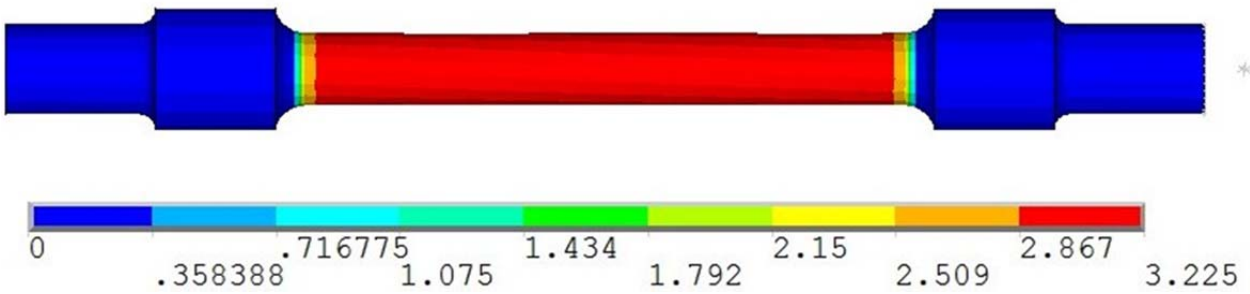

Figure 4.8: Damage contours for torsion specimen simulation. (a) Specimen surface. (b) Cross section at midplane.

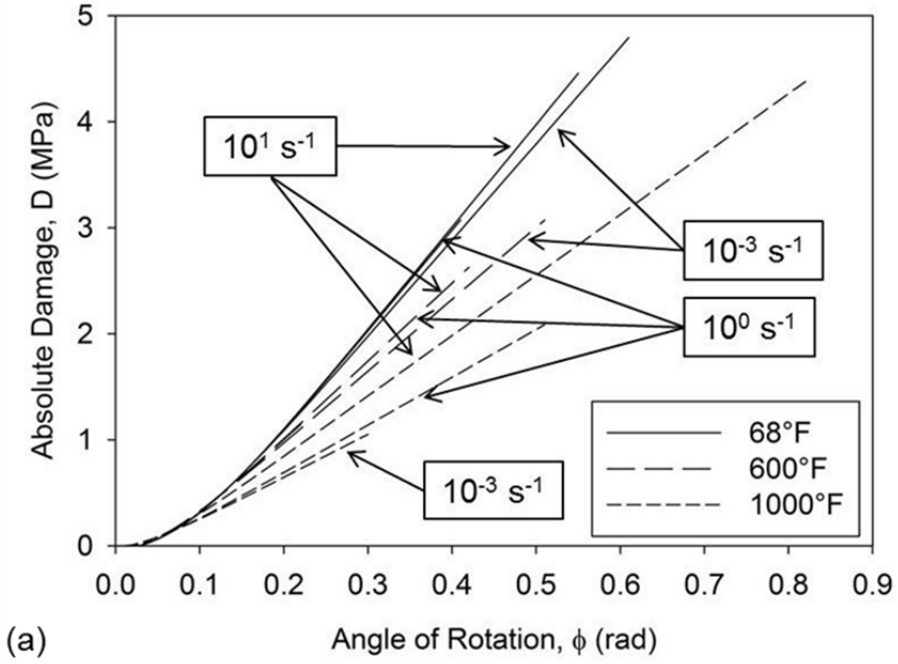

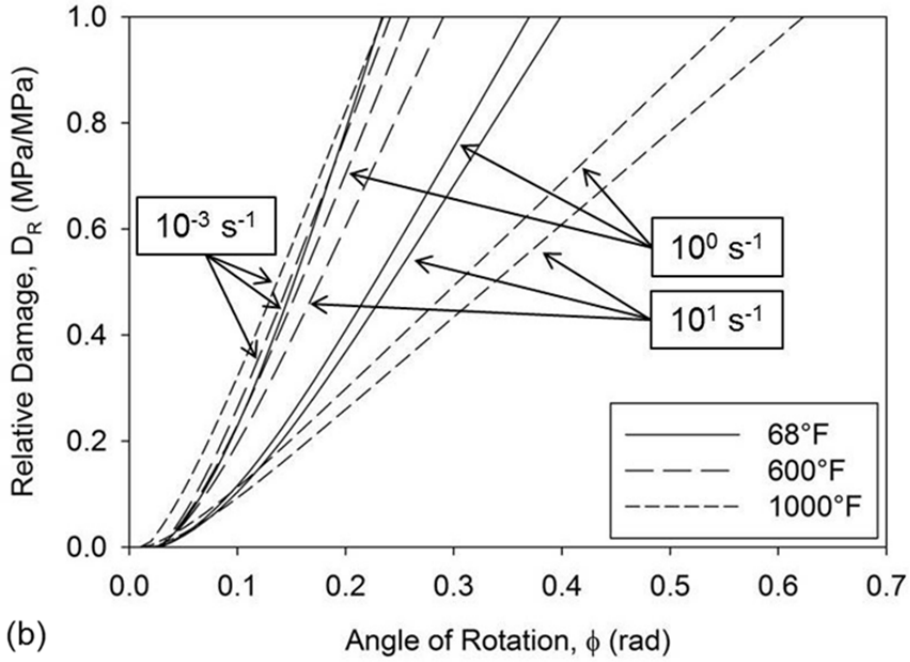

Figure 4.9: Simulated damage histories. (a) Absolute damage. (b) Relative damage.

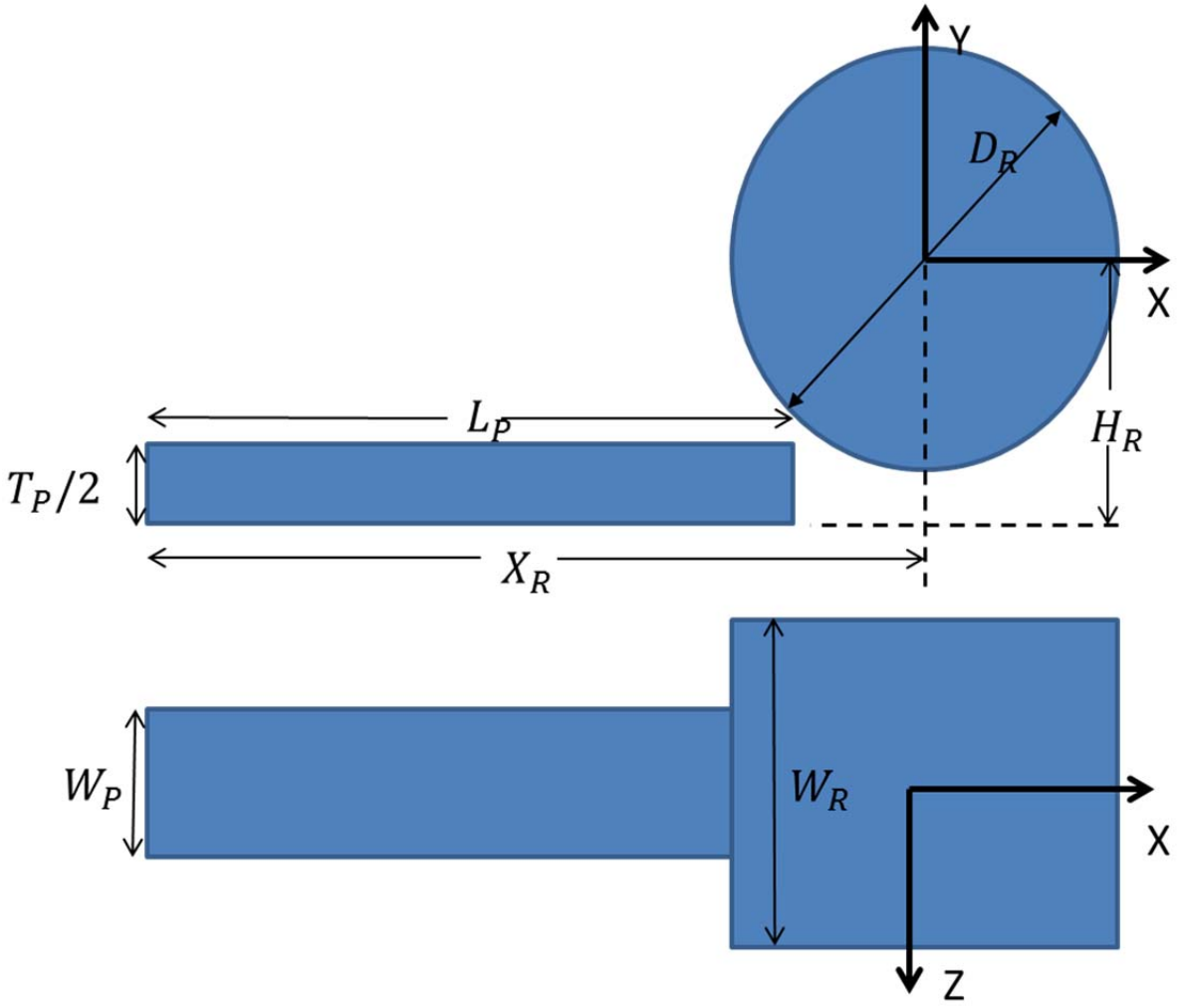

Figure 4.10: Rolling simulation geometry

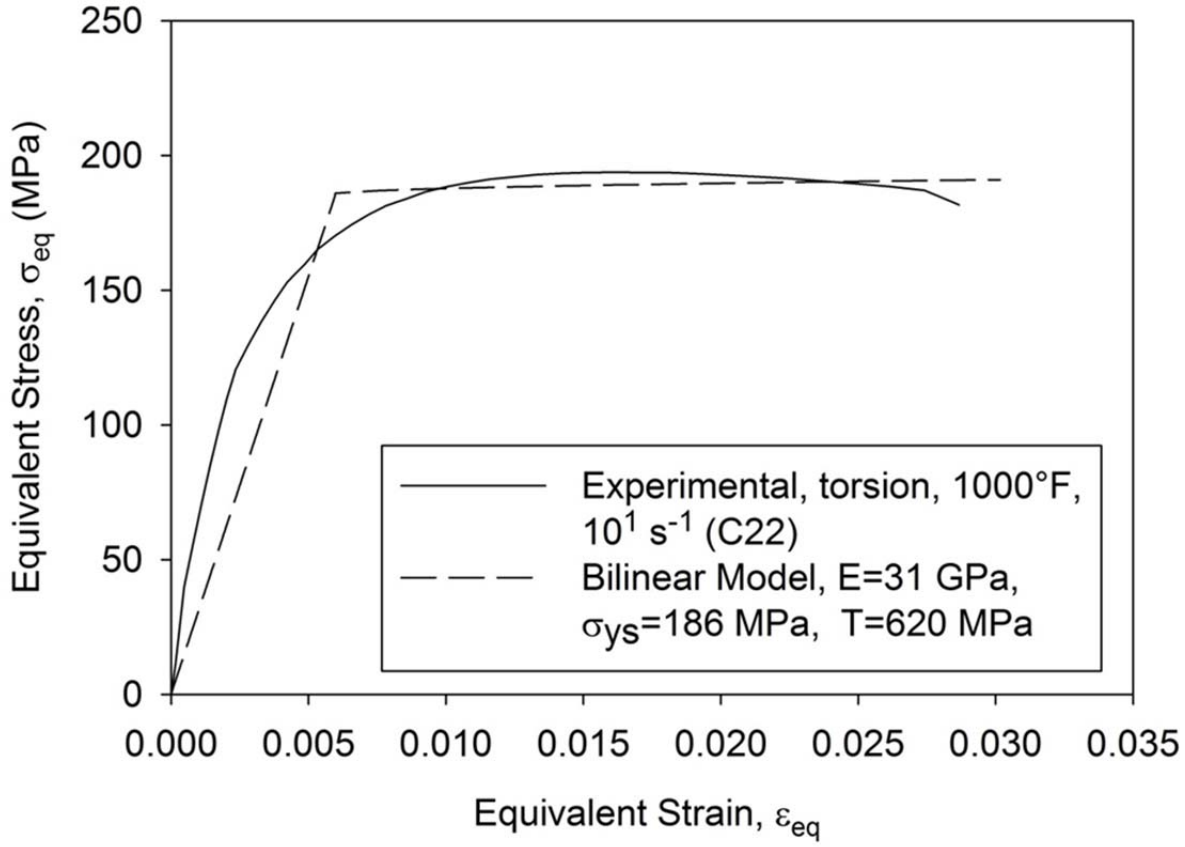

Figure 4.11: Equivalent stress v. strain for torsion test performed at 538°C (1000°F) and equivalent strain rate of 10^1 s^{-1} and bilinear approximation used for LS-DYNA simulation.

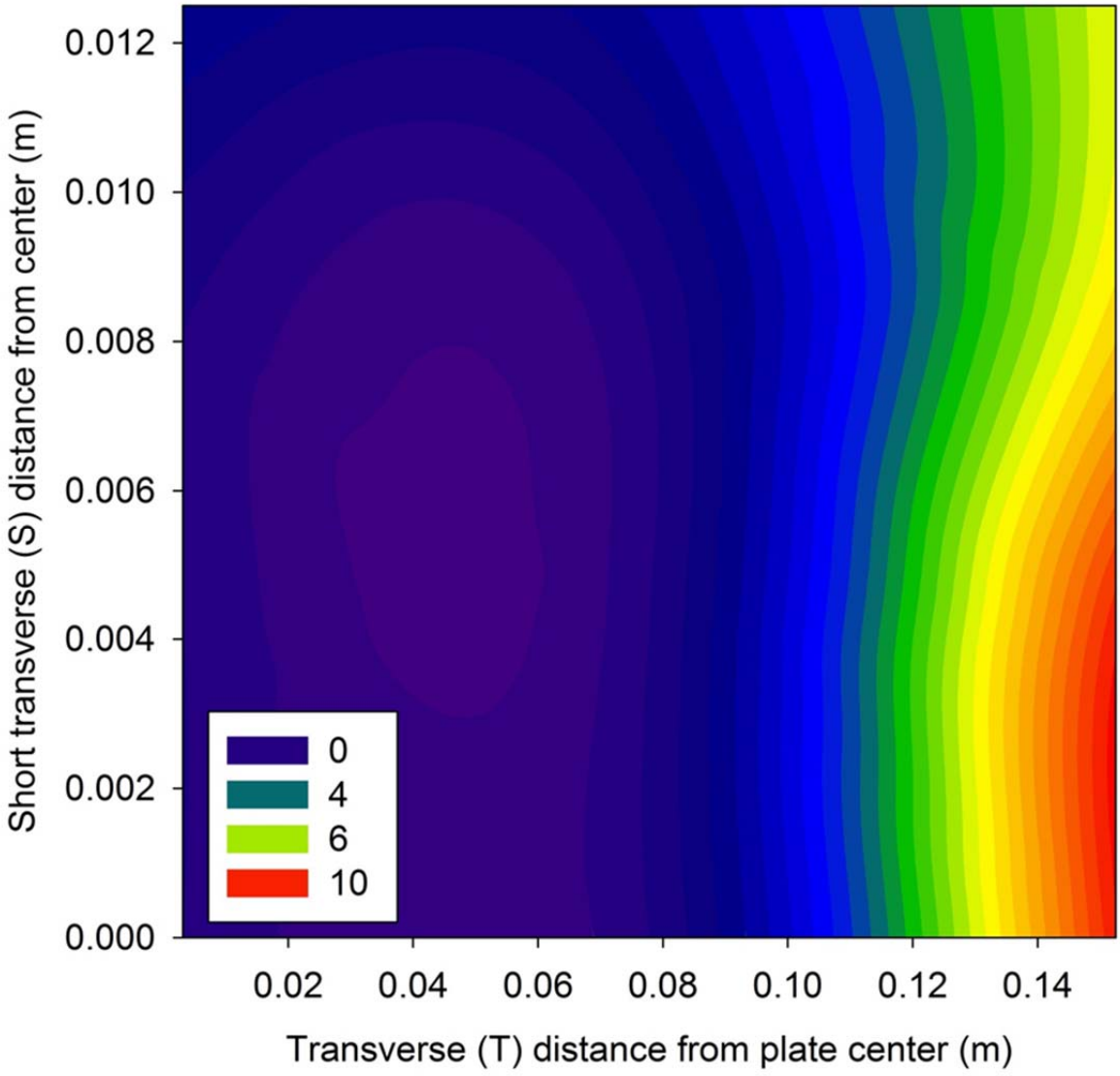

Figure 4.12: Rolling damage

CHAPTER 5: GENERAL DISCUSSION

In the preceding chapters, the mechanical characterization and numerical modeling of A359-SiC_p-30%, a light-weight aluminum metal-matrix composite, has been described. Results of tensile testing were conveyed in CHAPTER TWO, and results of torsion testing were given in CHAPTER THREE. Material properties obtained through tensile testing at various temperatures and strain rates were used to calibrate a temperature- and strain rate-dependent constitutive model for as-cast A359-SiC_p-30%. The model was implemented in the ANSYS finite element software suite through a user-programmable feature and used to simulate tension, torsion, and hot rolling. In CHAPTER FOUR, the model was extended by the introduction of a temperature- and strain rate-dependent damage model which allowed prediction of the workability of the material under various loading conditions.

In CHAPTER TWO, the dependence of various material properties on strain rate and temperature was identified by a series of experiments at different strain rates and temperatures representative of those expected to be encountered during hot rolling of as-cast A359-SiC_p-30%. The constitutive model that was constructed to simulate the material response was found to capture the strain rate and temperature dependence of the material. Simulated tensile response matched the elastic behavior, hardening evolution, and ultimate strengths of experiments throughout the range of temperatures and strain rates studied.

In CHAPTER THREE, the data obtained from a series of torsion tests performed at various rates and temperatures was analyzed. A scale model of the torsion specimens used for testing was

constructed in ANSYS and simulations of torsion tests were performed. Various means of extracting shear strain and shear stress from the simulation were compared. Shear stress-strain curves obtained from simulations were compared with experimental results, and the simulated response was found to match well with experiment in most cases.

In CHAPTER FOUR, trends in the toughness of as-cast A359-SiC_p-30% were examined. The trends were used to define a temperature- and strain rate-dependent failure criterion for an uncoupled damage model. The damage model was used to investigate the workability of A359-SiC_p-30% under torsion and during the hot rolling process. The damage model predicted material failure at the transverse edges of the rolled sheet, which coincides with observations of hot-rolled A359-SiC_p-30%.

In sum, the work presented here provides a thorough characterization of the aluminum MMC A359-SiC_p-30% and describes a constitutive model which captures the mechanical response of the material under arbitrary load configurations and at temperatures and strain rates encountered during hot or cold rolling. It also provides several examples of the utilization of the model in the simulation of mechanical testing and materials processing. In future work, the model may be used to complete a parametric study of the hot rolling process for A359-SiC_p-30%, which will allow the identification of rolling parameters that result in minimal edge cracking in rolled sheets of the material.